

**NOVEL METALLURGICAL APPROACHES TO CARBON
TRANSFORMATIONS**

by
Gina Greenidge

A dissertation submitted to Johns Hopkins University in conformity with the
requirements for the degree of Doctor of Philosophy

Baltimore, Maryland
March 2021

© 2021 Gina Greenidge
All Rights Reserved

Abstract

The interaction between metals and carbon has been of significant scientific and technological interest for hundreds of years. More recently, with the discovery that graphene (a single sheet of graphite that exhibits superlative physical properties) can be isolated experimentally, many techniques to produce this material and other valuable forms of carbon have emerged. This work reports novel metallurgical methods to synthesize various carbon architectures but also provides fundamental understanding of the mechanisms that occur when carbon transforms from one allotrope to another.

Porous graphite was prepared by dealloying SiC in molten germanium and then excavating the Ge phase. Dealloying is a technique whereby nanoporous materials are produced via the selective dissolution of one or more components from an alloy. Here, the liquid metal dealloying (LMD) process was extended to non-metal precursors, demonstrating that carbide-derived carbons (CDCs) can be fabricated by this process. The dealloying depth, concentration profile, and length scale of the dealloyed microstructure were examined as they varied with immersion times and temperatures. The dealloying depth h varied with time as $h \sim t^{1/2}$, and we also observed a buildup of Si concentration in the germanium in front of the dealloying interface. However, the measured activation barrier of 2.4 – 2.8 eV was too high to be consistent with diffusion in the liquid phase, so instead, we propose a mechanism in which Si diffusion is impeded by unsaturated carbon bonds in front of the dealloying interface. The porous graphite exhibited three-dimensional connectivity and a high degree of crystallinity, with an I(D)/I(G) ratio of 0.3 for samples dealloyed at the highest temperatures, as determined by Raman spectroscopy.

Additionally, we have developed the first study on the preparation and characterization of freestanding nanostructured carbon materials produced by melt spinning nickel-carbon alloys with carbon fractions up to 12 at. % and iron-carbon alloys with carbon fractions of 17 at. %. The carbon was excavated by chemical dissolution of the metal. We performed a detailed study on the precipitation kinetics of carbon in nickel-carbon ribbon. The equilibrium solubility of carbon in Ni is only 2 at. % at the eutectic composition, but we attained metastable solid solubility by achieving a rapid solidification rate of up to 1.6×10^6 K/s. The excess carbon atoms occupied the octahedral interstices in the metal lattice, causing up to 2% strain for an alloy spun at a linear velocity of 80 m/s; the lattice distortion was reversed via high temperature heat treatments. We also demonstrated the ability to tune the microstructure of carbon precipitated from the rapidly quenched ribbon by varying the carbon content from 4 – 12 at. % in the precursor and annealing the ribbon at temperatures that ranged from 400 – 1200 °C. By the step-wise variation of these two parameters, we sequentially transformed amorphous carbon nanospheres with a high BET surface area of 203.4 m²/g into thick, highly crystalline flakes of graphite as determined by Raman spectroscopy and transmission electron microscopy.

Advisor: Dr. Jonah Erlebacher

Readers: Dr. Jonah Erlebacher & Dr. Mingwei Chen

Acknowledgments

The completion of my PhD at Johns Hopkins University has been a tremendous personal and professional achievement, and one that was made possible by the input of a great number of people. I am very fortunate to have so many to thank, perhaps too many to be named individually in this brief section, so I would like to express my general gratitude to all the teachers, scientists, administrative staff, fellow students, family and friends who have accompanied me on this journey.

More specifically, I thank my advisor, Jonah Erlebacher, for granting me an unscheduled meeting during the prospective student visit day in 2015, after which he made me an offer to join his research group. When I was deciding which graduate school to choose, I sat down with my then Masters research advisor, Joshua Halpern, who had looked into all of my potential advisors and graduate programs. He told me I should pick Jonah, and I agreed. Since then, Jonah has been a mentor who was always available for thoughtful and detailed discussions about research problems while also allowing his students enough room for independent problem-solving. He encouraged his students to “play” in the lab, giving us room for scientific creativity. I am grateful to have been trained by him.

I also thank my dissertation committee members Dr. Mitra Taheri, Dr. Howard Fairbrother, Dr. Chao Wang, and Dr. Mingwei Chen. I appreciate the time they spent reading my dissertation, attending my talk, evaluating and providing feedback about my work. I also thank Dr. Evan Ma, who was a member of my thesis proposal committee, along with Dr. Patricia McGuiggan, who, in addition to being a committee member, was always available for a word of advice and encouragement.

I also thank the Department of Materials Science and Engineering staff who have significantly contributed to my time at Hopkins. Jeanine Majewski, Ellen Libao, Ada Simari, Meg Tully, Bryan Crawford and Phil Chapman, Dr. Ken Livi and Sam Norris, thank you for running the department so smoothly. You have consistently gone above and beyond for students and I appreciate your assistance.

My current and former labmates: Alyssa Chuang, Dr. Shashank Vummidi Lakshman, Jodie Baris, Sam Price, Aliya Carter, Dr. Tyler Pounds, Dr. Ian McCue and Luthfe Siddique, thank you for always being willing and available to discuss esoteric dealloying-related and other science topics and to lend a pair of hands when I needed help. It has been a great pleasure to work with and build friendships with all of you.

I would also be remiss if I did not thank professors and scientists associated with the Howard Nanofabrication Fabrication facility at Howard University. I joined that lab as an undergraduate and the training I received there has been integral to my development as a researcher. When I decided that I wanted to return to Howard for graduate school, I called Dr. Joshua Halpern and Dr. Gary Harris, and they made it happen. James Griffin, Tony Gomez, Crawford Taylor, Dr. Tina Brower-Thomas, thank you for your guidance, continued support and friendship. Dr. Michelle Chavis, Alexis Shepherd, Amber Wingfield, my former labmates and current friends, thank you for making the lab such a joyful place to work every day.

We entered the era of the Covid-19 pandemic during the final year of my PhD program and while the uncertainty, the immobility and the lockdowns were difficult, I was fortunate to have amazing people in my bubble: Paige Jones, Erin Gallagher, Connie Sanabria and Suhas Eswarappa Prameela. Thank you for the laughter, the daily walks, the

multiple trips for ice cream, the picnics, the Love Island marathons, and for your company.

Finally, I thank my family. My parents, Betty Ann and Harold, thank you for your love, support, and encouragement. I acknowledge the many sacrifices you have made so your children could have more opportunities than you had. Thank you for always reminding me that I always have a home to return to no matter what happens. My big sister, Genai, thank you for always taking care of me. Chenele, my cousin, thank you for your support and for always being up for a last-minute trip. My brother and brother-in-law, Jevon and Osaze, respectively, thank you for all your encouragement and for always providing much needed laughter. Riley, Noah, and Emre, my nieces and nephew, thank you for your hugs, smiles and contagious joy.

Table of Contents

| | |
|---|-----|
| Abstract | ii |
| Acknowledgments..... | iv |
| Table of Contents | vii |
| List of Tables | xi |
| List of Figures | xii |
| 1 Introduction | 1 |
| 1.1 Motivation | 1 |
| 1.2 Chapter Summaries | 3 |
| 1.3 Carbide Derived Carbons | 5 |
| 1.3.1 CDC Synthesis Methods | 6 |
| 1.3.2 Kinetics of CDC Transformations | 8 |
| 1.4 Dealloying | 9 |
| 1.4.1 Electrochemical Dealloying..... | 11 |
| 1.4.2 Coarsening | 16 |
| 1.4.3 Conditions for Electrochemical Dealloying..... | 17 |
| 1.4.4 Liquid Metal Dealloying..... | 18 |
| 1.4.5 Comparison between Liquid Metal Dealloying and Electrochemical Dealloying..... | 22 |
| 1.5 Melt Spinning..... | 27 |
| 1.5.1 Working Principle..... | 28 |
| 1.5.2 Microstructural Evolution..... | 29 |

| | | |
|-------|--|----|
| 1.5.3 | Experimental Parameters That Affect the Cooling Rate..... | 30 |
| 1.6 | Raman Spectroscopy | 32 |
| 1.7 | References | 34 |
| 2 | Porous Graphite Fabricated by Liquid Metal Dealloying of SiC | 43 |
| 2.1 | Summary | 43 |
| 2.2 | Introduction | 44 |
| 2.3 | Experimental Methods | 48 |
| 2.3.1 | Liquid Metal Dealloying..... | 48 |
| 2.3.2 | Characterization of As-Dealloyed SiC/Ge Samples | 50 |
| 2.3.3 | Excavation of the Pure Graphite Phase..... | 51 |
| 2.4 | Results and Discussion..... | 52 |
| 2.4.1 | General Observations..... | 52 |
| 2.4.2 | Dealloying kinetics and morphological evolution in SiC-Ge. | 54 |
| 2.4.3 | Ligament morphology and size..... | 63 |
| 2.4.4 | Raman spectroscopy of porous graphite..... | 69 |
| 2.5 | Conclusion..... | 73 |
| 2.6 | References | 75 |
| 3 | Carbon Transformations in Rapidly Solidified Nickel-Carbon Ribbon..... | 81 |
| 3.1 | Summary | 81 |
| 3.2 | Introduction | 81 |
| 3.3 | Experimental Methods | 85 |
| 3.3.1 | Alloy Preparation..... | 85 |

| | | |
|-------|--|-----|
| 3.3.2 | Melt Spinning..... | 85 |
| 3.3.3 | Thermal annealing of melt spun ribbon..... | 88 |
| 3.3.4 | Characterization tools..... | 88 |
| 3.4 | Results and Discussion..... | 88 |
| 3.4.1 | Microstructural evolution of melt-spun ribbon..... | 88 |
| 3.4.2 | The effect of annealing temperature and time on carbon precipitation..... | 97 |
| 3.5 | Conclusions..... | 102 |
| 3.6 | References..... | 103 |
| 4 | Microstructural Evolution of Freestanding Carbon from Rapidly Solidified Nickel- Carbon Ribbon..... | 109 |
| 4.1 | Summary..... | 109 |
| 4.2 | Introduction..... | 109 |
| 4.3 | Experimental Methods..... | 110 |
| 4.3.1 | Dissolution of metal phase to excavate carbon material..... | 110 |
| 4.3.2 | Characterization tools..... | 110 |
| 4.4 | Results and Discussion..... | 111 |
| 4.4.1 | The microstructural evolution of freestanding carbon..... | 111 |
| 4.4.2 | Microstructure of precursor carbon material..... | 113 |
| 4.4.3 | Microstructure of carbon excavated from as-spun ribbon..... | 114 |
| 4.4.4 | Microstructure of carbon from excavated from annealed ribbon..... | 118 |

| | | |
|--|--|-----|
| 4.5 | Conclusions | 123 |
| 4.6 | References | 124 |
| 5 | Amorphous Carbon Foam Fabricated by Melt Spinning Iron-Carbon Alloys | 126 |
| 5.1 | Summary | 126 |
| 5.2 | Introduction | 126 |
| 5.3 | Experimental Methods | 128 |
| 5.3.1 | Alloy Preparation | 128 |
| 5.3.2 | Melt Spinning..... | 128 |
| 5.3.3 | Dissolution of metal phase to excavate carbon material..... | 130 |
| 5.3.4 | Ribbon Annealing | 130 |
| 5.4 | Results and Discussion..... | 131 |
| 5.4.1 | Microstructural variation in Fe-C alloy | 131 |
| 5.4.2 | Microstructural evolution of the carbon after Fe removal | 134 |
| 5.5 | Conclusion..... | 138 |
| 5.6 | References | 140 |
| 6 | Summary and Prospects | 142 |
| 6.1 | References | 148 |
| Appendix A: Porous Tungsten Fabricated by the Liquid Metal Dealloying of Tungsten Silicides.....149 | | |
| Appendix B: BET Surface Area Reports for Carbon from Melt Spun Ribbon | | |
| Curriculum Vitae | | 172 |

List of Tables

| | | |
|------------|---|-----|
| Table 2-1. | Summary of properties of porous graphite processed under different conditions. | 73 |
| Table 4-1. | Summary of Raman spectrum properties of freestanding carbon etched from melt spun Ni ₉₂ C ₈ ribbon annealed at different temperatures. | 122 |

List of Figures

- Figure 1-1. A graphic depicting the microstructure of multiple allotropes of carbon. *Graphite typically comprises 10 or more layers of graphene; only two layers are shown here for illustration. Adapted from Ref. [1]. 2
- Figure 1-2. CDC film prepared by the chlorination of TiC. Reprinted from Ref. [11] ... 5
- Figure 1-3. Sintered α -SiC in Ar + 3.5% Cl₂ (left). A plot of CDC layer thickness vs. reaction time at two temperatures (right). For a short time and low temperatures, linear kinetics dominate. At higher temperatures and longer reaction times, a parabolic time law is observed. Adapted from Ref. [6]. 9
- Figure 1-4. A schematic depicting the four dealloying techniques differentiated by the use of different dealloying media used to facilitate the selective removal of a component from an alloy. Typical setups for each experiment are also shown (Reused from Ref. [31]) 11
- Figure 1-5. Working model for porosity in the Ag-Au alloy system (Ag, *grey*; Au, *orange*). (a) Ag atoms dissolve from terrace sites – the rate-limiting step. (b) Surface diffusion passivates low-coordination sites with Au, leading to surface roughening. (c-d) As dealloying proceeds, a large surface area develops, leading to exposure of undissolved Ag atoms. As a result, ligaments are undercut and bifurcated. (e) Nanoscale ligaments with Au-rich surface and Ag-rich interiors evolve. (f) As coarsening increases the length scale of the initial structure, residual Ag atoms are exposed and dissolved, leaving the final structure with a low Ag content. 14
- Figure 1-6. Scanning electron micrograph of nanoporous gold prepared by immersing Au₂₆Ag₇₄ in nitric acid. Adapted from Ref. [36]..... 15
- Figure 1-7. SEM and optical micrographs (insets) of nanoporous Au formed by free corrosion of a homogenous Ag₆₅Au₃₅ alloy in concentrated nitric acid. (a) The system was dealloyed for 24 h and exhibits ~ 30 nm features. (b) An

additional 100 h treatment in acid results in feature sizes that coarsen to ~60 nm. (c) Features coarsen to several micrometers after thermal treatment at 800 °C for 10 min in air (Reused from Reference [37])..... 16

Figure 1-8. Phase diagrams used to determine that nanoporous Ta can be fabricated by liquid metal dealloying of a Ta-Ti alloy in molten Cu. (a) The Ti-Ta system forms a homogeneous solid solution over the entire composition range. The composition at $Ti_{55}Ta_{45}$ is highlighted as an example of a typical precursor alloy. (b) The Ta-Cu system shows limited solubility of Ta in Cu at temperatures investigated in LMD (highlighted by the green bar). (c) The Ti-Cu system shows that when small amounts of Ti (relative to Cu) are immersed in liquid Cu, dissolution occurs..... 19

Figure 1-9. (a) A photograph showing a Ti-Ta sample being immersed in a liquid Cu bath heated by RF induction. (b-c) A schematic depicting porosity formation on the surface of the sample during LMD. (d) SEM micrograph of a sample of $Ti_{55}Ta_{45}$ dealloyed in Cu at 1240 °C for 20 s. The dealloying interface is sharp and flat, clearly delineating the undealloyed parent material on the left and the porous Ta-Cu composite on the right (Adapted from Ref. [45])..... 20

Figure 1-10. Periodic table (© 2015 Todd Helmenstine) highlighting elements that have been dealloyed electrochemically (purple) and elements that have been dealloyed via liquid metal dealloying (orange). Adapted from Ref. [47]. .. 21

Figure 1-11. SEM images of porous C produced by the dealloying a Mn-C ingot in liquid Bi at 800 °C for 600 s, following by removal of the Bi rich phase in HNO_3 . (a) Porous C developed from the dealloying of the α -Mn phase (b) Porous C developed from the dealloying of the $Mn_{23}C_6$ phase. Adapted from Ref. [48]. 22

Figure 1-12. Universal trend in ligament diameter versus the inverse homologous temperature ($T_m/T_{dealloy}$) for ECD (red-to-yellow gradient) and LMD (blue-to-green gradient) at various dealloying times (different marker shapes.) The

dealloying duration significantly impacts ligament diameter for low melting point elements and high dealloying temperatures, causing scatter at high homologous temperatures. Reprinted with permission from Ref. [47]..... 24

Figure 1-13. Comparison of dealloyed morphologies formed in liquid metal and aqueous electrolyte as a function of parent alloy composition. (a) Ti_xTa_{1-x} dealloyed in molten Cu via liquid metal dealloying; at low Ta concentrations, the dealloyed morphology forms droplets and lamella and as the Ta content increases, the dealloyed morphology becomes interconnected. (b) Ag_xAu_{1-x} dealloyed in concentrated HNO_3 via electrochemical dealloying; the dealloyed structure is bicontinuous for all Au concentrations. Reused with permission from Ref. [47]. 26

Figure 1-14. A schematic diagram of the melt spinning process. The liquid melt is impinged on a rotating wheel where it forms a melt spool from which solidified ribbon is expelled. 29

Figure 1-15. Schematic representation of the microstructure typically found in melt spun ribbons. Adapted from Ref. [55]. 30

Figure 1-16. Motions of the atoms in graphitic materials that give rise to the D peak (left) and the G peak (right). Adapted from Ref. [72]. 33

Figure 2-1. (a) Binary phase diagram of Si-C. (b) Binary phase diagram of Ge-Si showing miscibility over the entire composition range in solid and liquid phases. (c) Binary phase diagram of C-Ge effectively showing no solubility of C in Ge at temperatures below 1400 °C. © ASM International. 47

Figure 2-2. (a) Schematic diagram depicting dealloying process of single crystal SiC in molten Ge. Ge dissolves Si from the parent alloy, leaving behind a porous graphite network. (b) Optical micrograph showing SiC with a dealloyed region. Ge, the dissolving medium, solidifies in the carbon pores upon termination of the dealloying process. A fully dense network of carbon with Ge solidified in its pores is shown. Dealloying generally starts preferentially

on the Si-terminated face surface while the C-terminated surface remains unchanged..... 49

Figure 2-3. Scanning electron microscopy (SEM) micrographs of SiC samples dealloyed in molten germanium at 1300 °C for different times. The dealloying front proceeds right to left from the geometric surface towards the sharp and flat dealloying interface. The dealloying region displays different contrast as the light phase is Ge rich and the dark phase is carbon. The two images on the left were taken at 850x magnification and the images on the right were taken at 800x magnification, but it can be observed that the dealloying depth increases with time. 51

Figure 2-4. Optical micrographs of various types of SiC dealloyed under identical experimental conditions: (left) 4H research grade, (middle) 6H research grade and (right) 4H dummy grade. 54

Figure 2-5. (a) Plot of dealloying depth h vs. time t measured at 1200 °C (blue, squares), 1300 °C (yellow, diamonds) and 1400 °C (green, triangles). (b) Plot of dealloying depth vs. $t^{1/2}$. Dealloying depth increased with increasing temperature and appeared to follow a power-law relationship with time. The error bars represent one standard deviation..... 56

Figure 2-6. Collapsed dealloying depth versus scaled time $t' = t \cdot \exp - E_a/kBT$ for SiC for measurements taken at 1200 °C (blue, squares), 1300 °C (yellow, diamonds), and 1400 °C (green, triangles). Dashed line: fits to the data using the relationship $ht \sim t^{1/2}$. The values for E_a and the scaling exponent were determined as the values associated with best least-squares fit. 58

Figure 2-7. Si mole fraction versus distance away from the dealloying interface for SiC dealloyed in molten Ge at 1300 °C for 5 minutes (orange, squares) and 9 minutes (blue, circles). The dealloying interface is $x = 0$ and distance from the dealloying interface represents the liquid side of the interface. Unlike in conventional LMD, where there is a gradual decline of the dissolving

component across the dealloyed region, the Si concentration declines rapidly to near 0 at. % within the first micrometer of the dealloyed region for both dealloying time periods shown. Solid line: data fits steady state diffusion equation as $Cx = Ca_{exp} - viDL x'$ 60

Figure 2-8. (a) SEM micrographs depicting ligament size increase with increasing temperature. Variation in ligament morphology is also observed with a higher degree of interconnectedness at the lowest experimental temperature, coalesced graphite particles aligned perpendicular to the dealloying direction at 1300 °C, and larger circular particles at the highest temperature. (b) Ligament diameter versus processing temperature for dealloying SiC. Length scales increase at higher temperatures. (c) Trend in ligament diameter versus inverse homologous temperature ($T_m/T_{dealloy}$) for electrochemical dealloying and liquid metal dealloying at different times, shown as grey triangles for metal systems (adapted with permission from reference [25]. Error bars represent one standard deviation. For comparison, the trend between ligament diameter and inverse homologous temperature for SiC ($T_{sublimation}/T_{dealloy}$) is shown as green squares. Error bars lie within the data markers..... 65

Figure 2-9. (a) SEM micrograph of porous graphite produced by dealloying at 1400 °C. (b) SEM micrograph of a cross-section of SiC dealloyed at 1300 °C. The morphology of the porous graphite is shown at increasing magnifications. The material presents as clusters of graphite flakes on the surface..... 66

Figure 2-10. TEM images of a SiC sample dealloyed in molten Ge at 1400°C after etching in aqua regia to remove solidified Ge from pores. Images depict highly interconnected porous graphite. (Inset) selected area electron diffraction shows that the graphite is polycrystalline. 67

Figure 2-11. SEM micrograph showing anomalous carbon structures with larger feature sizes near the geometric surface of the sample during LMD at 1300°C. There is a 25 µm region on the surface where the carbon ligaments appear > 5µm in

| | | |
|--------------|--|----|
| | diameter, but the rest of the sample shows uniform particle size up to the dealloyed interface. | 69 |
| Figure 2-12. | Raman spectra of the porous graphite before and after the Ge phase was etched from the pores. The Raman fingerprint exhibits characteristics features of nanographite. The very low intensity peaks between 1700 cm^{-1} and 2600 cm^{-1} were activated by the epoxy sample mount. | 71 |
| Figure 2-13. | Raman spectra of porous graphite processed at different dealloying temperatures. | 73 |
| Figure 3-1. | (a) Photograph showing major components of the melt spinning apparatus. (i) A typical boron nitride crucible that houses the pre-cast nickel carbon ingot is shown. (ii) RF coils surround the base of the crucible and are used to melt the ingot. The melt is ejected onto the surface of (iii) the water-cooled copper wheel and solidified into ribbon that is retrieved from (iv) the collection tube. | 86 |
| Figure 3-2. | (a) Micrographs depicting the difference in microstructure of Ni_{92}C_8 cast in an induction furnace and that of melt-spun ribbon of the same composition. A dendritic solidification microstructure with visible carbon precipitation in the nickel is seen in the ingot while a homogeneous single phase is observed for the melt-spun ribbon. (b) Cross-section of $\text{Ni}_{88}\text{C}_{12}$ ribbon showing a typical melt-spun microstructure. Carbon precipitates highlight the evolution of the grain structure from the ribbon surface that was in contact with the wheel to the ribbon free surface. | 90 |
| Figure 3-3. | Ribbon thickness (h) vs. tangential wheel velocity (v) for different carbon fractions: Ni containing 4 at. % C (purple, diamonds), 8 at. % C (blue, squares), 10 at. % C (green, triangles). | 93 |
| Figure 3-4. | TEM micrographs of Ni_{92}C_8 ribbon. (a) Image taken before annealing show micron-sized grains and no evidence of carbon precipitation. (b) Image of | |

ribbon annealed at 1000 °C for 1 hour show grain growth and the presence of large graphite particles (light particles) embedded in the Ni matrix (inset).94

Figure 3-5. (a) XRD patterns showing the effect of annealing on the Ni peak positions in melt-spun ribbon prepared under the same conditions. (i) Shows unstrained Ni (111) peak. (ii) Shows a Ni (111) peak shift to a smaller 2θ indicating lattice expansion. The peak shoulder is the $K\alpha_2$ peak. (iii) Shows that annealing relieves the lattice strain. (b) Plot of lattice spacings in melt spun Ni-C ribbon with different carbon fractions as a function of tangential wheel velocity: Ni containing 4 at. % C (purple diamonds), 8 at. % C (blue squares), 10 at. % C (green triangles). Little to no change in d_{hkl} is observed for ribbon containing 4 at.% C indicating minimal strain, but for material with higher carbon fractions, d_{hkl} increases monotonically with wheel velocity, indicating increasing amounts of saturation of the Ni lattice with carbon. 96

Figure 3-6. (a) SEM micrographs showing growth of carbon precipitates in $Ni_{92}C_8$ ribbon annealed at 1000 °C for increasing times. (b) Log-Log plot of mean particle size as a function of time. The dashed line shows a power law fit with $n = 1/3$ 99

Figure 3-7. (a) Microstructural variation of melt-spun Ni-C ribbon (cross-section) with varying carbon content and annealed at different temperatures. Scale bars are 5 μm . (b) Plot of average carbon particle size in ribbon vs. annealing temperature for Ni-C ribbon of varying carbon fractions: Ni containing 8 at. % C (dark blue squares), 10 at. % C (green triangles) and 12 at.% C (light blue diamonds). The activation energy of 1.43 eV is consistent with bulk diffusion of carbon in Ni. 101

Figure 4-1. Microstructural variation of carbon excavated from melt-spun ribbon annealed at different temperatures with varying precursor carbon contents. Scale bars are 4 μm 112

| | | |
|-------------|---|-----|
| Figure 4-2. | (Top) (a) and (b) Commercially prepared graphite used to prepare precursor Ni-C ingots for melt-spinning; (Bottom) (c) and (d) Carbon flakes and spheroids collected by chemical dissolution of Ni from Ni-C ingots prepared by induction melting..... | 113 |
| Figure 4-3. | Carbon etched from Ni ₉₂ C ₈ melt-spun ribbon before annealing showing two types of morphologies (a) Thin carbon flake comprised of clusters of nanometer sized carbon particles. (b) The structure shown in (a) is magnified. (c) A large carbon “slab” that is 10 μm thick and over 100 μm long. (d) At higher magnification, the slab is observed to be comprised of clusters of interconnected submicron sized particles..... | 115 |
| Figure 4-4. | TEM micrographs of carbon from Ni ₉₂ C ₈ ribbon before annealing showing amorphous sub-micron polygonal carbon spheres (top). After annealing at 1000 °C for one hour, the carbon particles became sized on the order of microns and exhibited a high degree of graphitic crystallinity (bottom).. | 117 |
| Figure 4-5. | (a) Carbon from Ni ₈₈ C ₁₂ melt spun ribbon before annealing showing growth front of graphene layers; (b) Carbon from Ni ₉₂ C ₈ ribbon annealed at 1200 °C exhibiting the structure of Kish graphite..... | 118 |
| Figure 4-6. | Plan view of (top) as-spun Ni ₈₈ C ₁₂ ribbon and (bottom) Ni ₈₈ C ₁₂ ribbon annealed at 1000 °C for 1 hour, showing the growth of carbon (black regions) on the surface post heat-treatment. The carbon appears to grow in two forms on the ribbon surface: (left) as striations through the Ni ribbon and (right) as a layer interspersed with Ni particles embedded in the surface. | 120 |
| Figure 4-7. | Raman spectra showing increasing graphitization of carbon with increasing annealing temperatures..... | 121 |
| Figure 5-1. | Photograph of melt-spun iron-carbon ribbon | 129 |
| Figure 5-2. | The iron-iron carbide phase diagram. Adapted with permission from Reference [10]. | 132 |

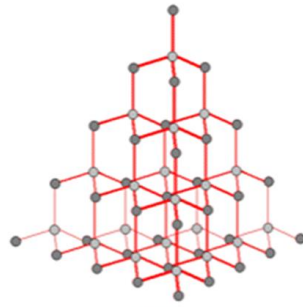
| | | |
|-------------|--|-----|
| Figure 5-3. | SEM images (a) Cross-section of $\text{Fe}_{83}\text{C}_{17}$ (at. %) alloy showing lamellar microstructure. (b) Cross-section of as-spun melt-spun ribbon showing finer features and a small region of carbon precipitates. (c) Cross-section of melt-spun ribbon annealed at 1000 °C for 1 hour showing growth of domains. | 133 |
| Figure 5-4. | XRD Patterns of melt spun $\text{Fe}_{83}\text{C}_{17}$ ribbon before and after heat treatment. Peaks corresponding to bcc-iron are labeled. | 134 |
| Figure 5-5. | Carbon foam exhibiting hierarchical porosity formed by chemical dissolution of Fe from as-spun Fe-C ribbon | 135 |
| Figure 5-6. | SEM micrographs of carbon foam fabricated from annealed melt spun Fe-C ribbon shown at different magnifications. | 136 |
| Figure 5-7. | TEM micrographs of carbon from annealed Fe-C ribbon at different magnifications. (Inset) Selected area electron diffraction showing that the carbon is amorphous. | 137 |
| Figure 5-8. | Raman spectrum of carbon from melt spun and annealed iron-carbon ribbon. | 138 |
| Figure 6-1. | (a) Scanning electron micrograph showing $\text{Mn}_{80}\text{Si}_{10}\text{C}_{10}$ that was dealloyed in liquid Bi at 800 °C. SiC powder was used to make the parent alloy. The light grey areas are Bi rich and dark grey areas are ligaments that comprise large amounts of residual Mn (~20 at. %) along with Si and C. (b) The dealloyed material post etching in acid shows faceted ligaments that comprised of 94 at. % C with some residual Si. | 144 |
| Figure 6-2. | (a) $\text{Ni}_{40}\text{Mn}_{40}\text{C}_{20}$ melt spun ribbon. (b) Powder diffraction patterns of $\text{Ni}_{40}\text{Mn}_{40}\text{C}_{20}$ melt spun ribbon before and after annealing showing the heat treatment transforms the ribbon microstructure from amorphous to crystalline. | 146 |

1 Introduction

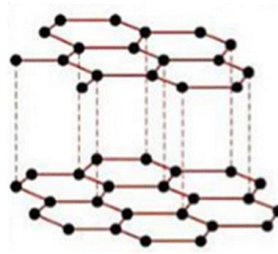
1.1 Motivation

Carbon is a versatile material. Its most common allotropes are diamond and graphite; in the former, the carbon atoms are arranged in the tetrahedra characteristic of sp^3 bonding, while the latter they are arranged in sp^2 hybridized sheets where the layers are connected by weak van der Waals forces. However, many other carbon morphologies exist: graphene, amorphous carbon, nanotubes, lonsdaleite, foams and carbide-derived carbons are examples, some of which are shown in Figure 1-1. Such a variety in morphologies leads to equal diversity in properties and corresponding applications. As such, the ability to tune the properties of carbon by transforming it from one microstructure to another is a useful technological advantage that has implications for a variety of fields.

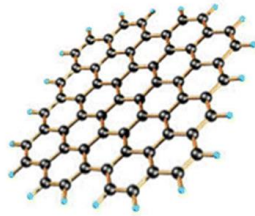
The purpose of this thesis is to establish novel methods of carbon conversion via metallurgical routes. We show that the process of preparing nanostructured porous materials via liquid metal dealloying is not restricted to metal precursors but can be extended to covalently bonded ceramic materials. We also examine the kinetics of the dealloying of a non-metal precursor and outline how it differs from conventional dealloying. We demonstrate that a variety of carbon nanostructures, including amorphous carbon, graphene and graphite sponges can be fabricated from inexpensive graphite materials via a rapid solidification process called melt spinning.



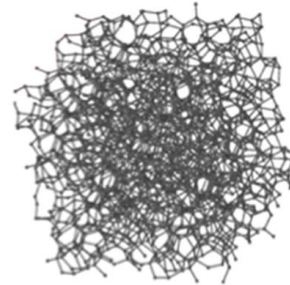
Diamond



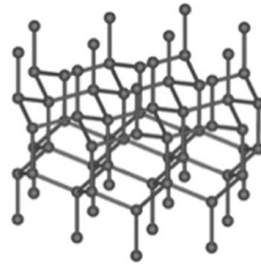
Graphite



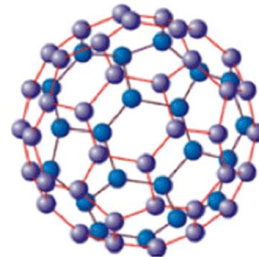
Graphene



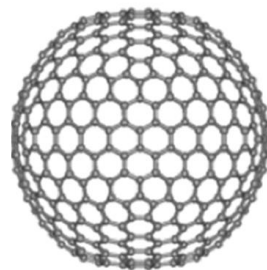
Amorphous carbon



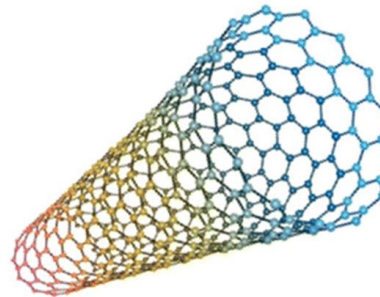
Lonsdaleite



C60-fullerene



C540-fullerite



Carbon nanotube

Figure 1-1. A graphic depicting the microstructure of multiple allotropes of carbon. Graphite typically comprises 10 or more layers of graphene; only two layers are shown here for illustration. Adapted from Ref. [1].

1.2 Chapter Summaries

The remainder of the chapter will give an overview of the fundamental concepts required to understand the techniques used to synthesize carbon materials in this work. It will also provide a review of the relevant literature, highlighting important experimental breakthroughs that have advanced the field.

In Chapter 2, we show that liquid metal dealloying is a promising technique in the fabrication of porous carbon material from silicon carbide. We simultaneously establish the ability to expand the set of materials available to dealloying as well as provide an alternative route to the preparation of a carbide-derived carbon with a uniform morphology and tunable pore size. We also examine the kinetics of the liquid metal dealloying of a non-metal precursor as it deviates from the expected mechanisms typically seen in dealloying of metal alloys.

In Chapter 3, we present a study of the microstructural variations that occur in Ni-C alloys that are processed via melt spinning. We attained metastable solid solubility of carbon in nickel ribbon by achieving a rapid solidification rate of up to 1.6×10^6 K/s. Excess carbon atoms were found to occupy the octahedral interstices in the nickel lattice causing up to 2% strain for an alloy spun at 80 m/s tangential wheel speeds. We also examine the precipitation kinetics when the ribbon is subjected to high temperature heat treatments. We find that annealing leads to precipitation of carbon from the nickel lattice on the ribbon free surfaces but also leads to subsequent growth of spherical precipitates within the nickel matrix via bulk diffusion-driven Ostwald ripening.

In Chapter 4, we examine the microstructural evolution of carbon that was produced via chemical dissolution of the Ni from supersaturated melt spun Ni-C. We will

show that the morphology can be tuned by varying the carbon content from 4 – 12 at. % in the precursor and annealing the ribbon at temperatures that ranged from 400 – 1200 °C. Via the step-wise variation of these two parameters, we sequentially transformed amorphous carbon nanospheres with a high BET surface area of 203.4 m²/g (see Appendix B.1) into graphene and eventually into thick, highly crystalline flakes of graphite.

In Chapter 5, we will show that nanoporous graphite with a honeycomb lattice architecture can be prepared by melt spinning iron-carbon alloys followed by chemical dissolution of the metal. The resulting material from as-spun ribbon was a freestanding carbon foam with hierarchical porosity; the sizes of the cells ranged from 2 – 5 μm, but the carbon walls that enclosed the cells contained nanometer sized pores. Annealing resulted in the disappearance of the submicron sized pores, but the open cell pore size remained unchanged by thermal treatment. Raman spectroscopy and TEM analysis revealed that the material consisted of amorphous carbon even after annealing and the BET surface area of the material was 4.5 m²/g.

1.3 Carbide Derived Carbons

Carbide-derived carbons (CDCs) are a classification of carbon materials derived from the selective removal of a metal/metalloid component from a precursor carbide (e.g., SiC, VC, Ti₃AlC₂). The morphologies of CDC materials include amorphous carbon, highly ordered graphite, graphene, nanotubes, diamond, carbon onions and porous carbon with varying pore sizes [2–5]; the structure depends on the choice of carbide precursor, the applied temperature and pressure, and the synthesis method [6]. An example of a CDC film grown on the surface of a Si/SiO₂ substrate by the treatment of TiC with hot chlorine gas is shown in Figure 1-2. The wide variety of CDC microstructures allow for diverse properties and therefore makes these materials suitable for a wide range of applications including, but not limited to, supercapacitor electrodes [7], tribological coatings [8], hydrogen storage [9], and protein sorption [10].

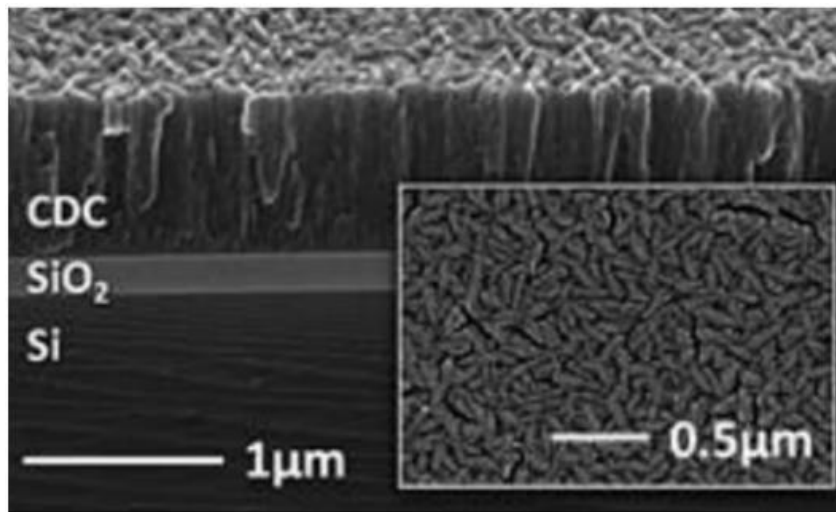


Figure 1-2. CDC film prepared by the chlorination of TiC. Reprinted from Ref. [11]

1.3.1 CDC Synthesis Methods

All CDC synthesis methods involve the selective extraction of the metal or metalloid atoms from a carbide material, transforming it into pure carbon. This transformation is conformal; that is, the resultant CDC material retains the macroscopic geometry of the parent material, even after a component is removed. This conservation of the original shape occurs because the carbon layer is formed by growth from the surface inwards, as opposed to a chemical or physical vapor deposition process where carbon is deposited as a layer on the exterior of a substrate. The three primary methods of CDC synthesis - halogenation, hydrothermal treatment and vacuum decomposition - will be discussed in detail in the subsequent sections.

1.3.1.1 Halogenation

Halogenation is the process in which the metal or metalloid atoms in the carbide are selectively etched upon exposure to a halogen-containing gas. Chlorination of Si was first reported by Hutchins [12] in 1917 and the following reaction was observed:



Initially, the C was considered as a waste byproduct in the synthesis of SiCl₄ until it was realized that the porous CDC was a valuable material [6]. While fluorine or fluorine-containing etchants such as HF can be used as the etching medium, chlorination has proven to be the most economical and well-studied method of CDC synthesis.

The carbon fabricated by treatment in pure chlorine gas is predominantly highly disordered and porous but often contains residual halogen or metal chlorides that can be removed by annealing [5]. Temperature also affects the resultant CDC structure; Presser [6] reported that at lower temperatures such as 600 °C for SiC chlorination, amorphous

carbon is the dominant morphology, but as temperatures reach 1000 °C, there is a significant increase in structural order of the carbon. Additionally, carbon nanotubes (CNTs), onions, barrel-like structures, and fullerenes have been reported as the product of chlorination of carbides [6].

1.3.1.2 Hydrothermal Decomposition

Hydrothermal CDC synthesis was first reported in the early 1990s. Hydrothermal decomposition involves the interaction of the carbide precursor with hot, high-pressure water in the range of 200 – 1000 °C and pressures of up to hundreds of MPa. Where M is the metal/metalloid element in the carbide, the main reaction to produce CDCs is:



However, alternate reactions that produce the byproducts CH₄, CO₂, CO and H₂ are also observed.

The carbon structure formed by this technique varies depending on the precursor and the processing conditions; for instance, amorphous porous graphite was grown on the surface of Tyranno fibers (amorphous SiO_xC_y with nanometer-sized β-SiC domains) at 300 – 400 °C and 100 MPa, whereas the formation of amorphous carbon, graphite, and diamond structured carbon was reported on the surface of α- and β-SiC powder and single crystals after treatments at 300 – 800 °C and 100 – 500 MPa [6,13–16].

1.3.1.3 Thermal Decomposition

Thermal decomposition of carbides takes advantage of carbon's high melting point to transform the carbide into carbon. Heat treatment of the precursor in a vacuum or in inert atmospheres facilitates the selective evaporation of the metal/metalloid element to form a variety of carbon morphologies, such as graphene, carbon nanotubes, and porous

carbon [6,17,18]. Kusunoki and others [18] synthesized self-organized carpets of carbon nanotubes by heat treating β -SiC single crystals to 1700 °C at 10^{-9} Torr with a laser. Unlike carbon nanotube formation via CVD, this process negated the use of metal catalysts and produced CNTs of the same chirality.

SiC is the most commonly utilized precursor for this method because it exists in various forms (powder, fibers, etc.), but also because it is readily available as large single crystals. However, SiC is anisotropic, and the differences in surface energy of the Si face (2.2 J m^{-2}) and the C-face (0.3 J m^{-2}) affect the type of carbon nanostructure formed and its growth rate. For example, Kusunoki [19] observed that under the same conditions, CNTs grew on the C-face but graphite sheets on the Si-face. The mechanism of C growth from SiC by decomposition was investigated by Badami [20], who reported that it requires 2-3 SiC bilayers to form a single graphene layer. As such, structural reorganization, facilitated by higher carbon mobility at elevated temperatures, was offered as an explanation for this occurrence.

Aluminum chloride was also investigated as a precursor for CDC growth. In 1958 Foster et al. [21] demonstrated the production of graphite single crystals by heating Al_4C_3 to temperatures above 2200 °C at atmospheric pressure, therefore proving that other carbides have potential as precursors in this particular CDC formation method.

1.3.2 Kinetics of CDC Transformations

Two primary kinetic regimes are observed in CDC fabrication. For thin CDC films, approximately 50 – 100 μm thick, the rate limiting step is the reaction between the halogen and the carbide, and the growth rate is linear with time [6]. The high degree of porosity in the CDC layer facilitates fast diffusion of SiCl_4 out of the pores (if the

halogen used is chlorine). For thicker CDC layers and longer halogenation times, there is a buildup of the byproduct gas at the transformation interface and the rate-limiting step becomes diffusion out of the porous layer. Under these conditions, the CDC growth rate varies with time as $t^{1/2}$ [22]. Figure 1-3 displays a CDC film grown via chlorination of SiC and a plot of CDC layer thickness against time. The linear kinetic regime is evident at the lower temperature and shorter chlorination times, and the transition to power-law diffusion mediated kinetics is observed as the CDC thickness increases.

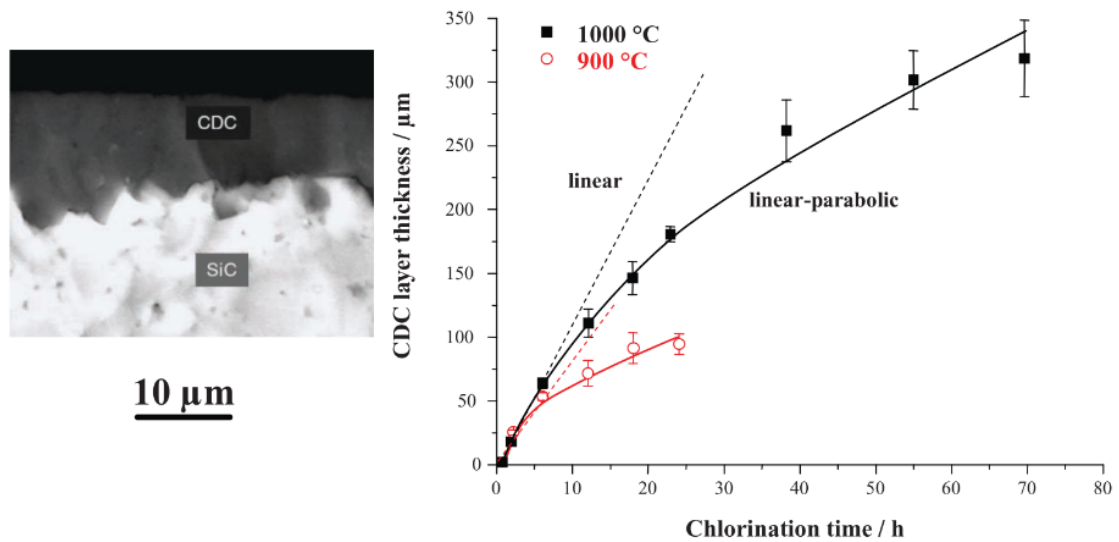


Figure 1-3. Sintered α -SiC in Ar + 3.5% Cl₂ (left). A plot of CDC layer thickness vs. reaction time at two temperatures (right). For a short time and low temperatures, linear kinetics dominate. At higher temperatures and longer reaction times, a parabolic time law is observed. Adapted from Ref. [6].

1.4 Dealloying

Dealloying is a facile materials processing technique used to fabricate a variety of bulk nanostructured materials. Conventionally, dealloying is a self-organization process that involves the selective dissolution of one or more of the components of a homogeneous alloy to yield a three-dimensional bicontinuous nanoporous network. The

morphology of nanoporous metals is unique. Other nanomaterials, such as nanoparticles, only contain regions of positive (or negative) curvature, while nanoporous metals contain regions of positive, negative, and saddle point curvature in a complex topology.

Furthermore, because mass transport is primarily via surface diffusion, there are no mechanisms to create defects like grain boundaries; the implication of this is that if a single crystal is dealloyed, the final dealloyed material is a porous single crystal.

Additionally, since the final structure evolves as a kinetic competition between the dissolution rate and interfacial diffusion rate of the remaining component, the length scale of the resultant microstructure is controlled dynamically rather than being intrinsic to the parent alloy and this length scale is on the dimension of nanometers [23–26].

These distinctive geometric features lend themselves to a variety of applications that utilize the materials' high surface area, open porosity and favorable mechanical properties. For example, Pounds et al. [27] used porous Nb reinforced with niobium silicide platelets [28] to fabricate working electrodes for the hydrogen evolution reaction in a sequential flow cell. Bai et al. [29] fabricated nanoporous Cu from an Al-Cu alloy for use as a low cost electrochemical actuator. Okulov et al. [30] dealloyed the surface of the Ti-6Al-7Nb by selective dissolution of the Al, leading to improved biocompatibility of the alloy.

Seminal studies on dealloying involved the use of an aqueous electrolyte to enable the selective removal of one species from an alloy. However, researchers have since identified alternative dealloying media that have further expanded the field to include dealloying via liquid metals, solid metals, or atmosphere. Changing the media changes the driving force for porosity evolution and ultimately leads to increasing the number of

materials compatible with the dealloying process. Figure 1-4 summarizes the four dealloying techniques currently in the literature. In each technique, differentiated from the other by the dealloying medium, element B is selectively removed from the parent alloy and a nanoporous structure comprised of element A remains. The dealloying process and its history will be described in further detail in the remainder of this section.

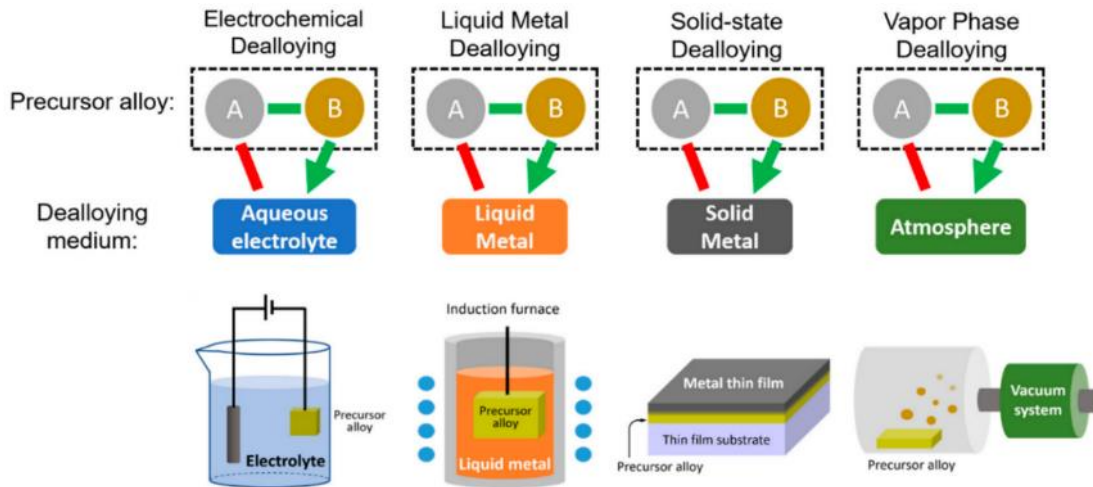


Figure 1-4. A schematic depicting the four dealloying techniques differentiated by the use of different dealloying media used to facilitate the selective removal of a component from an alloy. Typical setups for each experiment are also shown (Reused from Ref. [31])

1.4.1 Electrochemical Dealloying

One of the earliest recorded mentions of a dealloying process dates back to the second millennium B.C. in the pre-Columbian Andean era [32]. In a process referred to as depletion gilding, the ancient metallurgists enriched the surfaces of copper-silver-gold alloys, called tumbaga alloys, to achieve gold coloration by applying corrosive salts to the material surface that preferentially dissolved the less noble elements. Achieving a

more expensive finish while still maintaining the properties of the base alloy was culturally significant; the Incas considered gold “the sweat of the sun” and silver “the tears of the moon” and as such, these materials signified political power, social status and religious affiliations.

In more recent history, however, dealloying was often considered as a deleterious materials corrosion process. The dezincification of brasses has been studied since the 1800s [33] where, for example, the selective dissolution of zinc from Cu-Zn alloys in marine environments led to mechanical failure; it was observed that even though the part retained its original dimensions, the metal had no physical strength and displayed a structure of spongy copper [34]. Efforts to elucidate the mechanism by which this porosity evolves began in earnest in the 1960s. Pickering and Wagner [35] postulated that volume diffusion via divacancies was responsible for the observed porous pattern when Cu-Au and Cu-Zn alloys were submerged in electrolytes. However, this theory did not reconcile the requirement for unfeasible diffusion rates. In 1979, Forty [26] proposed a model whereby surface diffusion contributed to pit formation in a 50:50 Ag-Au alloy corroded with 50 % aqueous solution of nitric acid. The model claimed that atomic roughening of the alloy surface occurred by the selective dissolution of the less noble (LN) species, leaving behind silver vacancies or gold adatoms. Eventually, surface diffusion of the gold allowed for island nucleation and growth into the interconnected structure characteristic of dealloying. The proposed process, however, still included the possibility of mass transport of atoms through the bulk of the material or across the crystal surface to maintain dissolution.

While Pickering, Wagner and Forty provided the basis for modern study, the accurate working model for electrochemical dealloying was only introduced in 2001 by Erlebacher et al. [36] using a combination of kinetic Monte Carlo simulations and numerical solutions. The model is described in detail elsewhere [36,37] and summarized in Figure 1-5 using $\text{Ag}_{70}\text{Au}_{30}$ as a prototype, where Au is the more noble (MN) metal, meaning it has a higher positive standard reduction potential (1.5 V) than silver (0.80 V). Porosity evolution is driven by the application of a potential that lies between the reduction potentials of the two elements; this potential must be above a composition-dependent critical potential V_c to drive the reaction and may either be applied passively via free corrosion or actively by the application of a potential.

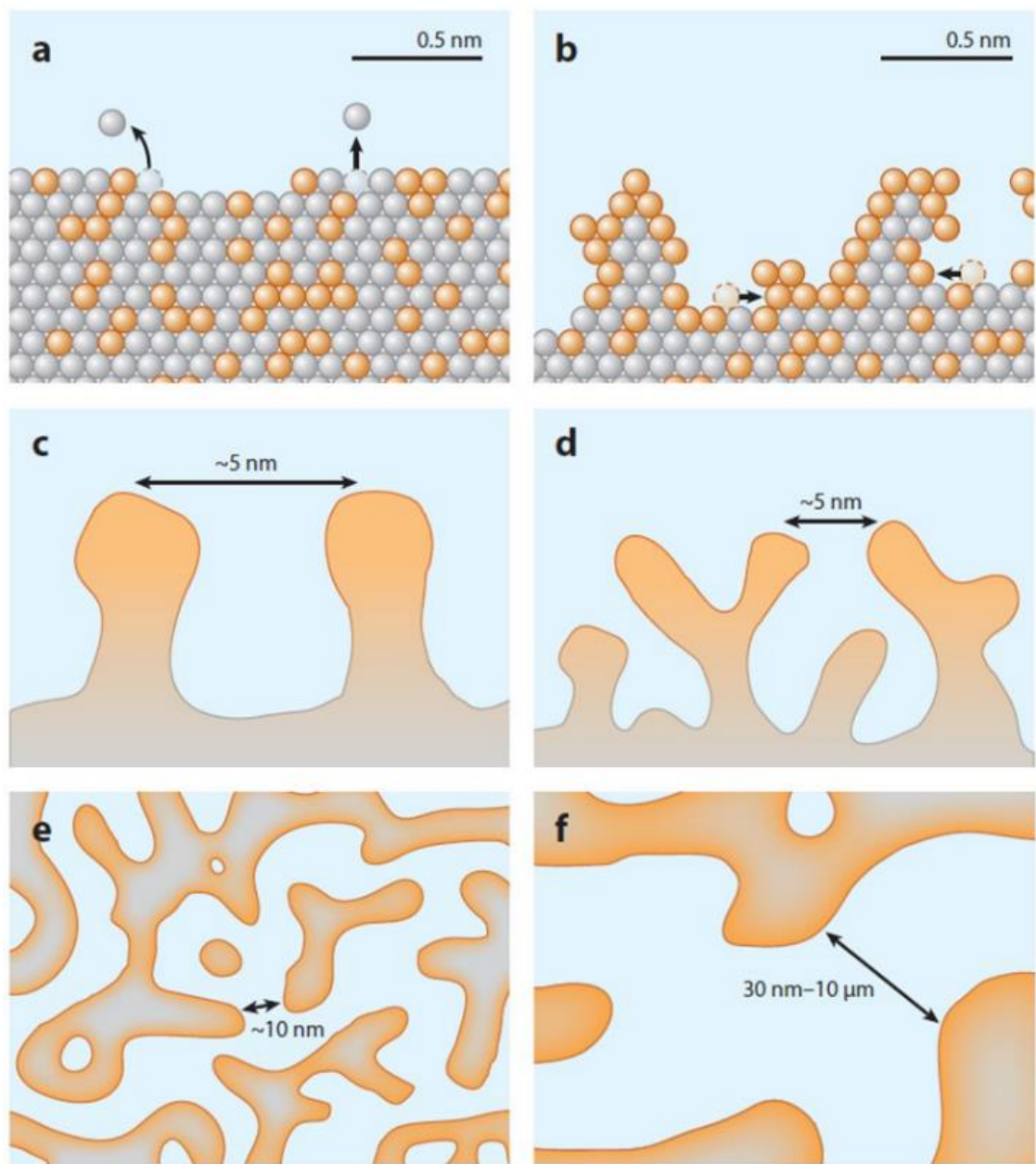


Figure 1-5. Working model for porosity in the Ag-Au alloy system (Ag, *grey*; Au, *orange*). (a) Ag atoms dissolve from terrace sites – the rate-limiting step. (b) Surface diffusion passivates low-coordination sites with Au, leading to surface roughening. (c-d) As dealloying proceeds, a large surface area develops, leading to exposure of undissolved Ag atoms. As a result, ligaments are undercut and bifurcated. (e) Nanoscale ligaments with Au-rich surface and Ag-rich interiors evolve. (f) As coarsening increases the length scale of the initial structure, residual Ag atoms are exposed and dissolved, leaving the final structure with a low Ag content.

Under these conditions, Ag atoms are easily solvated and extracted from low coordination sites. The rate-limiting step is the dissolution of a silver atom from a high coordination site such as a terrace, which leads to the formation of a terrace vacancy that grows laterally into a vacancy cluster as near-neighbors are extracted into solution. At first, the remaining Au species exist as adatoms but reorganize on the surface driven by uphill diffusional kinetics (Cahn-Hilliard) and capillary forces. The interfacial diffusion of the Au exposes fresh surfaces to dissolution, allowing dealloying to continue. Au clusters grow into mounds that bifurcate when the diffusion distance exceeds the threshold for efficient transport. The process of mound growth and bifurcation repeats, and so porosity proceeds into the bulk, and a bicontinuous structure is formed with 5-30 nm ligaments and pores [23,24,37]. An example of nanoporous gold prepared by dealloying a Au-Ag alloy in nitric acid is shown in Figure 1-6.

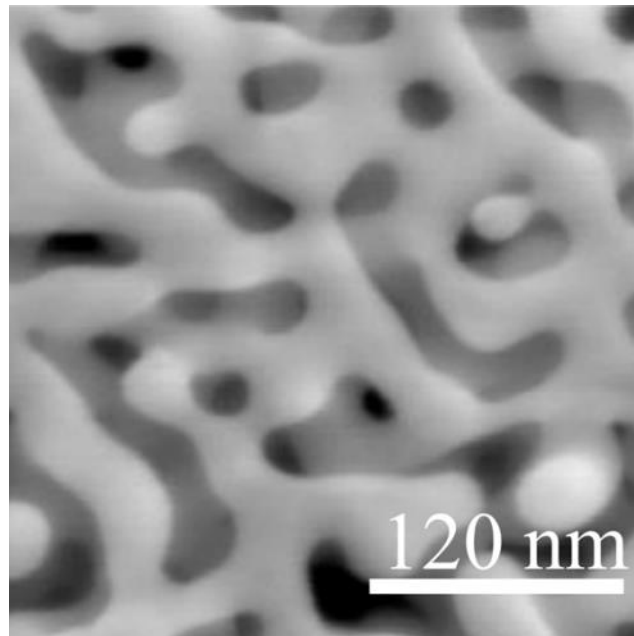


Figure 1-6. Scanning electron micrograph of nanoporous gold prepared by immersing $\text{Au}_{26}\text{Ag}_{74}$ in nitric acid. Adapted from Ref. [36]

1.4.2 Coarsening

Chen and Sieradzki [38] demonstrated that feature sizes scale linearly with the inverse homologous dealloying temperature $T_m/T_{dealloy}$: the ratio of the melting point of the remaining component to the dealloying temperature. Higher melting point materials, therefore, form finer features due to decreased surface mobility. The nanoporous structure is metastable and will undergo coarsening when annealed or electrochemically cycled; Figure 1-7 shows the coarsening of nanoporous gold dealloyed in nitric acid of increasing times. Coarsening is driven by two surface-diffusion mediated processes with a $t^{1/4}$ dependence: capillary effects and genus-reduction events. The driving force in the former is a reduction of surface area where there is mass transport from regions of high to regions of low curvature. The latter is driven by Rayleigh instabilities where ligaments pinch off to reduce the genus (number of “handles”) in the material [39].

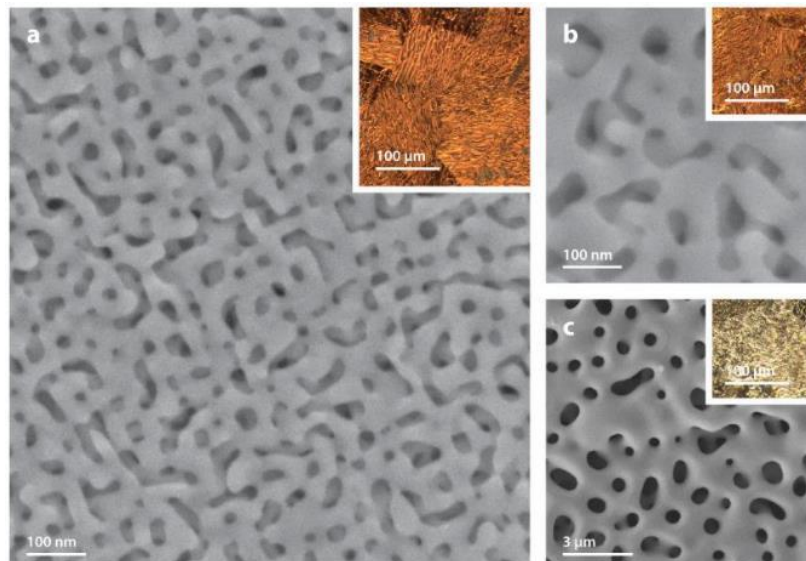


Figure 1-7. SEM and optical micrographs (insets) of nanoporous Au formed by free corrosion of a homogenous $\text{Ag}_{65}\text{Au}_{35}$ alloy in concentrated nitric acid. (a) The system was dealloyed for 24 h and exhibits ~ 30 nm features. (b) An additional 100 h treatment in acid results in feature sizes that coarsen to ~ 60 nm. (c) Features coarsen to several micrometers after thermal treatment at 800°C for 10 min in air (Reused from Reference [37]).

1.4.3 Conditions for Electrochemical Dealloying

The composition range of the parent alloy determines whether the structure will dealloy fully or at all; for materials dealloyed electrochemically, the range is limited to approximately 15-50 atomic percent of the more noble metal [37]. The parting limit - the upper end of the range - is the critical alloy composition necessary for complete dealloying; below this value, dealloying will not proceed to completion. In the case of Ag-Au, the parting limit is ~55 at. % Ag. Artymowicz [40] showed that there needs to exist a large enough chain or cluster of Ag atoms to facilitate solvation and dissolution by anions in the electrolyte; if there are fewer of the LN atoms in the alloy, they will become passivated by the MN species, effectively halting porosity evolution. At the other end of the range, the parent material dissolves and redeposits as particles instead of topologically complex porous structure [41].

The window of standard reduction potentials between the MN and LN components of the alloy needs to be large, hundreds of millivolts, for dealloying to proceed. For example, this difference for Ag and Au is ~ 1 V. On the other hand, if the reduction potential difference is too small, both elements simultaneously dissolve. For example, this potential difference is only ~ 500 mV for Ni and Cu; therefore, electrochemical dealloying cannot be performed with an alloy of these two components.

The surface diffusivity of the MN component is also an important consideration in electrochemical dealloying. If the surface diffusivity is too low (e.g., W), the atoms will not diffuse fast enough to form porous structures at the low temperatures typically used to perform ECD. In contrast, if the surface diffusivity is too high, the structure will passivate and prevent dealloying from occurring.

1.4.4 Liquid Metal Dealloying

Liquid Metal Dealloying (LMD) is a technique analogous to ECD in the fabrication of nanoporous materials. The major experimental difference, however, is that an aqueous electrolyte used as the liquid medium in ECD is replaced by liquid metal in LMD. The driving force for selective dissolution is differences in enthalpy of mixing between the alloy and the liquid metal. The major advantage of LMD is that it widens the set of materials that can be dealloyed since the essential requirements for ECD, discussed in Chapter 1.4.3, need not be met.

The LMD technique was first described by Harrison and Wagner [42] in 1959, where they successfully fabricated porous Ni by immersing a Cu-Ni parent alloy in molten silver and porous Cu by the preferential dissolution of Au in molten Bi from a Cu-Au parent alloy. Although the authors suggested potential applications for the technique, including catalysts or porous bearings containing lubricants, liquid metal dealloying did not garner popularity until 2011 with work published by Wada et al. [43]. These authors fabricated porous Ti by the liquid metal dealloying of a $\text{Ti}_{30}\text{Cu}_{70}$ melt spun ribbon in a Mg bath, demonstrating for the first time the evolution of porosity in less-noble metals.

Here, we will use Ta-Ti dealloyed in molten Cu to form nanoporous Ta as the model system to describe LMD further. As shown in the phase diagrams in Figure 1-8, this trio of elements exhibits the thermodynamic requirements that facilitate the formation of porosity: (i) Ta-Ti form a solid solution over a wide composition range, (ii) the enthalpy of mixing is positive between Ta and Cu, so Ta does not dissolve in the metal bath and (iii) the enthalpy of mixing is negative between Ti and Cu, meaning dissolution is favorable.

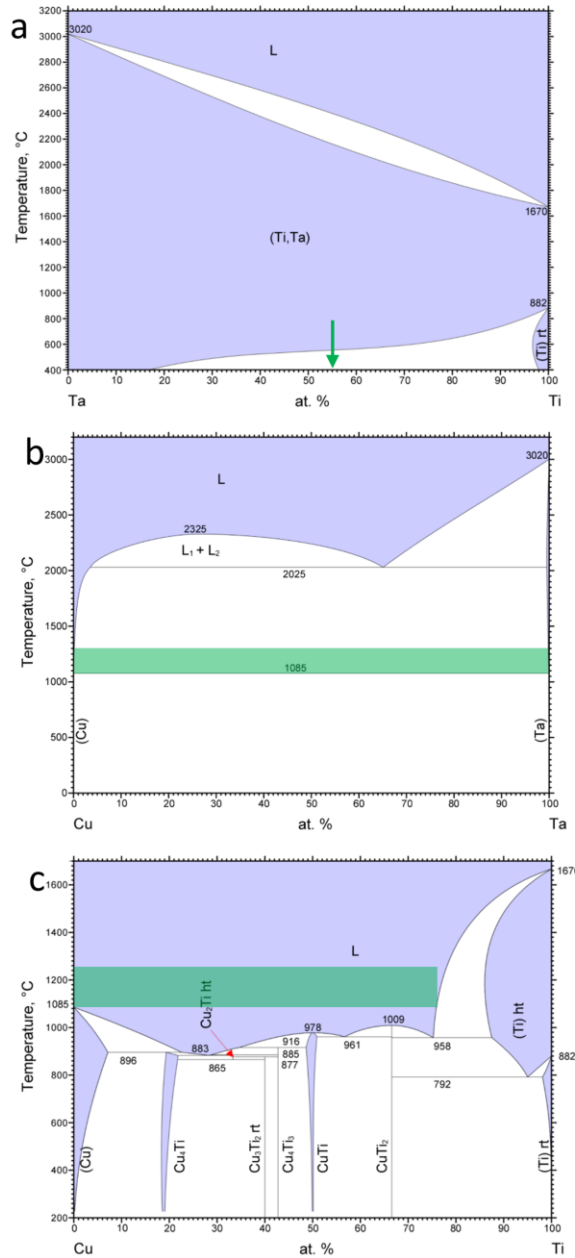


Figure 1-8. Phase diagrams used to determine that nanoporous Ta can be fabricated by liquid metal dealloying of a Ta-Ti alloy in molten Cu. (a) The Ti-Ta system forms a homogeneous solid solution over the entire composition range. The composition at $Ti_{55}Ta_{45}$ is highlighted as an example of a typical precursor alloy. (b) The Ta-Cu system shows limited solubility of Ta in Cu at temperatures investigated in LMD (highlighted by the green bar). (c) The Ti-Cu system shows that when small amounts of Ti (relative to Cu) are immersed in liquid Cu, dissolution occurs.

As depicted in Figure 1-9, the precursor alloy sample is immersed in the liquid Cu bath at the desired temperature, and the Ti is dissolved. As in ECD, the non-dissolved species (Ta) migrates along the alloy-melt interface and reorganizes into the porous structure characteristic of dealloying. However, upon termination of the process, pulling the alloy out of melt, the molten metal simply solidifies and a fully dense composite is formed that consists of the porous material with the dissolving medium solidified within the pores. This bicontinuous nanocomposite sometimes exhibits superior mechanical properties [37,44]. However, if a porous monolith is preferred, the dissolving metal can be excavated by chemical etching.

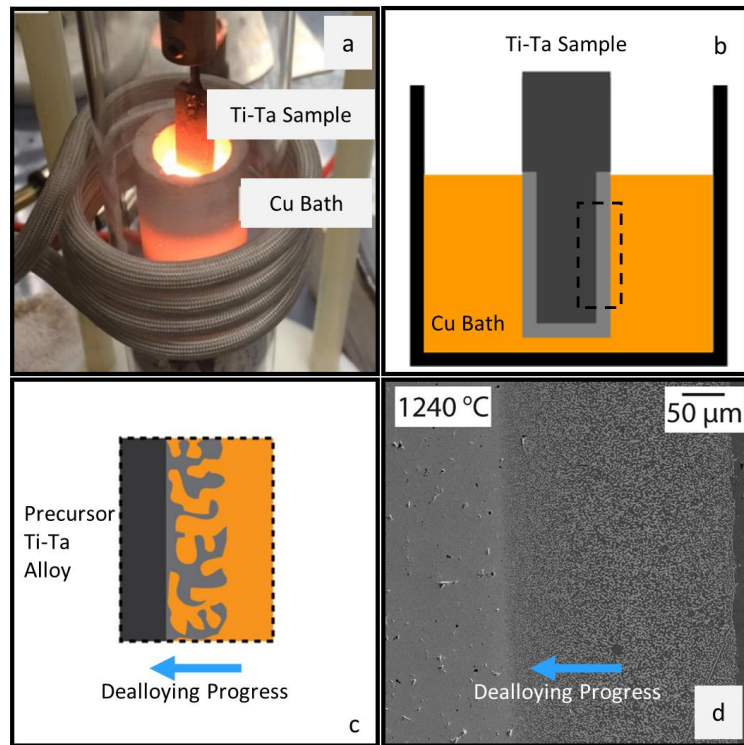


Figure 1-9. (a) A photograph showing a Ti-Ta sample being immersed in a liquid Cu bath heated by RF induction. (b-c) A schematic depicting porosity formation on the surface of the sample during LMD. (d) SEM micrograph of a sample of $Ti_{55}Ta_{45}$ dealloyed in Cu at 1240 °C for 20 s. The dealloying interface is sharp and flat, clearly delineating the undealloyed parent material on the left and the porous Ta-Cu composite on the right (Adapted from Ref. [45]).

The reintroduction of LMD has proven to be a significant advancement to the wider field of dealloying because it expands the set of materials systems to study when compared to ECD [37], see Figure 1-10. The electrochemistry of precious metals is well understood, but less noble metals rapidly oxidize or corrode in aqueous solvents, placing limitations on the set of materials that can be electrochemically dealloyed. In contrast, by using a liquid metal as the dissolution medium, a variety of new single and multi-component porous materials have been fabricated, e.g., porous Ta from Ta-Ti dealloyed in molten Cu [45], porous Nb/Nb₅Si₃ composite also dealloyed in molten Cu [28] and porous Si from Mg-Si dealloyed in molten Bi [46].

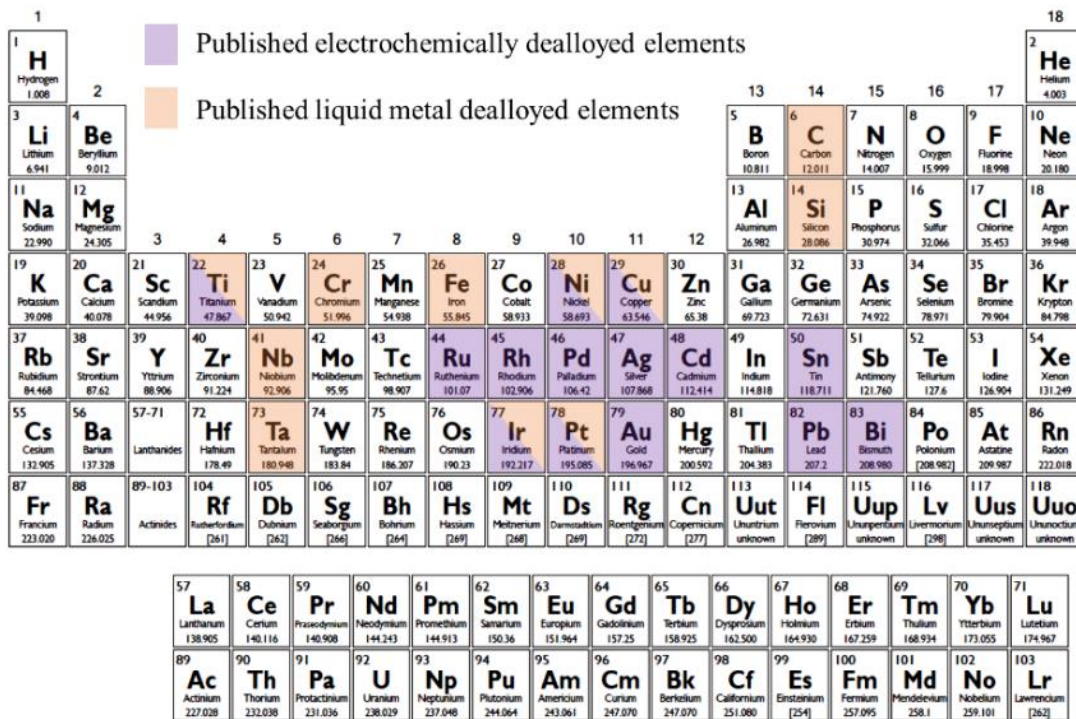


Figure 1-10. Periodic table (© 2015 Todd Helmenstine) highlighting elements that have been dealloyed electrochemically (purple) and elements that have been dealloyed via liquid metal dealloying (orange). Adapted from Ref. [47].

1.4.4.1 Liquid Metal Dealloying to Fabricate Porous Carbon

Most systems studied by LMD utilize alloy precursors that contain only metals or semi-metals, but recently nanographite was fabricated by selectively dissolving the metal from a metal-carbon precursor. Specifically, Yu et al. prepared a powder of composition $\text{Mn}_{85}\text{C}_{15}$ (particles size $\leq 100 \mu\text{m}$) and selectively dissolved Mn in molten Bi at 800°C to form a three-dimensional nanoporous graphite powder [48]. The Bi rich phase was removed by chemical etching in nitric acid. The parent material separated into $\alpha\text{-Mn}$ and Mn_{23}C_6 phases that revealed distinct structures after dealloying; see Figure 1-11.

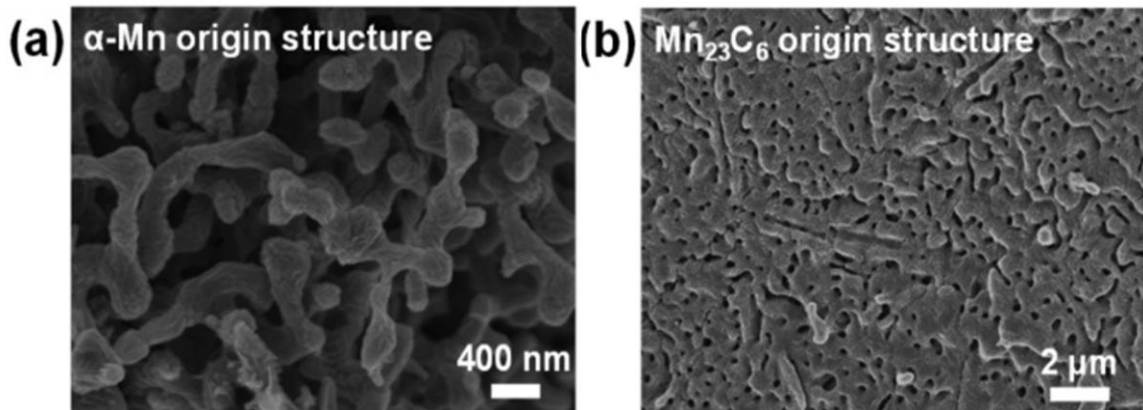


Figure 1-11. SEM images of porous C produced by the dealloying a Mn-C ingot in liquid Bi at 800°C for 600 s, following by removal of the Bi rich phase in HNO_3 . (a) Porous C developed from the dealloying of the $\alpha\text{-Mn}$ phase (b) Porous C developed from the dealloying of the Mn_{23}C_6 phase. Adapted from Ref. [48].

1.4.5 Comparison between Liquid Metal Dealloying and Electrochemical Dealloying

While the fundamental principle of dealloying – the selective dissolution of a component of an alloy – exists in both LMD and ECD, the effect of exchanging the aqueous dealloying medium in ECD for the liquid metal in LMD is worthy of closer examination. The major similarities between the two processes are described below:

- An interfacial pattern forming instability arises because of the kinetic competition between dissolution and surface diffusion. The process, described in further detail in Chapter 1.4.1, governs the evolution of porosity in both varieties of dealloying.
- The ligament diameters of porous materials fabricated by both LMD and ECD scale universally with the inverse “homologous dealloying temperature,” $T_m/T_{dealloy}$, which is the melting point of the nanoporous material divided by the dealloying processing temperature. Figure 1-12 depicts this correlation and indicates the dealloying duration as well since coarsening impacts how well the data fit the trend.

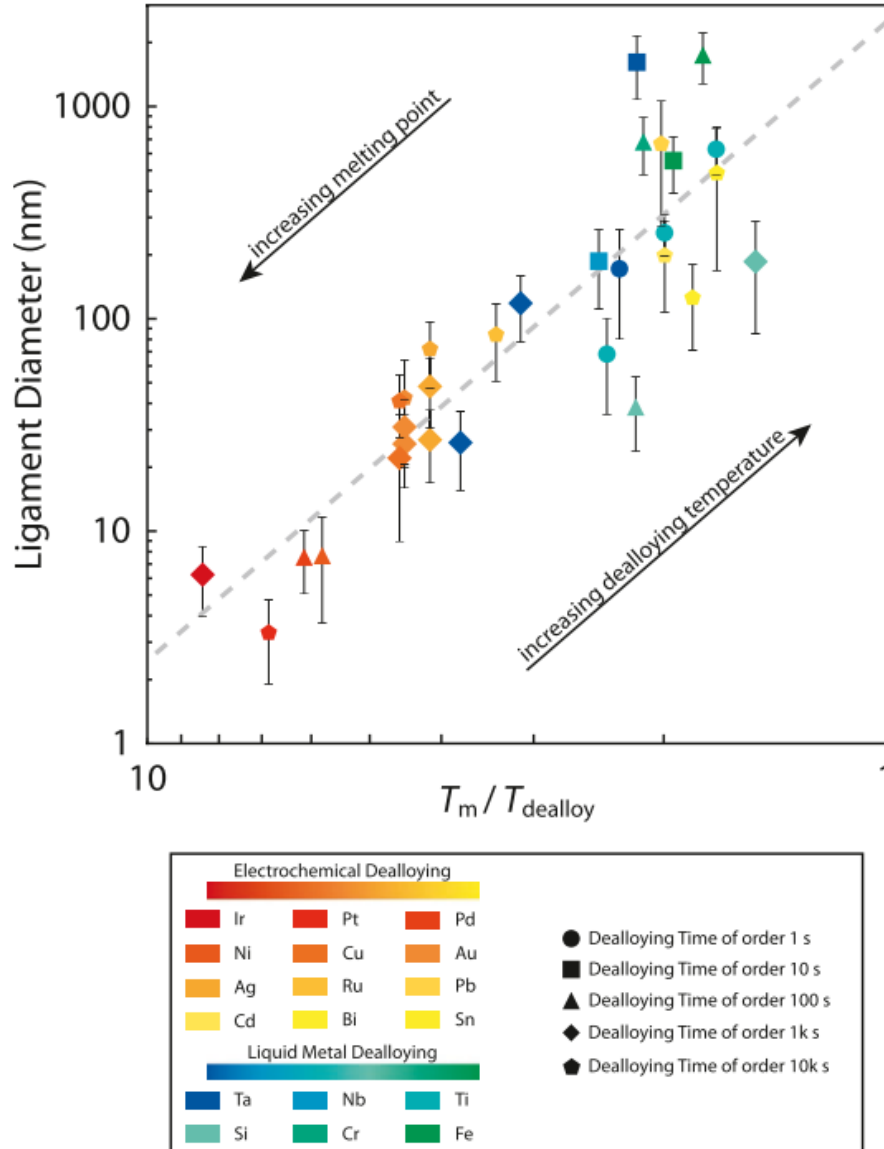


Figure 1-12. Universal trend in ligament diameter versus the inverse homologous temperature ($T_m/T_{dealloy}$) for ECD (red-to-yellow gradient) and LMD (blue-to-green gradient) at various dealloying times (different marker shapes.) The dealloying duration significantly impacts ligament diameter for low melting point elements and high dealloying temperatures, causing scatter at high homologous temperatures. Reprinted with permission from Ref. [47]

The major differences between the two processes are described below:

- The rate limiting behavior in the processes is not the same. In ECD, the diffusivity of oxidized metal ions in the electrolyte is very fast (on the order of 10^{-6} cm²/s) relative to dealloying interface velocities (~ 10 nm/s) [47,49], which leads to an effectively constant

dealloying velocity. Therefore, the rate limiting step in ECD is the attachment/detachment of the atoms from the solid-liquid interface. In contrast, the dealloying front velocity is much faster in LMD, on the order of 1 $\mu\text{m/s}$, while the diffusivity in the molten melt is about the same as in aqueous solvents. As a result, LMD is diffusion limited in the melt, and the interface velocity slows down with time as $t^{1/2}$ [45].

- In LMD, there is some dissolution and partitioning of the remaining component in the melt. The concentration of the dissolving species at the solid/liquid interface is in local equilibrium with the parent alloy and the concentration decays in a manner predicted by diffusional mathematics. The concentration of the dissolving component right at the interface can be as high as tens of percent, which increases the solubility of the “remaining” species in the liquid. Far from the interface, any of the “remaining” component that was dissolved will encounter a lower concentration of the dissolving species and will partition laterally back into the evolving porous structure.

These effects primarily manifest as differences in morphologies in ECD and LMD at varying mole fractions of the non-dissolving component in the parent alloy. There are two primary structures observed in ECD: (i) the prototypical three-dimensional bicontinuous network of pores and ligaments and (ii) particles, which form when the MN component fraction is low and the dissolution rate is high. A greater variety of morphologies, however, is seen in LMD, as shown in Figure 1-13. At low mole fractions (5 at. %) of the remaining component, particles are still formed. At intermediate mole fractions (15 at. %), a lamellar morphology is observed, a microstructure never observed

in ECD. At high mole fractions of the non-dissolving component (35 at. %), the expected bicontinuous interconnected structure is formed.

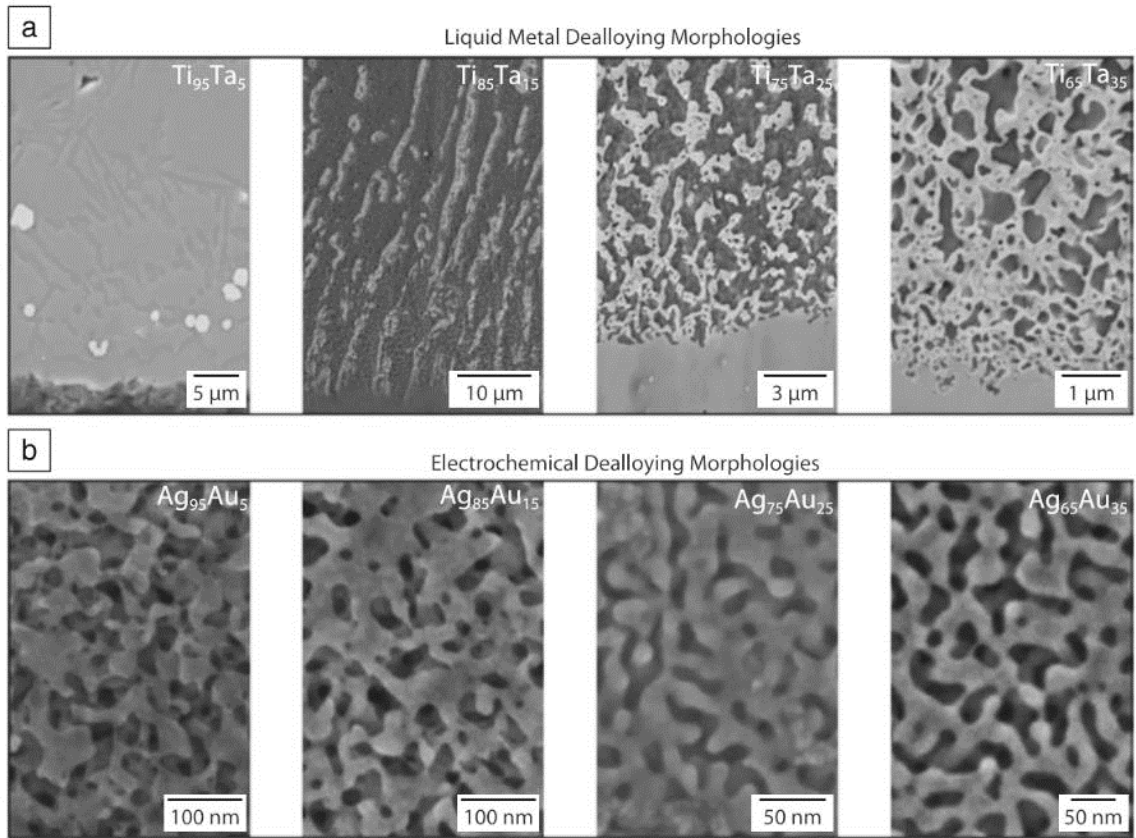


Figure 1-13. Comparison of dealloyed morphologies formed in liquid metal and aqueous electrolyte as a function of parent alloy composition. (a) Ti_xTa_{1-x} dealloyed in molten Cu via liquid metal dealloying; at low Ta concentrations, the dealloyed morphology forms droplets and lamella and as the Ta content increases, the dealloyed morphology becomes interconnected. (b) Ag_xAu_{1-x} dealloyed in concentrated HNO_3 via electrochemical dealloying; the dealloyed structure is bicontinuous for all Au concentrations. Reused with permission from Ref. [47].

1.5 Melt Spinning

Melt spinning is a rapid solidification technique first patented by British scientists Strange and Pim [50] in 1908 to manufacture sheets and ribbons of lead, zinc, and other alloys. In this process, a molten stream of metal is ejected onto a rotating substrate which extracts heat from the melt and expels a quenched ribbon. Conventional solidification typically proceeds at cooling rates lower than 100 K/s and generally results in phases and microstructures predicted by equilibrium thermodynamics [51]. However, melt spinning is a far-from-equilibrium cooling technique where solidification rates between $10^4 - 10^7$ K/s are encountered [52]. As a result, phases and microstructures that are favored kinetically instead of thermodynamically may evolve. The technique saw a resurgence in popularity in the 1960s and early 1970s when Pond and Maddin [53] investigated extended solid solubility in Cu-Au filaments prepared by ejecting a melt on the inside of a rotating drum and Chen and Miller [54] prepared amorphous alloys by ejecting melts between a pair of rapidly rotating steel rollers held together under pressure.

Continuous casting of alloys by melt spinning can be achieved by a variety of experimental arrangements, often differentiated by the type of rotating substrate used to facilitate rapid quenching. In the setup described by Strange and Pim [50], the melt is impinged on the exterior surface of a rotating wheel, and of this type, there are two primary variations: planar flow casting (PFC) and free jet melt spinning (FJMS). The difference between the two is the distance between the nozzle from which the liquid metal is expelled and the surface of the solidification substrate, where this distance is large (several millimeters) in FJMS and so small (< 1 mm) in PFC that the melt is simultaneously in contact with the nozzle and the spinning wheel [55]. The advantage of

the latter is that the constrained melt pool damps perturbations and leads to uniform ribbon thickness and smooth ribbon edges. Wheel substrate roughness or surface contaminants, entrapped gas molecules, or imperfections in the crucible nozzle also lead to instability of the melt pool and can result in non-uniformity in the ribbon and edge serrations [55,56].

Several applications that take advantage of the unique geometry of melt-spun materials and their far-from-equilibrium microstructures have been explored. A few examples are highlighted below. In 2014, Zhang et al. [57] prepared nanocrystalline and amorphous Mg-Nd-Ni-Cu based alloys by melt spinning and demonstrated the material's potential utility in hydrogen storage. Shelyakov [58] and colleagues prepared a micromechanical device – microtweezers – by melt spinning the shape memory alloy $Ti_{50}Ni_{25}Cu_{25}$ (at. %). High silicon steels prepared by melt spinning have also been considered for their potential in the use of distribution transformers due to the material's superior mechanical properties when compared to traditional fabrication methods [59].

1.5.1 Working Principle

A schematic of the planar flow casting melt spinning method, referred to simply as melt spinning henceforth, is shown in Figure 1-14. The solid alloy is placed into a crucible heated to some temperature above its melting point. A back-pressure is applied to the molten metal which is ejected from the crucible nozzle onto a rotating wheel that functions as a heat sink. Upon impingement, the liquid metal forms a melt pool that acts as a local reservoir from which quenched ribbon is continuously expelled. The shape of the melt pool is formed from the counteracting forces of tangential flow of the material and its surface tension [60].

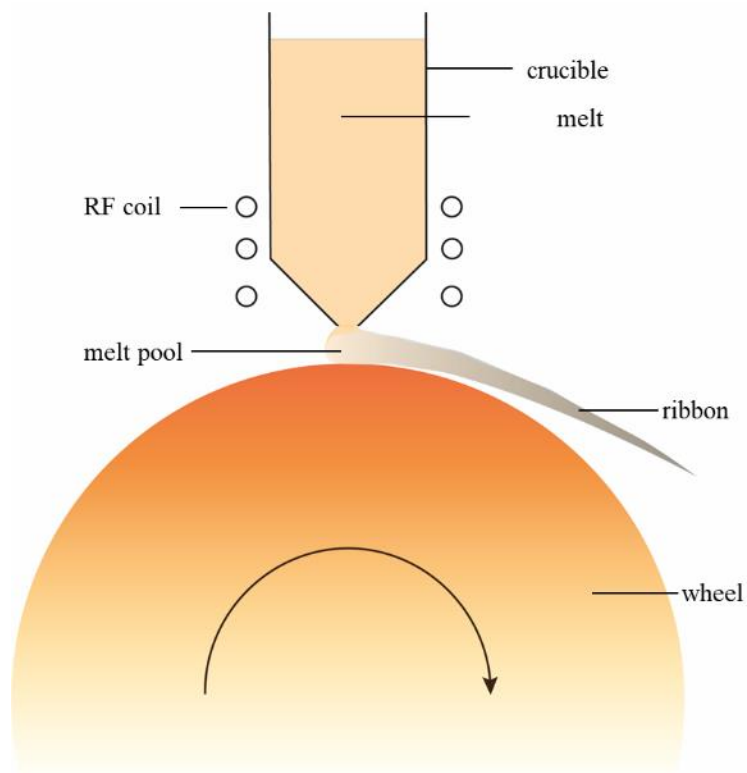


Figure 1-14. A schematic diagram of the melt spinning process. The liquid melt is impinged on a rotating wheel where it forms a melt pool from which solidified ribbon is expelled.

1.5.2 Microstructural Evolution

In addition to its function as a heat sink, the wheel surface provides heterogeneous nucleation sites for the growth of solid phases. A schematic representation of ribbon microstructure is found in Figure 1-15. Typically, solidification begins in the form of fine, equiaxed crystals and extends laterally until the contact surface is covered. From this initial chill zone, columnar grains grow in the direction parallel to the thermal gradient, i.e., normal to the ribbon surface. In Ni alloys, the preferential growth direction of the columnar grains is the [100] orientation [55]. With sufficient cooling rates, the early stage of columnar solidification is partitionless; that is, the solidification velocity is faster than the diffusion of solutes, which become trapped in the solid phase. The

equilibrium partition coefficient ($k = c_S/c_L$) is generally less than unity but can approach $k = 1$ in rapid solidification processes [61], and the equilibrium solid solubility can be greatly exceeded. As the solidification front advances from the contact surface to the free surface, the latent heat of solidification is released, reducing the thermal gradient and the interface velocity. When solidification is no longer partitionless, the microstructure of the ribbon transitions into a cellular configuration with much larger grains.

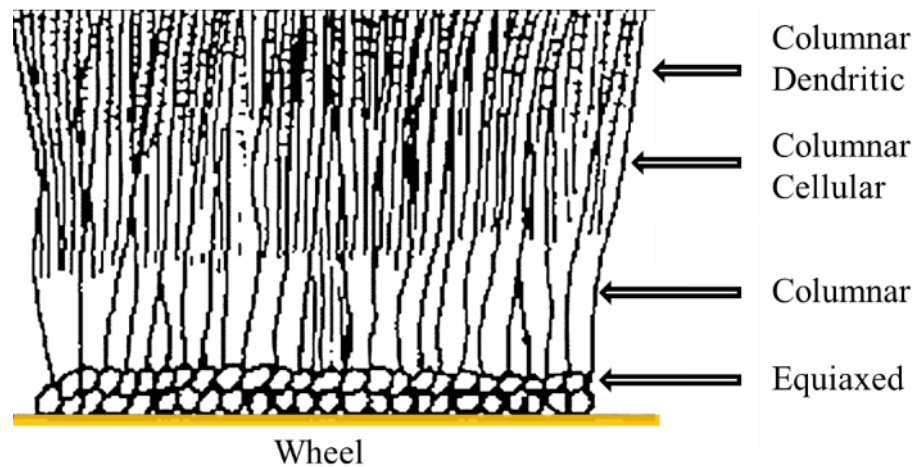


Figure 1-15. Schematic representation of the microstructure typically found in melt spun ribbons. Adapted from Ref. [55].

1.5.3 Experimental Parameters That Affect the Cooling Rate

The unique properties and microstructures of alloys synthesized by melt spinning are strongly dependent on the experimental cooling rate. As a result, several studies have sought to elucidate the effect of various processing conditions on the cooling rates encountered in melt spinning [62–64].

Many experimental parameters affect the cooling rate, including the nozzle-wheel gap, melt superheat, the ejection gas pressure, wheel material and its surface finish, and the wheel velocity. These parameters primarily affect the ribbon thickness and

researchers have often described it as the most important feature of melt-spun material as its value is highly correlated with the cooling rate; the average cooling rate increases approximately as the inverse square of ribbon thickness for ideal cooling [55,62,65]. A selected few of these factors are discussed in further detail below.

1.5.3.1 Wheel Speed

According to a relationship between wheel speed V_s and ribbon thickness h experimentally derived by Tkatch et al. [62], $d \propto V_s^{1.3}$ and in the case where the wheel speed was the experimental variable, the cooling rate \dot{T} was determined to be $\dot{T} \propto d^{-2}$ for ideal cooling. Therefore, the cooling rate is directly proportional to the wheel velocity and inversely to the square of ribbon thickness. Increasing the wheel velocity increases the cooling rate due to improved thermal contact between the ribbon and the substrate, but also because it results in a decrease in ribbon thickness [51].

1.5.3.2 Melt Ejection Temperature

Ribbon thickness tends to decrease with the melt ejection temperature. One explanation proffered by scientists [62] is that, dictated by a momentum transfer mechanism, liquid metals at high temperatures have lower viscosities, and these lower viscosities lead to a thinner melt layer extracted by the wheel from the melt pool. Fiedler et al. [66] also provided an alternate explanation for the observed relationship where the increasing surface tension of Fe-based alloys with temperature led to the decrease in ribbon thickness.

1.5.3.3 Melt Ejection Pressure

The effect of the pressure at which the melt is ejected into the rotating wheel P_E on the cooling rate is complex. On one hand, increasing the ejection pressure results in

increased contact time between the ribbon and the wheel surface, allowing for improved heat transfer. However, in agreement with Bernoulli's equations for fluid flow, thickness h varies linearly with $P_E^{\frac{1}{2}}$, that is, ribbon thickness also increases with ejection pressure, which is manifested as a decrease in the cooling rate.

1.6 Raman Spectroscopy

Raman spectroscopy is a standard tool used in the characterization of carbon materials [67]. In this technique, a source of monochromatic light, usually a laser, is incident upon a material and interacts with its vibrational modes. This interaction results in Raman scattering where the energy of the incoming photon is shifted up or down.

Modern Raman instruments are simple to operate, fast, and non-destructive to samples while allowing researchers to elucidate structural and electronic information about a material [68]. Raman spectra provide fingerprints that allow the identification of a material, and specifically for carbon materials, the technique allows the determination of the crystallite size, the defect concentration, the number of layers present in graphitic material and the presence of dopants [69–71].

The most prominent features in the Raman fingerprint of graphitic samples are the G, D and 2D bands. The G peak located at $\sim 1580 \text{ cm}^{-1}$ is activated by the stretching modes of carbon rings and is present in all sp^2 hybridized carbon materials. The D peak, found at $\sim 1350 \text{ cm}^{-1}$, is produced via breathing modes of carbon rings and is only activated in the presence of defects. A schematic depicting the vibrational modes of these two peaks is shown in Figure 1-16. An additional defect activated peak, the D' peak, sometimes appears at $\sim 1620 \text{ cm}^{-1}$ as a shoulder on the G peak. The 2D band appears at \sim

2700 cm^{-1} and is intense in the Raman fingerprint of highly crystalline graphitic materials. Although it is the second order of the D peak, its presence is not indicative of defects. Examples of Raman spectra of carbon materials can be found in Chapters 2.4.4 and 4.4.4.

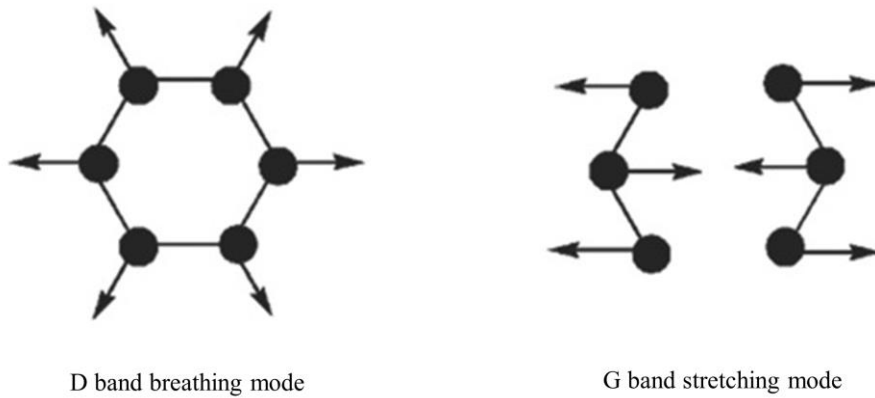


Figure 1-16. Motions of the atoms in graphitic materials that give rise to the D peak (left) and the G peak (right). Adapted from Ref. [72].

1.7 References

- [1] V. Negri, J. Pacheco-Torres, · Daniel Calle, · Pilar López-Larrubia, Carbon Nanotubes in Biomedicine, *Top. Curr. Chem.* 378 (2020) 15.
<https://doi.org/10.1007/s41061-019-0278-8>.
- [2] Y. Gogotsi, A. Nikitin, H. Ye, W. Zhou, J.E. Fischer, B. Yi, H.C. Foley, M.W. Barsoum, Nanoporous carbide-derived carbon with tunable pore size, *Nat. Mater.* 2 (2003) 591–594. <https://doi.org/10.1038/nmat957>.
- [3] G. Yushin, E.N. Hoffman, M.W. Barsoum, Y. Gogotsi, C.A. Howell, S.R. Sandeman, G.J. Phillips, A.W. Lloyd, S. V. Mikhalovsky, Mesoporous carbide-derived carbon with porosity tuned for efficient adsorption of cytokines, *Biomaterials.* 27 (2006) 5755–5762.
<https://doi.org/10.1016/J.BIOMATERIALS.2006.07.019>.
- [4] Y.G. Gogotsi, M. Yoshimura, Formation of carbon films on carbides under hydrothermal conditions, *Nature.* 367 (1994) 628–630.
<https://doi.org/10.1038/367628a0>.
- [5] S. Welz, M.J. McNallan, Y. Gogotsi, Carbon structures in silicon carbide derived carbon, *J. Mater. Process. Technol.* 179 (2006) 11–22.
<https://doi.org/10.1016/J.JMATPROTEC.2006.03.103>.
- [6] V. Presser, M. Heon, Y. Gogotsi, Carbide-Derived Carbons - From Porous Networks to Nanotubes and Graphene, *Adv. Funct. Mater.* 21 (2011) 810–833.
<https://doi.org/10.1002/adfm.201002094>.
- [7] P. Simon, Y. Gogotsi, Materials for electrochemical capacitors, *Nat. Mater.* 7 (2008) 845–854. <https://doi.org/10.1038/nmat2297>.
- [8] Y.-S. Chun, D.-S. Lim, Carbide derived carbon: from growth to tribological application, *J. Ceram. Soc. Japan.* 122 (2014) 577–585.
<https://doi.org/10.2109/jcersj2.122.577>.

- [9] Y. Gogotsi, R.K. Dash, G. Yushin, T. Yildirim, G. Laudisio, J.E. Fischer, Tailoring of nanoscale porosity in carbide-derived carbons for hydrogen storage, *J. Am. Chem. Soc.* 127 (2005) 16006–16007. <https://doi.org/10.1021/ja0550529>.
- [10] S. Yachamaneni, G. Yushin, S.H. Yeon, Y. Gogotsi, C. Howell, S. Sandeman, G. Phillips, S. Mikhalovsky, Mesoporous carbide-derived carbon for cytokine removal from blood plasma, *Biomaterials*. 31 (2010) 4789–4794. <https://doi.org/10.1016/j.biomaterials.2010.02.054>.
- [11] M. Heon, S. Lofland, J. Applegate, R. Nolte, E. Cortes, J.D. Hettinger, P.-L. Taberna, P. Simon, P. Huang, M. Brunet, Y. Gogotsi, Continuous carbide-derived carbon films with high volumetric capacitance, *Energy Environ. Sci.* 4 (2011) 135. <https://doi.org/10.1039/c0ee00404a>.
- [12] O. Hutchins, Method for the Production of Silicon Tetrachlorid., US1271713A, 1917. <https://patents.google.com/patent/US1271713A/en> (accessed February 5, 2021).
- [13] R. Roy, D. Ravichandran, A. Badzian, E. Breval, Attempted hydrothermal synthesis of diamond by hydrolysis of β -SiC powder, *Diam. Relat. Mater.* 5 (1996) 973–976. [https://doi.org/10.1016/0925-9635\(95\)00443-2](https://doi.org/10.1016/0925-9635(95)00443-2).
- [14] R. Riedel, ed., *Handbook of Ceramic Hard Materials*, Wiley, 2000. <https://doi.org/10.1002/9783527618217>.
- [15] T. Kraft, K.G. Nickel, Y.G. Gogotsi, Hydrothermal degradation of chemical vapour deposited SiC fibres, *J. Mater. Sci.* 33 (1998) 4357–4364. <https://doi.org/10.1023/A:1004480814477>.
- [16] Y.G. Gogotsi, Structure of carbon produced by hydrothermal treatment of β -SiC powder, *J. Mater. Chem.* 6 (1996) 595–604. <https://doi.org/10.1039/JM9960600595>.
- [17] E. Rollings, G.H. Gweon, S.Y. Zhou, B.S. Mun, J.L. McChesney, B.S. Hussain, A. V. Fedorov, P.N. First, W.A. de Heer, A. Lanzara, Synthesis and characterization

- of atomically thin graphite films on a silicon carbide substrate, *J. Phys. Chem. Solids.* 67 (2006) 2172–2177. <https://doi.org/10.1016/j.jpcs.2006.05.010>.
- [18] M. Kusunoki, M. Rokkaku, T. Suzuki, Epitaxial carbon nanotube film self-organized by sublimation decomposition of silicon carbide, *Appl. Phys. Lett.* 71 (1997) 2620–2622. <https://doi.org/10.1063/1.120158>.
- [19] M. Kusunoki, T. Suzuki, T. Hirayama, N. Shibata, Aligned carbon nanotube films on SiC(0001) wafers, *Phys. B Condens. Matter.* 323 (2002) 296–298. [https://doi.org/10.1016/S0921-4526\(02\)01027-X](https://doi.org/10.1016/S0921-4526(02)01027-X).
- [20] D. V. Badami, X-Ray studies of graphite formed by decomposing silicon carbide, *Carbon.* 3 (1965) 53–57. [https://doi.org/10.1016/0008-6223\(65\)90027-8](https://doi.org/10.1016/0008-6223(65)90027-8).
- [21] L.M. Foster, G. Long, H.C. Stumpf, Production of graphite single crystals by the thermal decomposition of aluminum carbide, *Am. Mineral.* 43 (1958) 258–296.
- [22] A. Lee, R. Zhu, M. McNallan, Kinetics of conversion of silicon carbide to carbide derived carbon, *J. Phys. Condens. Matter.*, 18 (2006).
- [23] J. Rugolo, J. Erlebacher, K. Sieradzki, Length scales in alloy dissolution and measurement of absolute interfacial free energy, *Nat. Mater.* 5 (2006) 946–949. <https://doi.org/10.1038/nmat1780>.
- [24] J. Erlebacher, M.J. Aziz, A. Karma, N. Dimitrov, K. Sieradzki, Evolution of nanoporosity in dealloying, *Nature.* 410 (2001) 450–3. <https://doi.org/10.1038/35068529>.
- [25] J. Erlebacher, An Atomistic Description of Dealloying, *J. Electrochem. Soc.* 151 (2004) C614–C626. <https://doi.org/10.1149/1.1784820>.
- [26] A.J. Forty, Corrosion micromorphology of noble metal alloys and depletion gilding, *Nature.* 282 (1979) 597–598. <https://doi.org/10.1038/282597a0>.
- [27] T. Pounds, E.E. Benn, A. Carter, J. Erlebacher, Sequential Electrochemical Flow

- Cell for Complex Multicomponent Electrocatalysis, *J. Electrochem. Soc.* 167 (2020) 106510. <https://doi.org/10.1149/1945-7111/ab9bfc>.
- [28] B. Gaskey, I. McCue, A. Chuang, J. Erlebacher, Self-assembled porous metal-intermetallic nanocomposites via liquid metal dealloying, *Acta Mater.* 164 (2019) 293–300. <https://doi.org/10.1016/J.ACTAMAT.2018.10.057>.
- [29] Q. Bai, C. Zhang, F. Tan, F. Wu, Z. Zhang, Nanoporous copper as an inexpensive electrochemical actuator responsive to sub-volt voltages, *Electrochem. Commun.* (2021). <https://doi.org/10.1016/j.elecom.2021.106940>.
- [30] I.V. Okulov, S.-H. Joo, A.V. Okulov, A.S. Volegov, B. Luthringer, R. Willumeit-Römer, L. Zhang, L. Mädler, J. Eckert, H. Kato, Surface Functionalization of Biomedical Ti-6Al-7Nb Alloy by Liquid Metal Dealloying, *Nanomaterials.* 10 (2020) 1479. <https://doi.org/10.3390/nano10081479>.
- [31] A. Chuang, J. Erlebacher, Challenges and Opportunities for Integrating Dealloying Methods into Additive Manufacturing, *Materials.* 13 (2009) 3706. <https://doi.org/10.3390/ma13173706>.
- [32] H. Lechtman, Pre-Columbian Surface Metallurgy, *Sci. Am.* 250 (1984) 56–63. <https://doi.org/10.2307/24969389>.
- [33] C. Calvert, R. Johnson, Action of Acids upon Metals and Alloys, *J. Chem. Soc.* 19 (1866) 434–454. <https://doi.org/https://doi.org/10.1039/JS8661900434>.
- [34] L. Kenworthy, W.G. O’Driscoll, B.L. Kenworthy, Dezincification of Brasses, *Anti-Corrosion Methods Mater.* 2 (1955) 247–249. <https://doi.org/10.1108/eb019087>.
- [35] H.W. Pickering, C. Wagner, Electrolytic Dissolution of Binary Alloys Containing a Noble Metal, *J. Electrochem. Soc.* 114 (1967) 698. <https://doi.org/10.1149/1.2426709>.
- [36] J. Erlebacher, M.J. Aziz, A. Karma, N. Dimitrov, K. Sieradzki, Evolution of

nanoporosity in dealloying, *Nature*. 410 (2001) 450–453.
<https://doi.org/10.1038/35068529>.

- [37] I. McCue, E. Benn, B. Gaskey, J. Erlebacher, Dealloying and Dealloyed Materials, *Annu. Rev. Mater. Res.* 46 (2016) 263–286. <https://doi.org/10.1146/annurev-matsci-070115-031739>.
- [38] Q. Chen, K. Sieradzki, Spontaneous evolution of bicontinuous nanostructures in dealloyed Li-based systems, *Nat. Mater.* 12 (2013) 1102–1106.
<https://doi.org/10.1038/nmat3741>.
- [39] J. Erlebacher, Mechanism of coarsening and bubble formation in high-genus nanoporous metals, *Phys. Rev. Lett.* 106 (2011).
<https://doi.org/10.1103/PhysRevLett.106.225504>.
- [40] D.M. Artymowicz, J. Erlebacher, R.C. Newman, Relationship between the parting limit for de-alloying and a particular geometric high-density site percolation threshold, *Philos. Mag.* 89 (2009) 1663–1693.
<https://doi.org/10.1080/14786430903025708>.
- [41] T. Pounds, *Applied Electrochemistry of Porous Metals*, Johns Hopkins University, 2019. <http://jhir.library.jhu.edu/handle/1774.2/61455> (accessed January 19, 2021).
- [42] J.D. Harrison, C. Wagner, The attack of solid alloys by liquid metals and salt melts, *Acta Metall.* 7 (1959) 722–735. [https://doi.org/10.1016/0001-6160\(59\)90178-6](https://doi.org/10.1016/0001-6160(59)90178-6).
- [43] T. Wada, K. Yubuta, A. Inoue, H. Kato, Dealloying by metallic melt, *Mater. Lett.* 65 (2011) 1076–1078. <https://doi.org/10.1016/J.MATLET.2011.01.054>.
- [44] I. McCue, B. Gaskey, B. Crawford, J. Erlebacher, Local heterogeneity in the mechanical properties of bicontinuous composites made by liquid metal dealloying, *Appl. Phys. Lett.* 109 (2016) 231901.
<https://doi.org/10.1063/1.4971776>.

- [45] I. McCue, B. Gaskey, P.-A. Geslin, A. Karma, J. Erlebacher, Kinetics and morphological evolution of liquid metal dealloying, *Acta Mater.* 115 (2016) 10–23. <https://doi.org/10.1016/J.ACTAMAT.2016.05.032>.
- [46] T. Wada, J. Yamada, H. Kato, Preparation of three-dimensional nanoporous Si using dealloying by metallic melt and application as a lithium-ion rechargeable battery negative electrode, *J. Power Sources.* 306 (2016) 8–16. <https://doi.org/10.1016/J.JPOWSOUR.2015.11.079>.
- [47] I. McCue, A. Karma, J. Erlebacher, Pattern formation during electrochemical and liquid metal dealloying, *MRS Bull.* 43 (2018) 27–34. <https://doi.org/10.1557/mrs.2017.301>.
- [48] S.-G. Yu, K. Yubuta, T. Wada, H. Kato, Three-dimensional bicontinuous porous graphite generated in low temperature metallic liquid, *Carbon.* 96 (2016) 403–410. <https://doi.org/10.1016/j.carbon.2015.09.093>.
- [49] Y.K. Chen-Wiegart, S. Wang, I. McNulty, D.C. Dunand, Effect of Ag–Au composition and acid concentration on dealloying front velocity and cracking during nanoporous gold formation, *Acta Mater.* 61 (2013) 5561–5570. <https://doi.org/10.1016/J.ACTAMAT.2013.05.039>.
- [50] E.H. Strange, C.A. Pim, Process of manufacturing thin sheets, foil, strips, or ribbons of zinc, lead, or other metal or alloy., US905758A, 1908. <https://patents.google.com/patent/US905758A/en> (accessed February 7, 2021).
- [51] H. Jones, The status of rapid solidification of alloys in research and application, *J. Mater. Sci.* 19 (1984) 1043–1076. <https://doi.org/10.1007/BF01120015>.
- [52] B. Cantor, W.T. Kim, B.P. Bewlay, A.G. Gillen, Microstructure - cooling rate correlations in melt-spun alloys, *J. Mater. Sci.* 26 (1991) 1266–1276. <https://doi.org/10.1007/BF00544465>.
- [53] R. Pond, R. Maddin, A Method of Producing Rapidly Solidified Filamentary Castings, *Trans. Metall. Soc. AIME.* 245 (1969) 2475–6.

- [54] H.S. Chen, C.E. Miller, A Rapid Quenching Technique for the Preparation of Thin Uniform Films of Amorphous Solids, *Rev. Sci. Instrum.* 41 (1970) 1237. <https://doi.org/10.1063/1.1684774>.
- [55] H.H. Liebermann, Rapidly solidified alloys made by chill block melt-spinning processes, *J. Cryst. Growth.* 70 (1984) 497–506. [https://doi.org/10.1016/0022-0248\(84\)90308-7](https://doi.org/10.1016/0022-0248(84)90308-7).
- [56] H.S. Chen, H.J. Leamy, C.E. Miller, Preparation of Glassy Metals, *Annu. Rev. Mater. Sci.* 10 (1980). <https://doi.org/10.-363-91>.
- [57] Y. Zhang, H. Wang, T. Zhai, T. Yang, Y. Qi, D. Zhao, Hydrogen storage characteristics of the nanocrystalline and amorphous MgeNdeNieCu-based alloys prepared by melt spinning, (2014). <https://doi.org/10.1016/j.ijhydene.2013.12.139>.
- [58] A.V. Shelyakov, N.N. Sitnikov, V.V. Koledov, D.S. Kuchin, A.I. Irzhak, N.Y. Tabachkova, Melt-spun thin ribbons of shape memory TiNiCu alloy for micromechanical applications, *Int. J. Smart Nano Mater.* 2 (2011) 68–77. <https://doi.org/10.1080/19475411.2011.567305>.
- [59] S. Wang, Y.M. Jiang, Y.F. Liang, F. Ye, J.P. Lin, Magnetic Properties and Core Loss Behavior of Fe-6.5wt.%Si Ribbons Prepared by Melt Spinning, *Adv. Mater. Sci. Eng.* 2015 (2015). <https://doi.org/10.1155/2015/410830>.
- [60] R.C. Budhani, T.C. Goel, K.L. Chopra, Melt-spinning technique for preparation of metallic glasses, *Bull. Mater. Sci.* 4 (1982) 549–561. <https://doi.org/10.1007/BF02824962>.
- [61] W. Löser, O. Shuleshova, Nucleation and Solidification Kinetics of Metastable Phases in Undercooled Melts, in: D.M. Herlach and D.M. Matson (Ed.), *Solidification of Containerless Undercooled Melts*, Wiley, Weinheim, Germany, 2012: pp. 187–212. <https://doi.org/10.1002/9783527647903.ch9>.
- [62] V.I. Tkatch, A.I. Limanovskii, S.N. Denisenko, S.G. Rassolov, The effect of the melt-spinning processing parameters on the rate of cooling, *Mater. Sci. Eng. A.*

323 (2002) 91–96. [https://doi.org/10.1016/S0921-5093\(01\)01346-6](https://doi.org/10.1016/S0921-5093(01)01346-6).

- [63] A. Lovas, E. Kisdi-Koszo, L. Potocky, L. Novak, Effect of processing conditions on physical properties of transition metal-metalloid metallic glasses, *J. Mater. Sci.* 22 (1987) 1535–1546.
- [64] V. Manov, P. Popel, E. Brook-Levinson, V. Molokanov, M. Calvo-Dahlborg, U. Dahlborg, V. Sidorov, L. Son, Y. Tarakanov, Influence of the treatment of melt on the properties of amorphous materials: Ribbons, bulks and glass coated microwires, *Mater. Sci. Eng. A.* 304–306 (2001) 54–60. [https://doi.org/10.1016/S0921-5093\(00\)01433-7](https://doi.org/10.1016/S0921-5093(00)01433-7).
- [65] R.C. Ruhl, Cooling rates in splat cooling, *Mater. Sci. Eng.* 1 (1967) 313–320. [https://doi.org/10.1016/0025-5416\(67\)90013-4](https://doi.org/10.1016/0025-5416(67)90013-4).
- [66] H. Fiedler, H. Mohlbach, G. Stephani, The effect of the main processing parameters on the geometry of amorphous metal ribbons during planar flow casting (PFC), *J. Mater. Sci.* 19 (1984) 3229–3235.
- [67] A.C. Ferrari, D.M. Basko, Raman spectroscopy as a versatile tool for studying the properties of graphene, *Nat. Nanotechnol.* 8 (2013) 235–246. <https://doi.org/10.1038/nnano.2013.46>.
- [68] A.C. Ferrari, Raman spectroscopy of graphene and graphite: Disorder, electron-phonon coupling, doping and nonadiabatic effects, *Solid State Commun.* 143 (2007) 47–57. <https://doi.org/10.1016/j.ssc.2007.03.052>.
- [69] M.S. Dresselhaus, A. Jorio, R. Saito, Characterizing Graphene, Graphite, and Carbon Nanotubes by Raman Spectroscopy, *Annu. Rev. Condens. Matter Phys.* 1 (2010) 89–108. <https://doi.org/10.1146/annurev-conmatphys-070909-103919>.
- [70] M.A. Pimenta, G. Dresselhaus, M.S. Dresselhaus, L.G. Cançado, A. Jorio, R. Saito, Studying disorder in graphite-based systems by Raman spectroscopy, *Phys. Chem. Chem. Phys.* 9 (2007) 1276–1290. <https://doi.org/10.1039/B613962K>.

- [71] A.C. Ferrari, J.C. Meyer, V. Scardaci, C. Casiraghi, M. Lazzeri, F. Mauri, S. Piscanec, D. Jiang, K.S. Novoselov, S. Roth, A.K. Geim, Raman spectrum of graphene and graphene layers, *Phys. Rev. Lett.* 97 (2006) 187401.
<https://doi.org/10.1103/PhysRevLett.97.187401>.
- [72] R. Trusovas, G. Račiukaitis, G. Niaura, J. Barkauskas, G. Valušis, R. Pauliukaite, Recent Advances in Laser Utilization in the Chemical Modification of Graphene Oxide and Its Applications, *Adv. Opt. Mater.* 4 (2016) 37–65.
<https://doi.org/10.1002/adom.201500469>.

2 Porous Graphite Fabricated by Liquid Metal Dealloying of SiC

2.1 Summary

Porous graphite was prepared by dealloying SiC in molten germanium and then excavating the Ge phase. The liquid metal dealloying (LMD) process was extended to non-metal precursors, demonstrating that carbide-derived carbons (CDCs) can be fabricated by this process. The dealloying depth, concentration profile, and length scale of the dealloyed microstructure were examined as they varied with immersion times and temperatures. The dealloying depth h varied with time as $h \sim t^{1/2}$ and we also observed a build-up of Si concentration in the germanium near the dealloying interface. These observations are consistent with kinetics that are rate-limiting in the liquid germanium side of the moving interface. However, the measured activation barrier of 2.4 – 2.8 eV was too high to be consistent with diffusion in the liquid phase, so instead we propose a mechanism in which Si diffusion is impeded by unsaturated carbon bonds near the dealloying. The porous graphite exhibited three-dimensional connectivity and a high degree of crystallinity, with an I(D)/I(G) ratio of 0.3 for samples dealloyed at the highest temperatures.

2.2 Introduction

Porous graphite is a versatile material with a wide range of applications. Depending on the details of its microstructure, its desirable properties include high specific surface area, good electrical conductivity, and relatively low cost. Such characteristics make it useful as molecular sieves [1], absorptive composites [2], filtration devices [3], and electrode materials in devices such as Li ion batteries [4,5] and capacitors [6]. Some traditional methods for synthesizing porous carbon materials involve high temperature catalytic or chemical activation and carbonization of a precursor [7–9]. While various methods of synthesizing porous carbon materials exist, producing interconnected material with tunable pore sizes, narrow feature size distribution, and a significant degree of graphitization has been a challenge. For these reasons, identifying new methods to transform carbon-containing materials into porous graphite is of significant scientific interest.

Porous graphite synthesis from carbides is a well-studied field and a review of the topic can be found in Chapter 1.3. Carbide-derived carbons (CDCs) employ a direct transformation of a carbide (SiC, VC, TiC, etc.) to carbon using a variety of processing conditions that lead to differing properties and morphologies of the resulting material, including nanotubes, diamond, carbon onions, and porous carbon with varying pore sizes [10–13].

Liquid metal dealloying is another, but less well-studied, technique previously used to fabricate nanoporous graphite. In its most general sense, dealloying is a processing technique wherein a homogenous non-porous alloy undergoes selective dissolution of one or more of its components under conditions where the remaining

component reorganizes itself into a three-dimensional bicontinuous porous structure. As detailed in Chapter 1.4, the length scale of the dealloyed microstructure is controlled dynamically, rather than being intrinsic to the parent alloy [14–17]. Furthermore, dealloying maintains the original grain structure of the parent materials because mass transport is primarily via interface diffusion; that is, there are no mechanisms by which to create defects such as grain boundaries. We shall see, however, that dealloying of SiC does not fall neatly into this category because mass re-organization of carbon is accompanied by simultaneous chemical changes.

The structure of the resulting carbon material produced via either LMD or CDC formation can be affected by the carbon fraction of the precursor. SiC and Ti_3SiC_2 produce CDCs with varying porosities due to differences in the carbon fraction [18]. A similar phenomenon is found for the LMD of metals. Geslin et al. reported a wide range of porous Ta morphologies fabricated by dealloying $\text{Ti}_x\text{Ta}_{1-x}$ with varying phase fractions of the non-dissolving component, from the prototypical bicontinuous morphology at high Ta mole fractions (35 at.%) to a lamellar structure at intermediate concentrations (15 at.%) [19]. Additionally, two distinct graphite morphologies were observed from the LMD of an $\text{Mn}_{85}\text{C}_{15}$ precursor that phase separated into Mn_{23}C_6 and $\alpha\text{-Mn}$, where the lower porosity material originated from the former phase [20]. We also suspect variations in the morphology of resultant carbon produced via LMD of metals and ceramics due to differences in crystal structure. Since covalent bonding is directional and the crystal structure of the ceramic is less densely packed than its metallic counterparts, we can expect differences in the connectedness and morphologies of the porous materials produced when one of the components is extracted.

In this work, we demonstrate for the first time the LMD technique on a ceramic precursor, further adding to the set of materials systems amenable to dealloying. Porous graphite was fabricated by immersion of SiC in molten Ge, where Si was selectively dissolved from the precursor. The system exhibits the thermodynamic requirements for dealloying; namely, carbon is insoluble in Ge while Si and Ge are miscible over their entire composition range both in the solid and liquid phases. However, compared to other dealloyed systems, SiC is unique being a covalently bonded stoichiometric precursor with a very high bond enthalpy and upon dealloying carbon transforms from an sp^3 bonded network with Si to a highly crystalline sp^2 bonded network without a further graphitization step; it is a kind of LMD with an additional chemical (structural) reaction at the metal/solid interface.

Here we report the preparation and characterization of dealloyed research-grade 4H-SiC single crystals. We also demonstrate that research grade 6H SiC and dummy grade 4H-SiC can also be successfully dealloyed. However, only research-grade 4H SiC was used to elucidate the kinetics of dealloying and this polymorph can be used as a prototype for the dealloying of other SiC crystal structures as well as other intermetallics (see Appendix A). We find that the SiC can be dealloyed in molten Ge to produce a carbon-Ge composite that retains the dimensions, though not the crystal orientation, of the parent material. We also find that the dealloying kinetics in this system exhibit most, but not all, of the characteristics of LMD in all-metal alloy systems. For instance, the dealloying depth h slows down as a function of time t as $h \sim t^{1/2}$, which is typical behavior in the LMD of metal containing alloys. Unlike conventional liquid metal dealloying, however, the crystal structure of the parent material is not preserved, and we transform

single crystal SiC to a polycrystalline graphitic network with a generally uniform length scale. Ge can be chemically etched from dealloyed SiC to expose the interconnected porous graphite film, and this material exhibits a characteristic pore size depending on the processing temperature.

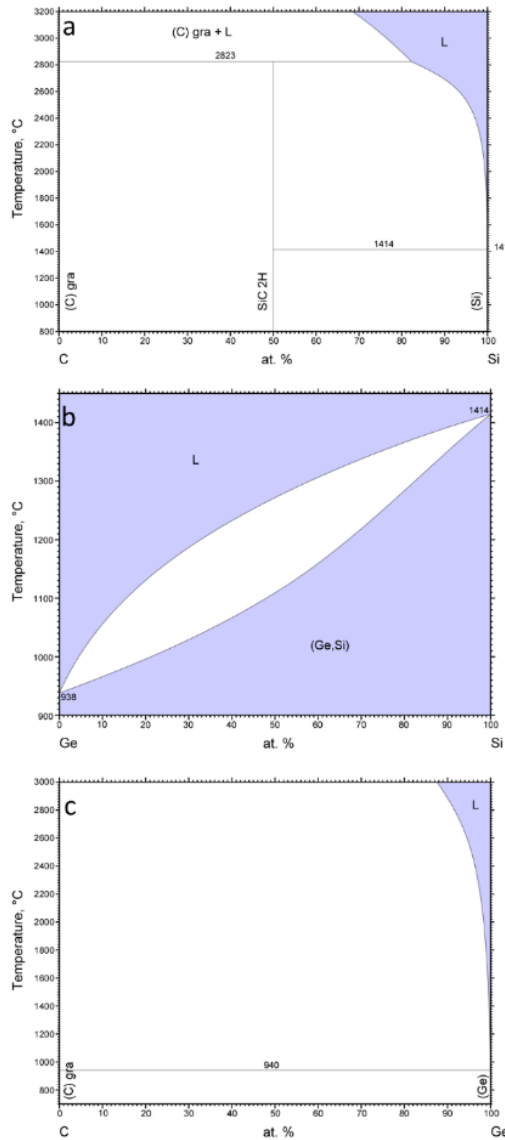


Figure 2-1. (a) Binary phase diagram of Si-C. (b) Binary phase diagram of Ge-Si showing miscibility over the entire composition range in solid and liquid phases. (c) Binary phase diagram of C-Ge effectively showing no solubility of C in Ge at temperatures below 1400 °C. © ASM International.

2.3 Experimental Methods

2.3.1 Liquid Metal Dealloying

The dealloying process is depicted in Figure 2-2(a). Experiments were performed by submerging bulk SiC wafer pieces into molten Ge. The dealloying process was tested on research grade (micropipe density $< 0.3 \text{ cm}^{-2}$) 4H and 6H SiC and dummy grade (micropipe density $< 25 \text{ cm}^{-2}$) 4H SiC. The grade is indicative of the micropipe density of the material; micropipes are screw dislocations that propagate through the thickness of the SiC. The polytypes differ by stacking order; the stacking sequences for 4H and 6H are ABCB and ABCAB, respectively. To elucidate the kinetics of dealloying in this system, only the research grade 4H SiC was used, and we examined the dealloying depth, concentration profile and characteristic size of the dealloyed microstructure as they varied with immersion times and temperatures.

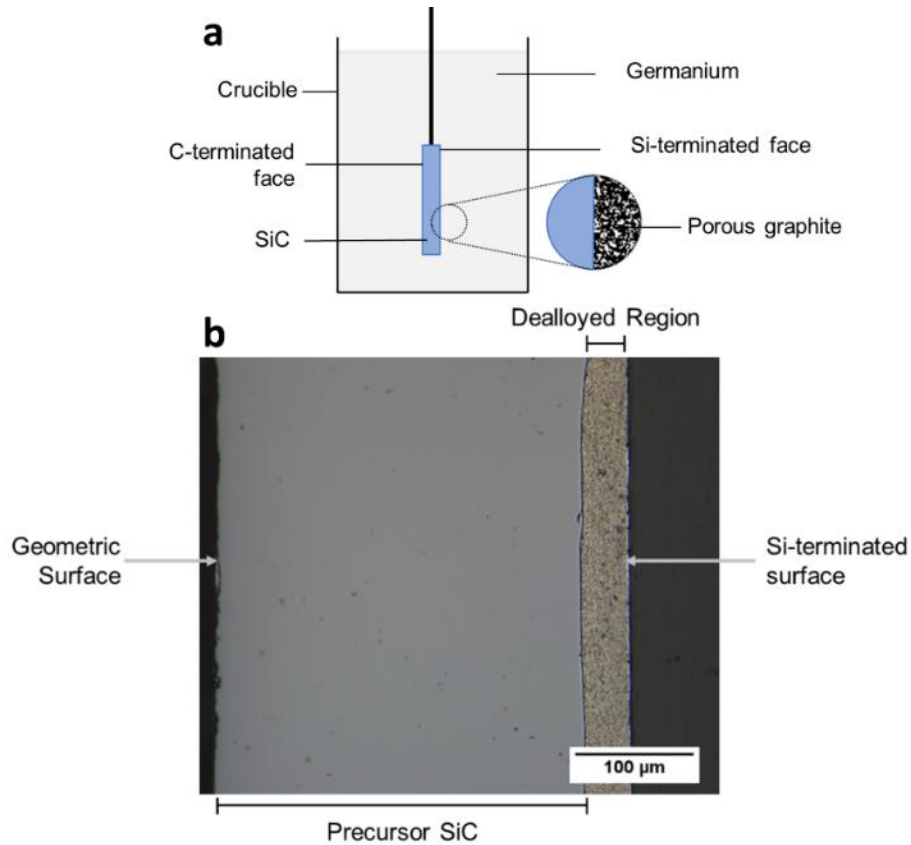


Figure 2-2. (a) Schematic diagram depicting dealloying process of single crystal SiC in molten Ge. Ge dissolves Si from the parent alloy, leaving behind a porous graphite network. (b) Optical micrograph showing SiC with a dealloyed region. Ge, the dissolving medium, solidifies in the carbon pores upon termination of the dealloying process. A fully dense network of carbon with Ge solidified in its pores is shown. Dealloying generally starts preferentially on the Si-terminated face surface while the C-terminated surface remains unchanged.

In a typical experiment, a 20 g mass of *n*-doped germanium (99.999 wt.% from Kurt J. Lesker) was inductively heated to fixed temperatures in a graphite crucible using a 4.5 kW Ambrell EkoHeat power supply. The chosen temperatures were 1200 °C (\pm 25°), 1300 °C (\pm 20 °C) and 1430 °C (\pm 15 °C) and temperature measurements were made using an Ircan Modline 5 infrared camera with a Yokogawa controller. All experiments were carried out under a flowing Ar atmosphere (99.999 at. %). In a typical experiment, a single piece of research grade, *n*-doped SiC wafer (MSE Supplies) approx. 30 mm x 10

mm x 0.35 mm was immersed into molten Ge for varied times at the preset temperatures using a vacuum manipulator arm. Upon conclusion of each experiment, the sample was lifted out of the bath to initiate cooling and discontinue the dealloying process.

Dealloying immersion times varied from 1 minute to 9 minutes, cooling of samples occurred on the order of one second, and we assume that dealloying terminated once the sample was pulled from the dealloying bath. The result was a fully dense structure that consisted of porous graphite impregnated with a solid germanium/silicon composite.

2.3.2 Characterization of As-Dealloyed SiC/Ge Samples

Once prepared, dealloyed samples were mounted on their shortest dimension and polished through their cross-sections. A typical sample is shown in Figure 2-2(b). We observed that SiC preferentially dealloyed on the Si-terminated face (see Discussion), and the present work only investigates the kinetics of dealloying on this surface. In approximately 10% of the samples, no dealloying was observed and in 25% of experiments, the dealloyed interfaces were neither sharp nor continuous. We believe this variation was likely due to surface contamination [21]. Most samples displayed a sharp and straight interface for a minimum length of 500 μm , and these samples were used for subsequent characterization. A minimum of 20 measurements from different regions of a sample were averaged to determine dealloying depth. Figure 2-3 depicts a typical cross-section and corresponding dealloying depth measurements, assessed by measuring the length from the geometric surface of a sample to the planar dealloyed interface using ImageJ. Average ligament diameters were determined using the AQUAMI software [22] on SEM micrographs. Compositional analysis as a function of depth was performed using energy dispersive spectroscopy (EDS).

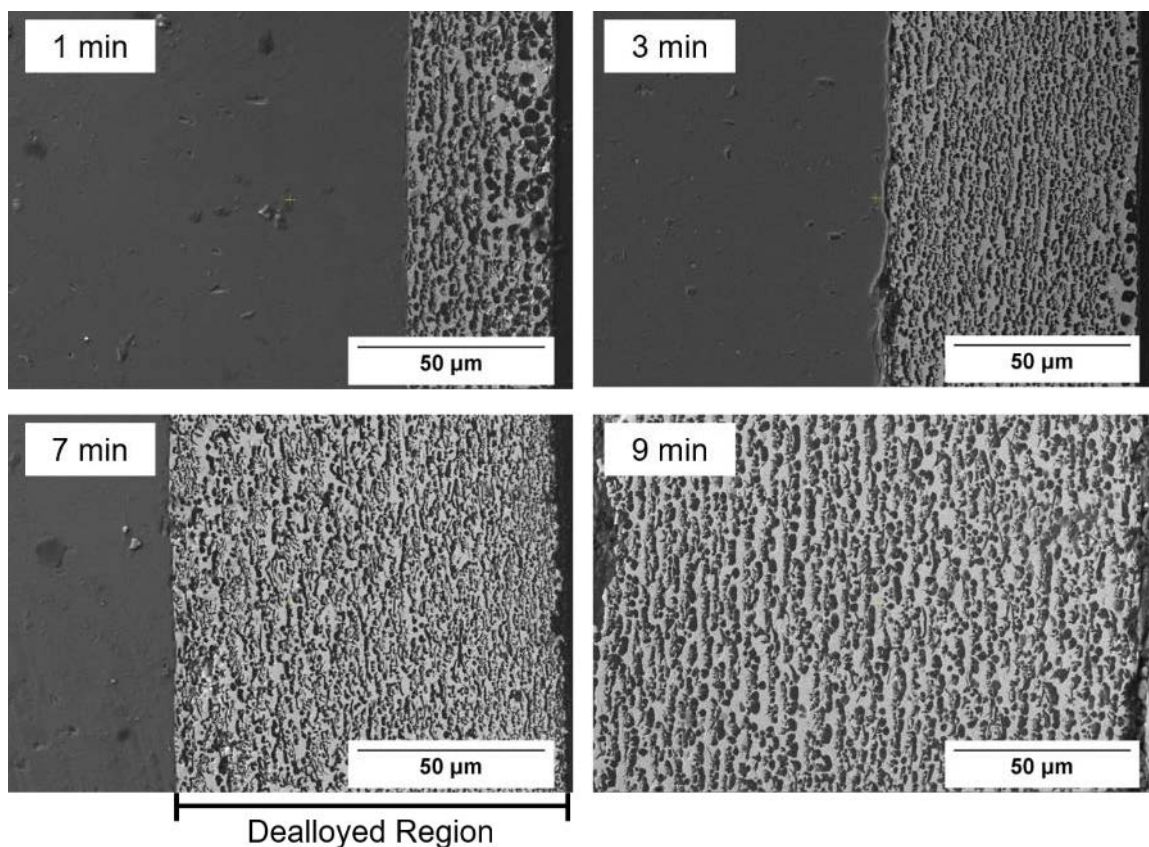


Figure 2-3. Scanning electron microscopy (SEM) micrographs of SiC samples dealloyed in molten germanium at 1300 °C for different times. The dealloying front proceeds right to left from the geometric surface towards the sharp and flat dealloying interface. The dealloying region displays different contrast as the light phase is Ge rich and the dark phase is carbon. The two images on the left were taken at 850x magnification and the images on the right were taken at 800x magnification, but it can be observed that the dealloying depth increases with time.

2.3.3 Excavation of the Pure Graphite Phase

The Ge rich phase was dissolved in hot aqua regia for ~45 minutes and rinsed thoroughly in distilled water to excavate the pure carbon phase in the dealloyed samples. The structure of the resulting porous graphite was then analyzed using a Horiba LabRam Evolution Raman microscope with a 532 nm laser. A Thermo Scientific Helios G4 UC Focused Ion Beam/ Scanning Electron Microscope (FIBSEM) instrument equipped with an energy dispersive spectroscopy (EDS) detector was used to image the material and

prepare carbon samples for imaging using the Thermo Scientific TF30 Transmission Electron Microscope (TEM).

Because bulk SiC wafers were used to obtain the kinetic parameters such as dealloying depth and ligament size, the form factor of the material we obtained after dealloying was a porous graphite film impregnated with solid Ge on the SiC surface. It was experimentally challenging to isolate a free-standing porous graphite membrane for further analysis. As a method to produce large quantities of material suitable for functional analysis (such as BET surface area), we propose employing the use of SiC powder in future experiments that would circumvent this experimental limitation.

2.4 Results and Discussion

2.4.1 General Observations

In conventional dealloying experiments, the surfaces of the material are chemically identical and therefore dealloy in an identical fashion under the same conditions. However, single crystal SiC is bipolar with a Si (0001) face and a C (000 $\bar{1}$) face and studies have reported markedly different chemical and physical properties of the two surfaces; for example, Kusunoki et al. found that after heating SiC at 1700°C in a vacuum, an aligned carbon nanotube film grew on the C face perpendicular to the surface while multiple graphene sheets formed on the Si face under the same conditions [23,24]. In our experiments, we observed that the dealloying process is initiated more readily on the Si surface. This observation held especially at the lower dealloying temperatures; at higher processing temperatures, we more frequently observed the evolution of a porous carbon structure initiated on the C-terminated surface. We hypothesize that the high solubility of Si in Ge allowed for more effective wetting of the Si surface by Ge

compared to the C terminated face, facilitating the initiation of the dealloying reaction at the Si surface at lower temperatures.

The dealloying interface (i.e., the boundary between the dealloyed and undealloyed material) was sharp, continuous and obvious, as is clear from Figure 2-4. Dealloying depth measurements from research grade 4H SiC were taken from dealloyed regions that had an interface length of 500 μm or longer where, in comparison, the ligament size of the porous carbon was on the order of tens of micrometers or less. Upon termination of the experiment, polished cross-sections show Ge solidified in the pores of the carbon and the carbon phase clearly appearing as dark precipitates dispersed throughout the lighter Ge background when examined via optical and scanning electron microscopy.

Figure 2-4 also shows that various types of SiC can be dealloyed successfully and the resultant dealloying depths exhibited only slight variations for different types of SiC processed under identical experimental conditions. This observation implies that research grade 4H SiC can be used as a prototype to determine the kinetics of dealloying SiC and other intermetallics. The microstructures of the dealloyed regions for both the 4H and 6H research grade materials were similar. However, the dealloyed microstructure of 4H dummy grade SiC exhibited three distinct regions of the evolved carbon particles; there was a stark gradation between the (i) fine feature sizes at the dealloyed interface and (ii) the adjacent area of larger carbon particles as well as (iii) another region of fine carbon particles near the geometric surface of the SiC. Therefore, micropipe density may influence the evolution of the dealloyed morphology, a phenomenon, however, that is out of the scope of this work.

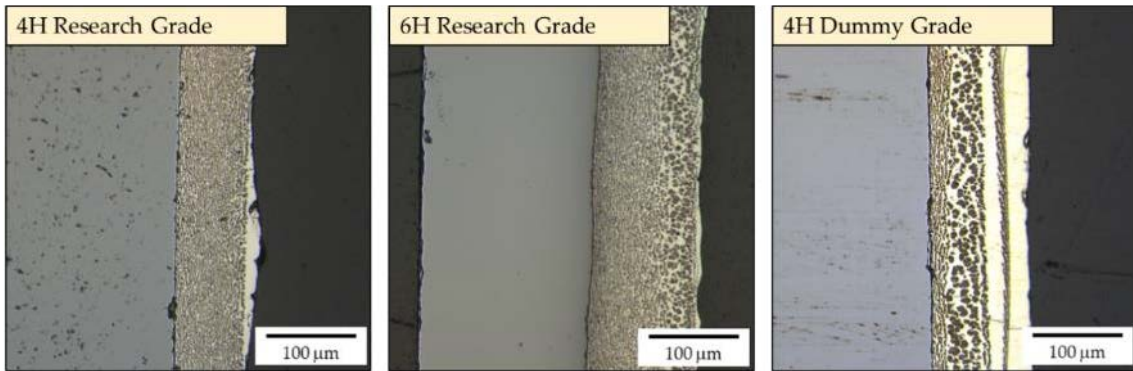


Figure 2-4. Optical micrographs of various types of SiC dealloyed under identical experimental conditions: (left) 4H research grade, (middle) 6H research grade and (right) 4H dummy grade.

2.4.2 Dealloying kinetics and morphological evolution in SiC-Ge.

In order to discuss our observations regarding the dealloying kinetics of SiC in Ge, it is useful first to review the kinetic response during LMD to that of electrochemical dealloying (ECD), the latter of which uses an electrolyte to induce selective dissolution, in order to compare the behavior of SiC dealloying to both.

LMD and ECD are both corrosion processes that result in a bicontinuous microstructure, and a detailed comparison/contrast between the two techniques has been reviewed by McCue et al. [25]. Notable points for comparison between the methods are the rate-limiting kinetics and the solubility of the remaining component in the bath. In the systems examined to date, LMD exhibits a dealloying depth increasing with time as $t^{1/2}$, with a corresponding decrease in the interface velocity as the dealloyed front penetrates into the sample. In the Ti/Ta system dealloyed in molten copper, these observations were quantitatively consistent with diffusion-limited transport of Ti through the molten copper in the pores formed behind the moving dealloying front. In contrast, the dealloying depth in ECD shows a constant velocity [26], which indicates that the dealloying kinetics are limited by the interface dissolution reaction. The diffusion rates

of the removed material in the liquid dissolution medium in both cases are similar, with diffusion coefficients of approximately 10^{-6} cm²/s, so the difference in kinetics is primarily manifested in the interface velocity. Consistent with rate limiting behavior, for LMD, the dealloyed front typically advances at a velocity of order 1 μ m/s, whereas in ECD, the interface velocity is of order 0.01 μ m/s. Diffusion limited transport in LMD leads to a significant concentration (> 10 at. %) of the dissolved species in the liquid medium near the dealloyed interface within the porous layer that decays toward the geometric surface of the sample.

The kinetic behavior of SiC exhibits characteristics of both LMD and ECD. Figure 2-5 (a) shows the dealloying depth h as a function of time t for single crystal SiC at three different temperatures: 1200 °C, 1300 °C and 1400 °C. The dealloying depth h vs. $t^{1/2}$ is plotted in Figure 2-5(b). Similar to observations of dealloying of metallic systems, dealloying depth h increases with temperature for fixed dealloying time t and appears to vary as a power law relationship with time consistent with diffusion-limited kinetics, i.e., $h \sim t^{1/2}$. We were unable to find a value in the literature for the diffusivity of Si in molten Ge, so we assumed that, because both Si and Ge are Group IV elements, they are chemically similar and exhibit comparable diffusion behavior [27]. We, therefore, estimate the diffusion coefficient of Si in liquid Ge to be on the order of 10^{-4} cm²/s based on the reported value for the self-diffusion coefficient of Ge in molten Ge as 1.8×10^{-4} cm²/s at 1246 °C [28]. We find experimentally that the interface velocity in this system is of order of 0.1 μ m/s. Compared to typical ECD and LMD systems, diffusion of Si in the germanium bath is approximately 2 orders of magnitude faster than in either ECD and LMD, while the interface velocities lie in-between typical values for the two processes.

Because diffusion is relatively fast compared to the interface velocity, we found it surprising that the interface velocity exhibited apparent diffusion limited kinetics (i.e., slowed down with dealloying depth).

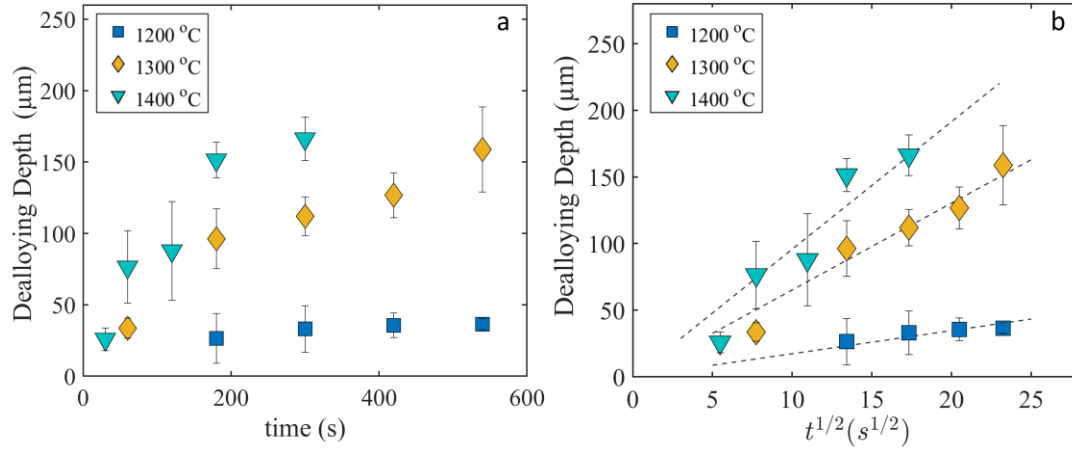


Figure 2-5. (a) Plot of dealloying depth h vs. time t measured at 1200 °C (blue, squares), 1300 °C (yellow, diamonds) and 1400 °C (green, triangles). (b) Plot of dealloying depth vs. $t^{1/2}$. Dealloying depth increased with increasing temperature and appeared to follow a power-law relationship with time. The error bars represent one standard deviation.

To examine the origin of rate-limiting behavior in more detail, we extracted the activation barrier associated with dealloying from our data collapse following the methodology outlined in Reference [29]. If there is an activated process controlling the dealloying kinetics, then dimensional analysis requires that any function such as the dealloying depth h must have the functional form $h(kt)$, where the Arrhenius rate constant is $k \sim \exp(-E_a/k_B T)$; k_B is Boltzmann's constant, T is the dealloying temperature and E_a is the activation barrier. To find E_a , we plotted $h(t)$ vs. scaled time $t = t \cdot \exp(-E_a/k_B T)$ and optimized for the best data collapse assuming that $h(t)$ follows a simple power law relationship $h(t) \sim t^n$; E_a and n (and a constant prefactor) were determined by the least squares method.

The exponent n is determined by the rate-controlling process and when the dealloying depth is rate-limited by diffusion and an interfacial reaction, the exponent n is reported to be 0.5 and 1.0, respectively [30,31]. Forcing $n = 0.5$ yields a reasonable fit to the data collapse, as shown in Figure 2-6, for which $E_a = 2.8$ eV. The best data collapse using this approach, however, is achieved when $n = 0.67$ which yields a smaller activation energy, $E_a = 2.4$ eV. It should be noted; however, the data collapse is relatively insensitive to this value. Tsuda et al. [30] reported an exponent greater than 0.6 for the liquid metal dealloying of Ti_2Cu and suggested that an interfacial reaction partly contributed to the rate-limiting process.

Additionally, a value of E_a between 2.4 – 2.8 eV is unreasonably large for a liquid phase diffusion process. For comparison, the activation energy for self-diffusion in molten Ge is only 0.16 eV [28]. Our measured value is closer to solid-state self-diffusion in Si-Ge, for which the activation barriers range from 2.9 – 3.5 eV depending on composition [36]. Lee et al. reported on the kinetics of carbide formation via the chlorination of SiC and observed a similar anomaly: the CDC growth layer followed a power law relationship with time where $n = 1/2$, but the calculated $E_a = 1.7$ eV was too high to be consistent with gas phase diffusion in the pores. Instead, an alternative mechanism of transport was suggested where chlorine diffused as an adsorbent on the pore surfaces [33].

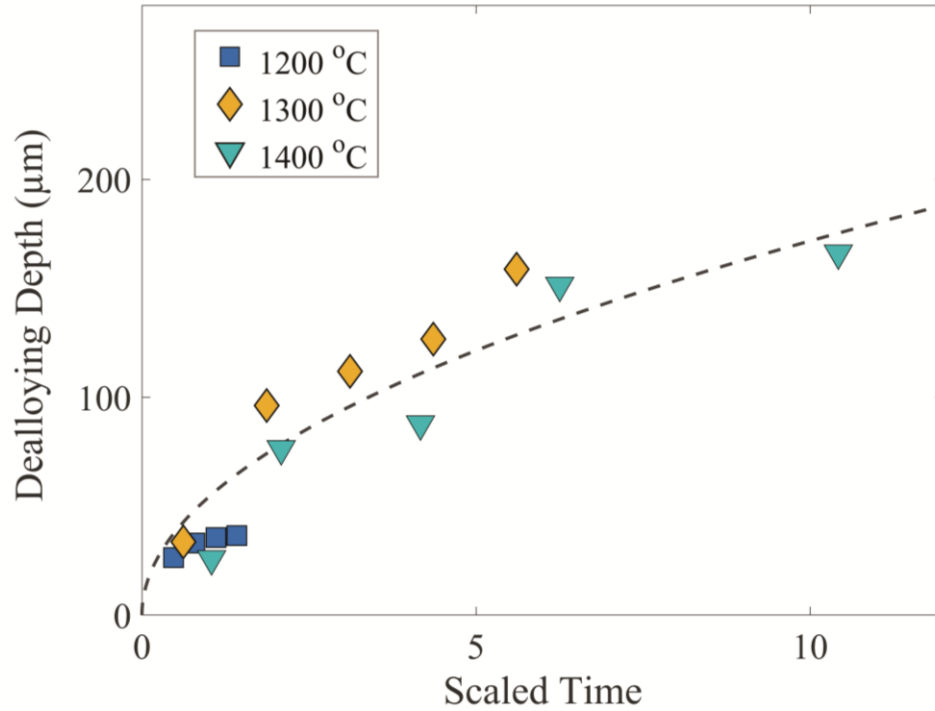


Figure 2-6. Collapsed dealloying depth versus scaled time $t' = t \cdot \exp(-E_a/k_B T)$ for SiC for measurements taken at 1200 °C (blue, squares), 1300 °C (yellow, diamonds), and 1400 °C (green, triangles). Dashed line: fits to the data using the relationship $h(t) \sim t^{1/2}$. The values for E_a and the scaling exponent were determined as the values associated with best least-squares fit.

We also examined the silicon concentration profile as it varied through the dealloyed region by direct measurement of the solidified Ge phase using EDS. As shown in Figure 1-7, we found that the Si concentration profile decays from the dealloying front, but the build-up of Si atoms only occurs in the first micrometer of a sample of a dealloyed region that extends to ca. 150 μm for a sample dealloyed for 9 minutes at 1300 °C. In contrast, in the LMD concentration profile obtained by McCue in the Ti-Ta system, the Ti concentration only reached a near-zero concentration close to the geometric surface of the dealloyed sample [29]. We were also unable to fit the concentration decay to McCue's model. For ECD, where the rate-limiting process is the interfacial reaction, the concentration of the leaving species in the liquid is expected to be

constant, so too is the dealloying velocity [26,29]. The observation that Si atoms accumulate only at the interface and then diffuse rapidly about 1 μm away from the interface deviates from expected behavior for both interfacial and diffusion rate-limited processes.

Figure 2-7 also shows the concentration profile for a sample dealloyed at 5 minutes; the Si concentration profile mimics that of the sample processed at a longer time. This behavior is consistent with steady-state diffusion where $\frac{dc}{dt} = 0$. Since we suspect an interfacial reaction is contributing to the rate-limiting behavior in the LMD of SiC, we make the reasonable assumption of steady state conditions, where the concentration of Si in the liquid at the interface and in the Ge bath is constant, ~ 0.5 at. % and 0 at. %, respectively, because the concentration of Si atoms supplied to the interface is constant and the concentration profile shown in Figure 2-7 indicates that virtually no Si is present outside of the interfacial region.

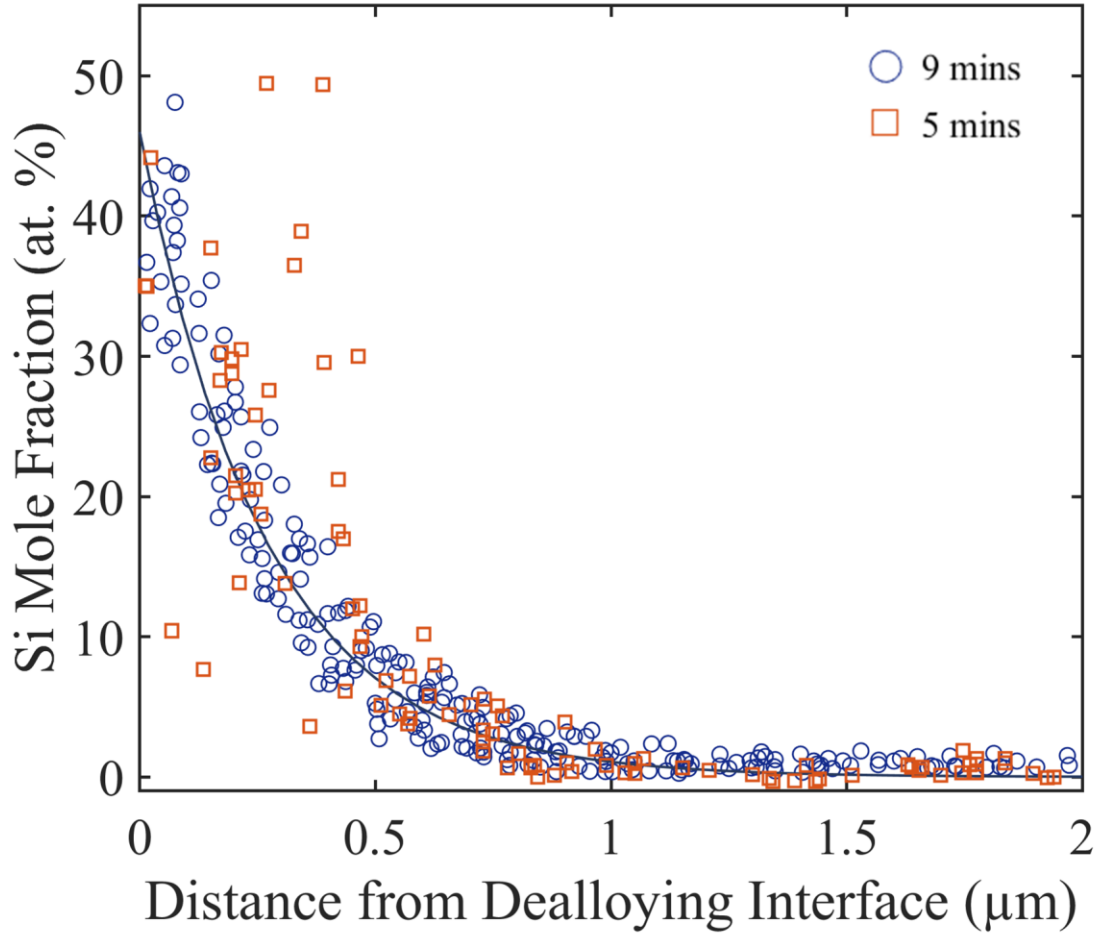


Figure 2-7. Si mole fraction versus distance away from the dealloying interface for SiC dealloyed in molten Ge at 1300 °C for 5 minutes (orange, squares) and 9 minutes (blue, circles). The dealloying interface is $x = 0$ and distance from the dealloying interface represents the liquid side of the interface. Unlike in conventional LMD, where there is a gradual decline of the dissolving component across the dealloyed region, the Si concentration declines rapidly to near 0 at. % within the first micrometer of the dealloyed region for both dealloying time periods shown. Solid line: data fits steady state diffusion equation as $C(x) = C_a \exp\left(-\frac{v_i}{D_L} x'\right)$.

Consider a system where there is limited diffusion right at the moving interface, and the solute profile ahead of this interface has reached a steady state. Using these boundary conditions, it follows that the diffusion equation is

$$\frac{dC}{dt} = D_L \frac{d^2C}{dx^2} \quad (1)$$

Where D_L is the diffusivity of Si in the liquid. Also,

$$\frac{dc}{dt} = \frac{dc}{dx} \frac{dx}{dt} = v_i \left(\frac{dc}{dx} \right) \quad (2)$$

For a steady state approximation,

$$v_i \left(\frac{dc}{dx} \right) + D_L \frac{d^2c}{dx^2} = 0 \quad (3)$$

which, when evaluated at the boundary conditions described above, gives

$$C(x) = C_a \exp\left(-\frac{v_i}{D_L} x'\right) \quad (4)$$

Where C_a is a prefactor and x' is the distance ahead of the moving interface. The slopes of the dealloying depth vs. time plots shown in Figure 2-5(a) can be used to determine the interface velocity v_i if it is assumed to vary linearly with time. For samples dealloyed at 1300 °C, v_i is 0.3 $\mu\text{m/s}$. Using the least squares method C_a and D_L were determined to be 0.46 at. % and $1 \times 10^{-9} \text{ cm}^2/\text{s}$, and the fit using these values is shown by the solid line in Figure 2-7. The value for C_a is consistent with the concentration of Si in the parent alloy which indicates that most of the Si atoms at the interface are dissolved. However, the value for the diffusivity of Si in the liquid at the interface is five orders of magnitude lower than expected for Si diffusion in molten Ge.

The observations of (i) slow diffusivity of Si in the liquid relative to the interface velocity, (ii) fast diffusion of Si into the liquid outside of the 1 μm transition zone ahead of the interface, (iii) a high activation barrier associated with rate-controlling behavior and (iv) a slowdown of the interface velocity with time, taken together, suggest that the mechanism of dealloying is complex. One possibility is a facile dissolution of a Si-C complex from the parent alloy that acts as a vehicle transporting C atoms to growing graphite clusters. This coupled species dissociates over approximately the first micron of

the liquid, freeing Si to diffuse into the molten Ge quickly. A second possibility is that as carbon reorganizes from the sp^3 configuration in SiC to sp^2 hybridized graphite, there is a transition zone in which a high number of C-dangling bonds act as transient points of attachment for Si, significantly slowing down diffusion within this zone. Such novel chemical-limiting steps in dealloying kinetics may be unique to systems such as SiC, where the hybridization of carbon changes during dealloying.

We briefly compare the kinetic response of carbon fabricated by LMD and halogenation, a conventional CDC preparation method. In 2001, Ersoy and colleagues reported a linear growth rate for porous carbon films produced via halogenation of sintered SiC at 1000 °C [34]. Similarly to ECD, this relationship indicates an interface-limited reaction, where in the case of the CDC, the controlling factor of the reaction was not diffusion of the reactant species through the growing carbon film. The composition of the mixture affected the linear rate constant, but as an example, the linear rate constant for a chlorine-hydrogen environment was 0.03 $\mu\text{m}/\text{min}$. However, Lee et al. demonstrated faster kinetics and a diffusion-limited process for CDC growth in the same temperature range as Ersoy's study but attributed the conflict to differences in experimental setup and procedures [33]. Regardless, the reaction kinetics described in both the interface and diffusion limited CDC growth processes are significantly slower than in LMD. According to Lee's study, growth of a 250 μm graphite film would take almost 20 hours at 1000 °C (interface velocity of 0.2 $\mu\text{m}/\text{min}$). In the LMD process described in this work, the processing time to grow a porous graphite layer of equal thickness is only 3 minutes at 1200 °C (interface velocity of 88 $\mu\text{m}/\text{min}$).

2.4.3 Ligament morphology and size

Figure 2-8(a) shows representative SEM micrographs of polished, cross-sectioned samples dealloyed at different temperatures. In each micrograph, the dark phase is carbon, and the light phase is solidified germanium. For samples dealloyed at 1200 °C, the carbon phase presents as randomly oriented elongated spines with a high degree of interconnectedness. For samples dealloyed at 1300 °C, the carbon appears as circular particles aligned normal to the dealloying direction with much less interconnectivity. At the highest temperature examined, the anisotropy is reduced, and the morphology consists primarily of disconnected circular structures interspersed in the Ge matrix. Even when the Ge phase was dissolved, the porous carbon appears as randomly oriented individual flakes and clusters of flakes on the surface (see Figure 2-9) as opposed to a porous network. It is interesting to note that although the material does not appear to contain a high degree of interconnectivity in the SEM micrographs, the porous graphite was mechanically robust, surviving the vigorous etching and rinsing process while still retaining the dimensions of the parent dealloyed zone. The TEM images (Figure 2-10) of porous graphite processed at the highest temperature, 1400°C, explain the inconsistency. The material consists of a network of ligaments that extend three-dimensionally; the ligaments are comprised of a series of overlapping graphite crystals that act as nodes from which elongated crystals branch. These ~1 μm long spokes connect various hubs; the result is a robust network that extends throughout the bulk of the material to form a topologically connected porous structure that we were unable to visualize with SEM.

We used the Aquami software on images of the porous graphite-germanium composite produced after dealloying (see Figure 2-8(a)) to quantify the ligament sizes

and an explanation of the detailed methods used in the digital image analysis can be found in Reference [22]. The ligament morphology of dealloyed SiC differs from those produced in conventional dealloying, but in a general sense, the relationship between ligament length scale and temperature is maintained, as shown in Figure 2-8(b). Specifically, the ligament length scale grows with increasing temperature. Looked at in detail, however, there is an interesting discrepancy associated with the remaining component being carbon. Sieradzki, McCue, et al. determined that ligament diameter scales with “inverse homologous temperature,” $T_m/T_{dealloy}$, for both LMD and ECD [25,35]. A plot showing this relationship is depicted in Figure 2-8(c), where data from the present work is also shown for comparison. Since graphite does not melt at atmospheric pressure, its sublimation point, 3642 °C, was used to calculate the inverse homologous temperature. While we do observe an increase in ligament length scaled with inverse homologous dealloying temperature, our work does not fall on the expected universal trend for LMD and ECD. We attribute this discrepancy to two factors: (i) the substitution of melting point with sublimation point and (ii) time-dependent coarsening.

Using images from Reference [20], we calculated ligament diameters of the porous graphite produced by LMD of a Mn-C precursor at 800 °C to be approximately 0.2 μm. In comparison, our samples processed at the lowest temperature (1200 °C) developed ligament diameters less than 0.5 μm. We posit that by reducing the processing temperature even further, we can evolve a material with even higher porosity. We mentioned earlier in the manuscript that we observed limited wetting of the SiC by the liquid metal at temperatures lower than 1200 °C, but the literature suggests that we can alter the composition of the Ge bath to improve the surface attraction between the

materials [36], allowing us to probe even lower temperature ranges in the future.

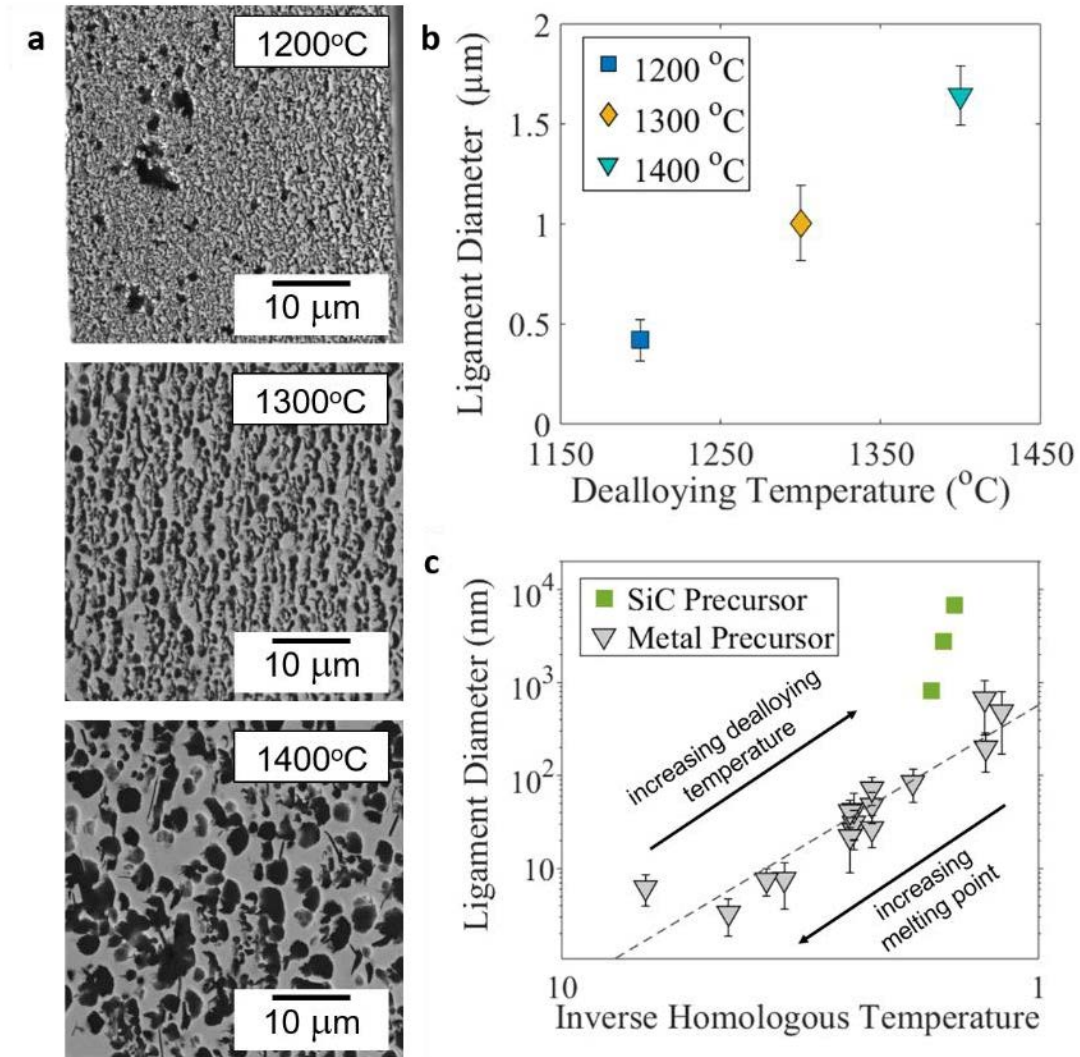


Figure 2-8. (a) SEM micrographs depicting ligament size increase with increasing temperature. Variation in ligament morphology is also observed with a higher degree of interconnectedness at the lowest experimental temperature, coalesced graphite particles aligned perpendicular to the dealloying direction at 1300 °C, and larger circular particles at the highest temperature. (b) Ligament diameter versus processing temperature for dealloying SiC. Length scales increase at higher temperatures. (c) Trend in ligament diameter versus inverse homologous temperature ($T_m/T_{dealloy}$) for electrochemical dealloying and liquid metal dealloying at different times, shown as grey triangles for metal systems (adapted with permission from reference [25]). Error bars represent one standard deviation. For comparison, the trend between ligament diameter and inverse homologous temperature for SiC ($T_{sublimation}/T_{dealloy}$) is shown as green squares. Error bars lie within the data markers.

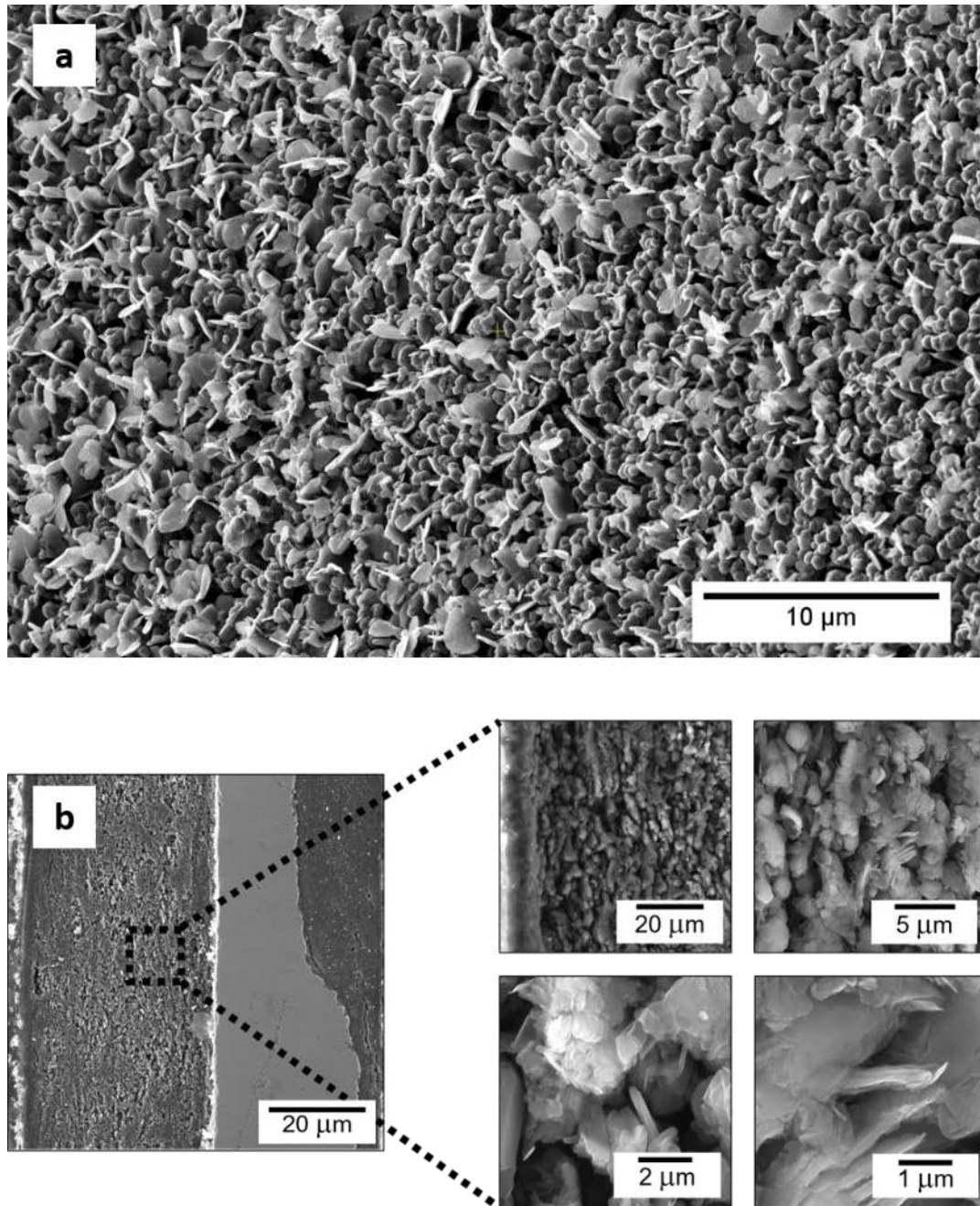


Figure 2-9. (a) SEM micrograph of porous graphite produced by dealloying at 1400 °C. (b) SEM micrograph of a cross-section of SiC dealloyed at 1300 °C. The morphology of the porous graphite is shown at increasing magnifications. The material presents as clusters of graphite flakes on the surface.

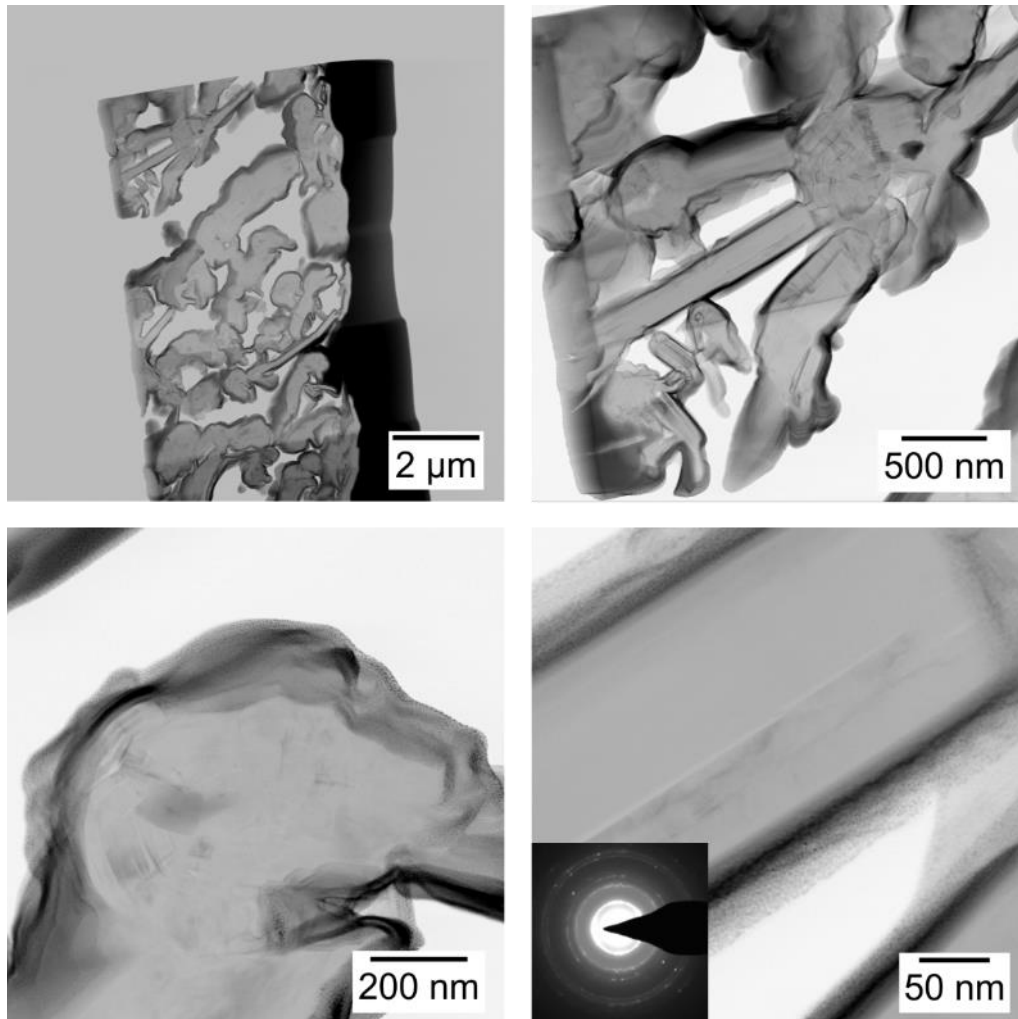


Figure 2-10. TEM images of a SiC sample dealloyed in molten Ge at 1400°C after etching in aqua regia to remove solidified Ge from pores. Images depict highly interconnected porous graphite. (Inset) selected area electron diffraction shows that the graphite is polycrystalline.

Due to decreased surface mobility, materials with higher melting points produce smaller ligaments after dealloying. Once dealloyed, the material behind the dissolution front often coarsens, and this is the reason larger ligament sizes are seen at higher temperatures. As already discussed in Chapter 1.4.2, coarsening is driven by two surface-diffusion mediated processes with a $t^{1/4}$ dependence: capillary effects and genus-reduction events. The driving force in the former is a reduction of surface area where there is mass transport from regions of high to regions of low curvature. The latter is driven by

Rayleigh instabilities where ligaments pinch off to reduce the genus or number of handles on a ligament [37]. In metal systems, experiments show a significant gradient of coarsening within a single sample; the ligament size varies by almost three orders of magnitude across the dealloyed depth. Gaskey et al. developed a model to describe the observed phenomenon [38]. They explain that coarsening in nanoporous metals is dominated by an attachment-mediated Ostwald ripening process that is facilitated by the solubility of the remaining component into the melt. In contrast, the feature sizes in our experiments are – for the most part – uniform across the dealloyed region at lower dealloying temperatures, indicating essentially zero carbon interface mobility (and consistent with the consolidation of the carbon network near the dealloying front). However, at 1300 °C, we sometimes observed regions with an abrupt size increase and a transition from a filamentous to a large-scale morphology near the surface of the sample (Figure 2-11), which we are unable to explain at this juncture.

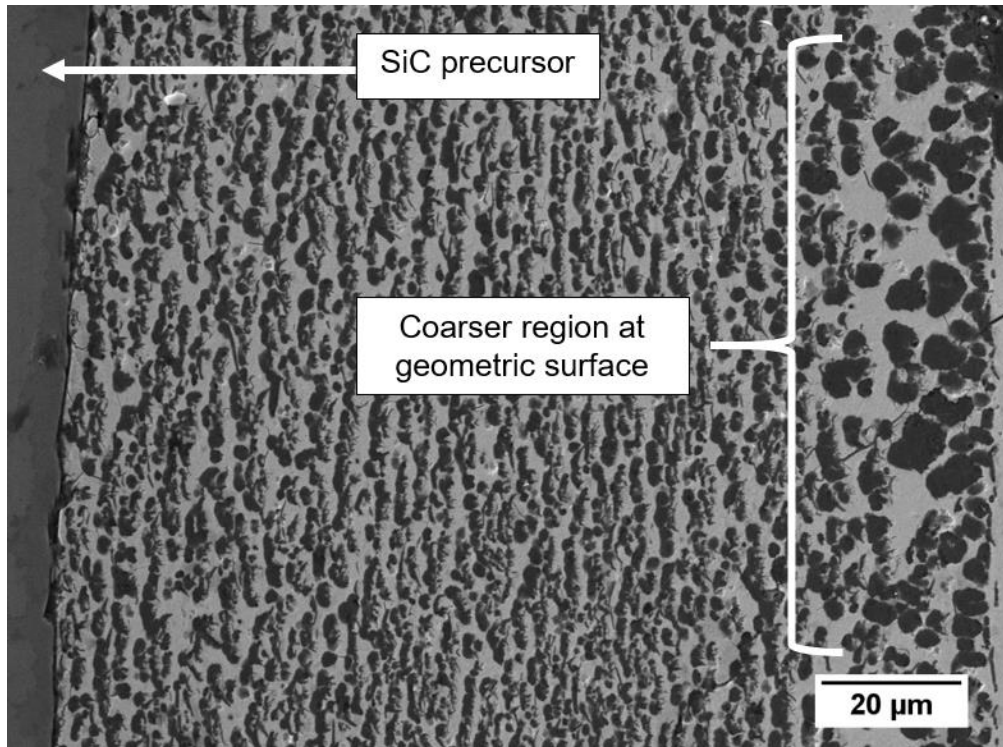


Figure 2-11. SEM micrograph showing anomalous carbon structures with larger feature sizes near the geometric surface of the sample during LMD at 1300°C. There is a 25 μm region on the surface where the carbon ligaments appear $> 5\mu\text{m}$ in diameter, but the rest of the sample shows uniform particle size up to the dealloyed interface.

2.4.4 Raman spectroscopy of porous graphite

The Ge rich phase of dealloyed SiC was chemically etched in hot aqua regia, and the presence of porous carbon was confirmed via EDS analysis, selected area electron diffraction, and Raman spectroscopy. The Raman fingerprint of graphite-related material exhibit three prominent peaks: the G band ($\sim 1580\text{ cm}^{-1}$), D ($\sim 1350\text{ cm}^{-1}$), and the 2D band ($\sim 2700\text{ cm}^{-1}$). The G peak is activated by sp^2 carbon networks and is therefore always present in the Raman fingerprint of any graphitic material, along with the 2D band which corresponds to a high energy second order-process and is always observed in the fingerprint. The D band and the D' band (1620 cm^{-1}) are defect activated peaks and are weak in the Raman spectra of graphite with low defect concentrations [39–41]. The

ratio of intensity between the D and G peaks, the $I(D)/I(G)$ ratio, can provide information about the crystal size and the defect density in the material where this ratio is inversely proportional to the crystal size, L_A [39]. The shape of the 2D band and the $I(2D)/I(G)$ ratio can be used to identify the number of graphene layers [42]. Figure 2-12 demonstrates a typical Raman spectrum of the material prepared at 1400 °C. The Raman features shown in the present work are similar to those reported for nanocrystalline graphite [41], that is, graphite that consists of small, randomly oriented crystallites in which the many grain boundaries and edges strongly activate the defect peaks. To evaluate the effect of the Ge removal on the graphite pores, Raman analysis was performed on the material before and after Ge etching, which is also depicted in Figure 2-12. We observed G band broadening by 6 cm^{-1} and a stiffening of peaks after Ge removal, where the G peak shifted by 5 cm^{-1} . Such small changes in the peaks are consistent with strain and doping by metals, which are known to influence the Raman spectrum of graphene and graphite [43–45]. However, the $I(D)/I(G)$ and $I(2D)/I(G)$ ratios remain relatively unchanged, indicating that no significant change in the graphite structure occurred during the corrosion of Ge in aqua regia.

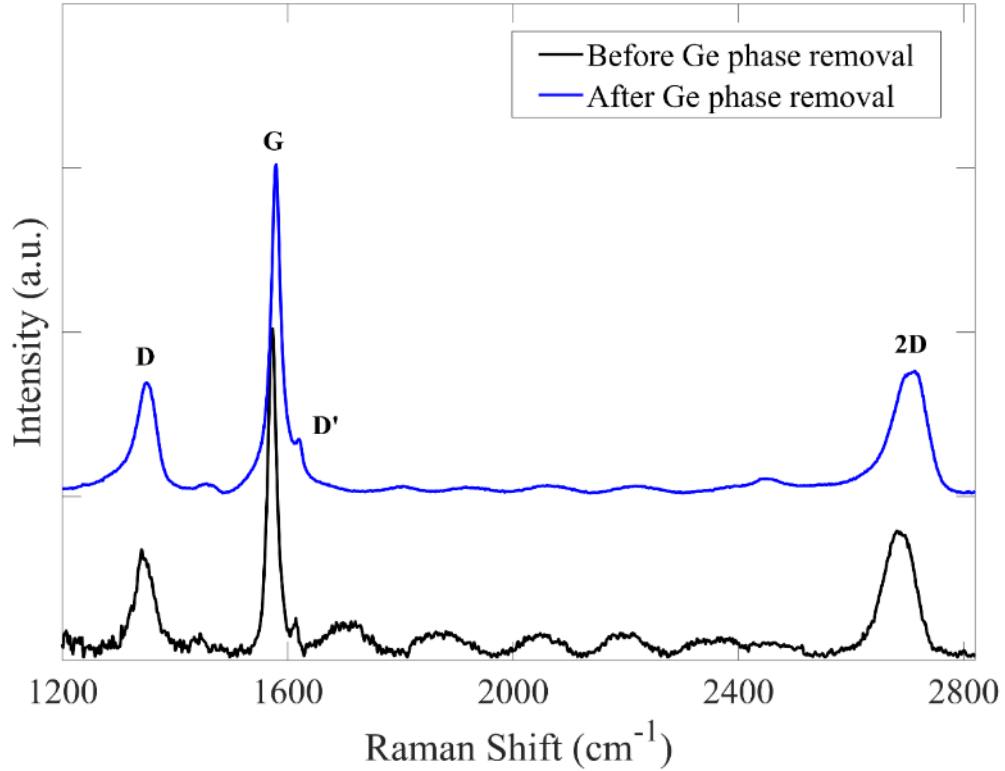


Figure 2-12. Raman spectra of the porous graphite before and after the Ge phase was etched from the pores. The Raman fingerprint exhibits characteristics features of nanographite. The very low intensity peaks between 1700 cm^{-1} and 2600 cm^{-1} were activated by the epoxy sample mount.

We also analyzed the Raman spectra of graphite produced by dealloying at different processing temperatures, and the results are shown in Figure 2-13 and summarized in Table 2-1. The full width at half maximum (FWHM) of the G peak broadens due to disorder [46], and we observe a nominal decrease in the FWHM-G for graphite fabricated by dealloying at cooler temperatures. The crystallite size, L_A , was computed using the general equation [41,47]:

$$L_A(\text{nm}) = 2.4 \times 10^{-10} \lambda_{\text{laser}}^4 \left(\frac{I(D)}{I(G)} \right)^{-1}$$

As expected, we observed an inverse relationship between processing temperature and I(D)/I(G) ratio, an indicator for crystallinity [18]. This trend suggests that we can tune the degree of disorder and crystallite size by varying the temperature.

We compare the Raman features of porous graphite produced in this work to that of carbon black (Cabot Corporation). Despite its low surface area, carbon black's moderate conductivity, low cost, and large pore volume make it an attractive material for electrocatalyst support in fuel cells and as a component of the cathode in lithium ion batteries [48]. However, scientists have been looking for carbon black substitutes that exhibit superior conductivity, crystallinity, and durability. Since Yu reported decreased volume resistivity in the porous graphite material post-graphitization at high temperatures, we note the implied relationship that a lower I(D)/I(G) ratio (higher crystallinity) indicates increased conductivity [20]. In this work, porous graphite synthesized from the LMD of SiC at 1200 °C had an I(D)/I(G) ratio of 0.41. In comparison, the measured I(D)/I(G) ratio of carbon black was 0.78, whereas the 3D porous graphite produced via LMD in Yu's work from a Mn-C precursor exhibited an I(D)/I(G) ratio of 0.46 only after a secondary high temperature graphitization step that involved heating the material at 1500 °C for 2 hours [20]. CDCs fabricated by halogenation are predominantly amorphous even in material prepared at temperatures over 1000 °C; for example, Ersoy reported I(D)/I(G) ratios of ~1 for CDCs fabricated by chlorination [13,34,49,50]. The as-prepared porous graphite fabricated in this study exhibited a high degree of crystallization compared to material prepared by other methods, which augurs well for its use in electrical devices.

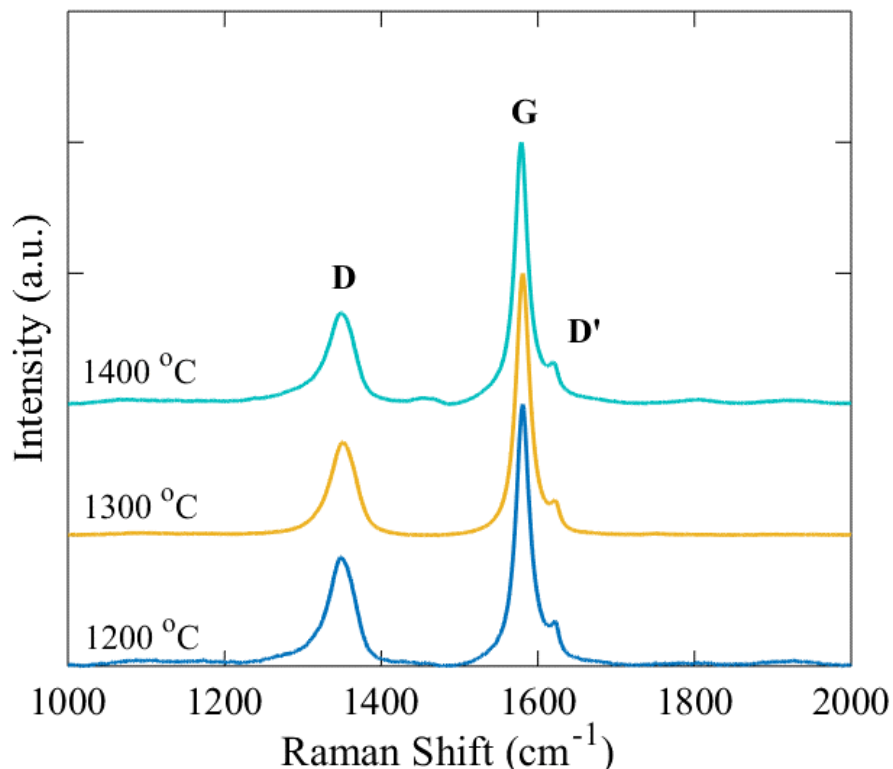


Figure 2-13. Raman spectra of porous graphite processed at different dealloying temperatures.

Table 2-1. Summary of properties of porous graphite processed under different conditions.

| | 1200 °C | 1300 °C | 1400 °C | 1400 °C Ge in Pores | Carbon Black |
|-----------------------------|---------|---------|---------|------------------------|-----------------|
| I(D)/I(G) | 0.41 | 0.36 | 0.34 | 0.33 | 0.78 |
| L_A (nm) | 46.7 | 53.9 | 57.4 | 58.9 | 24.6 |
| FWHM-G (cm^{-1}) | 21.3 | 21.0 | 20.2 | 26.2 | 51.8 |
| G Peak (cm^{-1}) | 1580.6 | 1580.7 | 1578.8 | 1574.1 | 1585.2 |

2.5 Conclusion

We report the fabrication of a porous network of graphite via the liquid metal dealloying (LMD) of a covalently bonded ceramic precursor, SiC, in molten germanium. This work focuses on the fundamental kinetics of a promising technique whereby mechanically robust and highly crystalline porous graphite can be produced. Preparing porous graphite via the LMD of SiC provides an alternative and facile route of preparing

a CDC with uniform morphology, tunable ligament sizes with narrow size distributions, fast kinetics, and low defect density indicated by I(D)/I(G) ratios as low as 0.3.

Furthermore, no additional annealing step is required to remove residual halogen adsorbents. With respect to dealloying generally, our process expands the set of systems suitable candidates for liquid metal dealloying. When compared to previous work on the fabrication of porous graphite via LMD, our as-prepared material exhibited greater uniformity and superior crystallinity, despite having larger pore sizes which we attribute to the higher processing temperatures.

The kinetics of LMD of the non-metal containing SiC precursor was examined by varying the dealloying time and temperature, and the kinetics were compared to that of conventional dealloying and CDC processing. It was found that the interface velocity in the present work is much faster than in CDC formation via chlorination but slower than in conventional LMD. The concentration gradient of Si decayed away from the dealloying interface with slow diffusivity, but outside of a transition zone, the Si diffusivity in the liquid was rapid. The dealloying depth h appeared to vary with time as $h \sim t^{1/2}$, associated with rate-limiting diffusion away from the interface. However, the measured activation barrier of 2.4 – 2.8 eV is too high to be consistent with diffusion in the Ge melt, so instead, we propose a complex mechanism in which Si diffusion is impeded by unsaturated carbon atoms near the dealloying front.

2.6 References

- [1] H.C. Foley, Carbogenic molecular sieves: synthesis, properties and applications, *Microporous Mater.* 4 (1995) 407–433. [https://doi.org/10.1016/0927-6513\(95\)00014-Z](https://doi.org/10.1016/0927-6513(95)00014-Z).
- [2] Q. Liu, D. Zhang, T. Fan, Electromagnetic wave absorption properties of porous carbon/Co nanocomposites, *Appl. Phys. Lett.* 93 (2008). <https://doi.org/10.1063/1.2957035>.
- [3] D. Siemer, J.F. Lech, R. Woodriff, Direct filtration through porous graphite for A.A. analysis of beryllium particulates in air, *Spectrochim. Acta Part B At. Spectrosc.* 28 (1973) 469–471. [https://doi.org/10.1016/0584-8547\(73\)80052-7](https://doi.org/10.1016/0584-8547(73)80052-7).
- [4] T. Deng, X. Zhou, The preparation of porous graphite and its application in lithium ion batteries as anode material, *J. Solid State Electrochem.* 20 (2016) 2613–2618. <https://doi.org/10.1007/s10008-016-3260-1>.
- [5] Y.-S. Hu, P. Adelhelm, B.M. Smarsly, S. Hore, M. Antonietti, J. Maier, Synthesis of Hierarchically Porous Carbon Monoliths with Highly Ordered Microstructure and Their Application in Rechargeable Lithium Batteries with High-Rate Capability, *Adv. Funct. Mater.* 17 (2007) 1873–1878. <https://doi.org/10.1002/adfm.200601152>.
- [6] Y. Korenblit, M. Rose, E. Kockrick, L. Borchardt, A. Kvit, S. Kaskel, G. Yushin, High-Rate Electrochemical Capacitors Based on Ordered Mesoporous Silicon Carbide-Derived Carbon, *ACS Nano.* 4 (2010) 1337–1344. <https://doi.org/10.1021/nn901825y>.
- [7] M.C.A. Ferraz, Preparation of activated carbon for air pollution control, *Fuel.* 67 (1988) 1237–1241. [https://doi.org/10.1016/0016-2361\(88\)90045-2](https://doi.org/10.1016/0016-2361(88)90045-2).
- [8] T. Tay, S. Ucar, S. Karagöz, Preparation and characterization of activated carbon from waste biomass, *J. Hazard. Mater.* 165 (2009) 481–485.

<https://doi.org/10.1016/J.JHAZMAT.2008.10.011>.

- [9] B.S. Girgis, S.S. Yunis, A.M. Soliman, Characteristics of activated carbon from peanut hulls in relation to conditions of preparation, *Mater. Lett.* 57 (2002) 164–172. [https://doi.org/10.1016/S0167-577X\(02\)00724-3](https://doi.org/10.1016/S0167-577X(02)00724-3).
- [10] Y. Gogotsi, A. Nikitin, H. Ye, W. Zhou, J.E. Fischer, B. Yi, H.C. Foley, M.W. Barsoum, Nanoporous carbide-derived carbon with tunable pore size, *Nat. Mater.* 2 (2003) 591–594. <https://doi.org/10.1038/nmat957>.
- [11] G. Yushin, E.N. Hoffman, M.W. Barsoum, Y. Gogotsi, C.A. Howell, S.R. Sandeman, G.J. Phillips, A.W. Lloyd, S. V. Mikhalovsky, Mesoporous carbide-derived carbon with porosity tuned for efficient adsorption of cytokines, *Biomaterials.* 27 (2006) 5755–5762. <https://doi.org/10.1016/J.BIOMATERIALS.2006.07.019>.
- [12] Y.G. Gogotsi, M. Yoshimura, Formation of carbon films on carbides under hydrothermal conditions, *Nature.* 367 (1994) 628–630. <https://doi.org/10.1038/367628a0>.
- [13] S. Welz, M.J. McNallan, Y. Gogotsi, Carbon structures in silicon carbide derived carbon, *J. Mater. Process. Technol.* 179 (2006) 11–22. <https://doi.org/10.1016/J.JMATPROTEC.2006.03.103>.
- [14] J. Rugolo, J. Erlebacher, K. Sieradzki, Length scales in alloy dissolution and measurement of absolute interfacial free energy, *Nat. Mater.* 5 (2006) 946–949. <https://doi.org/10.1038/nmat1780>.
- [15] J. Erlebacher, M.J. Aziz, A. Karma, N. Dimitrov, K. Sieradzki, Evolution of nanoporosity in dealloying, *Nature.* 410 (2001) 450–3. <https://doi.org/10.1038/35068529>.
- [16] J. Erlebacher, An Atomistic Description of Dealloying, *J. Electrochem. Soc.* 151 (2004) C614–C626. <https://doi.org/10.1149/1.1784820>.

- [17] A.J. Forty, Corrosion micromorphology of noble metal alloys and depletion gilding, *Nature*. 282 (1979) 597–598. <https://doi.org/10.1038/282597a0>.
- [18] V. Presser, M. Heon, Y. Gogotsi, Carbide-Derived Carbons - From Porous Networks to Nanotubes and Graphene, *Adv. Funct. Mater.* 21 (2011) 810–833. <https://doi.org/10.1002/adfm.201002094>.
- [19] P.-A. Geslin, I. McCue, B. Gaskey, J. Erlebacher, A. Karma, Topology-generating interfacial pattern formation during liquid metal dealloying, *Nat. Commun.* 6 (2015) 8887. <https://doi.org/10.1038/ncomms9887>.
- [20] S.-G. Yu, K. Yubuta, T. Wada, H. Kato, Three-dimensional bicontinuous porous graphite generated in low temperature metallic liquid, *Carbon*. 96 (2016) 403–410. <https://doi.org/10.1016/j.carbon.2015.09.093>.
- [21] G. Cicero, G. Galli, A. Catellani, Interaction of water molecules with SiC(001) surfaces, *J. Phys. Chem. B*. 108 (2004) 16518–16524. <https://doi.org/10.1021/jp0471599>.
- [22] J. Stuckner, K. Frei, I. McCue, M.J. Demkowicz, M. Murayama, AQUAMI: An open source Python package and GUI for the automatic quantitative analysis of morphologically complex multiphase materials, *Comput. Mater. Sci.* 139 (2017) 320–329. <https://doi.org/10.1016/j.commatsci.2017.08.012>.
- [23] M. Kusunoki, T. Suzuki, T. Hirayama, N. Shibata, K. Kaneko, A formation mechanism of carbon nanotube films on SiC(0001), *Appl. Phys. Lett.* 77 (2000) 531–533. <https://doi.org/10.1063/1.127034>.
- [24] W.W. Zhong, Y.F. Huang, D. Gan, J.Y. Xu, H. Li, G. Wang, S. Meng, X.L. Chen, Wetting behavior of water on silicon carbide polar surfaces, *Phys. Chem. Chem. Phys.* 18 (2016) 28033–28039. <https://doi.org/10.1039/C6CP04686J>.
- [25] I. McCue, A. Karma, J. Erlebacher, Pattern formation during electrochemical and liquid metal dealloying, *MRS Bull.* 43 (2018) 27–34. <https://doi.org/10.1557/mrs.2017.301>.

- [26] Y.K. Chen-Wiegart, S. Wang, I. McNulty, D.C. Dunand, Effect of Ag–Au composition and acid concentration on dealloying front velocity and cracking during nanoporous gold formation, *Acta Mater.* 61 (2013) 5561–5570. <https://doi.org/10.1016/J.ACTAMAT.2013.05.039>.
- [27] J. Räisänen, J. Hirvonen, A. Anttila, The diffusion of silicon in germanium, *Solid State Electron.* 24 (1981) 333–336. [https://doi.org/10.1016/0038-1101\(81\)90027-7](https://doi.org/10.1016/0038-1101(81)90027-7).
- [28] H. Weis, F. Kargl, M. Kolbe, M.M. Koza, T. Unruh, A. Meyer, Self-and interdiffusion in dilute liquid germanium-based alloys, *J. Phys. Condens. Matter.* 31 (2019). <https://doi.org/10.1088/1361-648X/ab354e>.
- [29] I. McCue, B. Gaskey, P.-A. Geslin, A. Karma, J. Erlebacher, Kinetics and morphological evolution of liquid metal dealloying, *Acta Mater.* 115 (2016) 10–23. <https://doi.org/10.1016/J.ACTAMAT.2016.05.032>.
- [30] M. Tsuda, T. Wada, H. Kato, Kinetics of formation and coarsening of nanoporous α -titanium dealloyed with Mg melt, *J. Appl. Phys.* 114 (2013) 113503. <https://doi.org/10.1063/1.4821066>.
- [31] Y. Tanaka, M. Kajihara, Y. Watanabe, Growth behavior of compound layers during reactive diffusion between solid Cu and liquid Al, *Mater. Sci. Eng. A.* 445–446 (2007) 355–363. <https://doi.org/10.1016/j.msea.2006.09.047>.
- [32] H.H. Silvestri, H. Bracht, J.L. Hansen, A.N. Larsen, E.E. Haller, Diffusion of silicon in crystalline germanium, *Semicond. Sci. Technol.* 21 (2006) 758–762. <https://doi.org/10.1088/0268-1242/21/6/008>.
- [33] A. Lee, R. Zhu, M. McNallan, Kinetics of conversion of silicon carbide to carbide derived carbon, *J. Phys. Condens. Matter.*, 18 (2006).
- [34] D.A. Ersoy, M.J. McNallan, Y. Gogotsi, Carbon coatings produced by high temperature chlorination of silicon carbide ceramics, *Mater. Res. Innov.* 5 (2001) 55–62. <https://doi.org/10.1007/s100190100136>.

- [35] Q. Chen, K. Sieradzki, Spontaneous evolution of bicontinuous nanostructures in dealloyed Li-based systems, *Nat. Mater.* 12 (2013) 1102–1106.
<https://doi.org/10.1038/nmat3741>.
- [36] G.W. Liu, M.L. Muolo, F. Valenza, A. Passerone, Survey on wetting of SiC by molten metals, *Ceram. Int.* 36 (2010) 1177–1188.
<https://doi.org/10.1016/J.CERAMINT.2010.01.001>.
- [37] J. Erlebacher, Mechanism of coarsening and bubble formation in high-genus nanoporous metals, *Phys. Rev. Lett.* 106 (2011).
<https://doi.org/10.1103/PhysRevLett.106.225504>.
- [38] B. Gaskey, I. McCue, A. Chuang, J. Erlebacher, Self-assembled porous metal-intermetallic nanocomposites via liquid metal dealloying, *Acta Mater.* 164 (2019) 293–300. <https://doi.org/10.1016/J.ACTAMAT.2018.10.057>.
- [39] F. Tuinstra, J.L. Koenig, Raman Spectrum of Graphite, *J. Chem. Phys.* 53 (1970) 1126–1130. <https://doi.org/10.1063/1.1674108>.
- [40] N. Shimodaira, A. Masui, Raman spectroscopic investigations of activated carbon materials, *J. Appl. Phys.* 92 (2002) 902–909. <https://doi.org/10.1063/1.1487434>.
- [41] M.A. Pimenta, G. Dresselhaus, M.S. Dresselhaus, L.G. Cançado, A. Jorio, R. Saito, Studying disorder in graphite-based systems by Raman spectroscopy, *Phys. Chem. Chem. Phys.* 9 (2007) 1276–1290. <https://doi.org/10.1039/B613962K>.
- [42] A.C. Ferrari, J.C. Meyer, V. Scardaci, C. Casiraghi, M. Lazzeri, F. Mauri, S. Piscanec, D. Jiang, K.S. Novoselov, S. Roth, A.K. Geim, Raman spectrum of graphene and graphene layers, *Phys. Rev. Lett.* 97 (2006) 187401.
<https://doi.org/10.1103/PhysRevLett.97.187401>.
- [43] X. Zheng, W. Chen, G. Wang, Y. Yu, S. Qin, J. Fang, F. Wang, X.A. Zhang, The Raman redshift of graphene impacted by gold nanoparticles, *AIP Adv.* 5 (2015) 057133. <https://doi.org/10.1063/1.4921316>.

- [44] X. Meng, S. Tongay, J. Kang, Z. Chen, F. Wu, S.S. Li, J.B. Xia, J. Li, J. Wu, Stable p- and n-type doping of few-layer graphene/graphite, *Carbon*. 57 (2013) 507–514. <https://doi.org/10.1016/j.carbon.2013.02.028>.
- [45] W.X. Wang, S.H. Liang, T. Yu, D.H. Li, Y.B. Li, X.F. Han, The study of interaction between graphene and metals by Raman spectroscopy, in: *J. Appl. Phys.*, American Institute of Physics, 2011: p. 07C501. <https://doi.org/10.1063/1.3536670>.
- [46] A.C. Ferrari, Raman spectroscopy of graphene and graphite: Disorder, electron-phonon coupling, doping and nonadiabatic effects, *Solid State Commun.* 143 (2007) 47–57. <https://doi.org/10.1016/j.ssc.2007.03.052>.
- [47] L.G. Cañado, K. Takai, T. Enoki, M. Endo, Y.A. Kim, H. Mizusaki, A. Jorio, L.N. Coelho, R. Magalhães-Paniago, M.A. Pimenta, General equation for the determination of the crystallite size l_a of nanographite by Raman spectroscopy, *Appl. Phys. Lett.* 88 (2006) 163106. <https://doi.org/10.1063/1.2196057>.
- [48] B.Z. Li, Y. Wang, L. Xue, X.P. Li, W.S. Li, Acetylene black-embedded $\text{LiMn}_0.8\text{Fe}_0.2\text{PO}_4/\text{C}$ composite as cathode for lithium ion battery, *J. Power Sources*. 232 (2013) 12–16. <https://doi.org/10.1016/j.jpowsour.2013.01.019>.
- [49] R.K. Dash, A. Nikitin, Y. Gogotsi, Microporous carbon derived from boron carbide, *Microporous Mesoporous Mater.* 72 (2004) 203–208. <https://doi.org/10.1016/j.micromeso.2004.05.001>.
- [50] R.K. Dash, G. Yushin, Y. Gogotsi, Synthesis, structure and porosity analysis of microporous and mesoporous carbon derived from zirconium carbide, *Microporous Mesoporous Mater.* 86 (2005) 50–57. <https://doi.org/10.1016/j.micromeso.2005.05.047>.

3 Carbon Transformations in Rapidly Solidified Nickel-Carbon Ribbon

3.1 Summary

We report the chemical and structural transformations of carbon in melt spun and annealed nickel-carbon ribbons. We attained metastable solid solubility of carbon in nickel ribbon by achieving a rapid solidification rate of up to 1.6×10^6 K/s. Excess carbon atoms were found to be dissolved in the nickel lattice causing up to 2% strain for an alloy spun at 80 m/s tangential wheel speeds. High temperature heat treatments led to precipitation of carbon from the nickel lattice on the ribbon free surfaces but also led to growth of spherical precipitates within the nickel matrix via bulk diffusion-driven Ostwald ripening.

3.2 Introduction

The morphology of graphite precipitated from metallic melts has long been of scientific interest [1]. Cast iron, one of the world's most industrially significant casting materials, contains ~ 2 - 7 wt.% carbon and its properties vary depending on the microstructure of the carbon precipitated within it. When the precipitated graphite is flake-shaped, cast iron exhibits good compressive strength but low ductility. "Ductile iron," with improved mechanical properties, was discovered in the 1940s when researchers added small quantities of impurities to the melt that converted the graphite morphology from flakes to spheroids [2]. While flakes and spheroids are generally distributed within the bulk of cast iron, Kish graphite, which exhibits a foliated dendritic

structure, is formed from carbon atoms that segregate on the surface of carbon-saturated cast iron liquid as it cools [3,4].

The use of nickel and other metals as catalysts for the growth of graphitic materials has been under investigation since the 1970s. Derbyshire et al. [5] reported the crystallization of amorphous carbon (a-C) on Ni thin films and postulated a process of carbon dissolution into the metal followed by graphite precipitation on the surface upon cooling – the dissolution-precipitation mechanism. The discovery of graphene in 2004 [6] has led to a surge in studies investigating the synthesis of the novel material on metal substrates. As a result, the technique described by Derbyshire has been refined to fabricate single and multi-layer graphene via the conversion of solid carbon sources, such as polymers [7] or amorphous carbon [8–12] on Ni thin films via thermal annealing. Various mechanisms to explain the crystallization reaction have been proposed. While some researchers maintain the traditional dissolution-precipitation theory, Saenger et al. postulated metal induced crystallization as the mechanism for graphene synthesis [12], owing to the detection of the graphite (002) peak by in situ XRD during the heating stage, whereas one would expect the evolution of the graphite peak only during cooling for the dissolution-precipitation mechanism. Wensich et al. proffered another explanation involving surface diffusion at low temperatures (≤ 600 °C) since bulk diffusion was an unlikely transport mechanism in the temperature ranges investigated [11]. Alternatively, Li and others [8] proposed a metal-induced layer exchange process, where the amorphous carbon and Ni exchanged positions in a Si-SiO₂/a-C/Ni sandwich structure to form graphene on the Ni free surface. Because no C remained in the newly formed SiO₂/Ni

interface, the dissolution-precipitation mechanism was deemed inconsistent with the observation.

Researchers have also grown graphene and graphite nanocrystals by dissolving graphite powder in molten nickel and other metals at high temperatures, followed by carefully controlled cooling steps to facilitate the nucleation and growth of single or multiple layers of carbon atoms on the liquid surface [13–16]. Alternatively, one of the most well-studied methods to grow graphene is by chemical vapor deposition (CVD), whereby carbon-containing gaseous precursors are thermally decomposed on metal foils that catalyze the formation of the single layer of graphite [17]. In both methods, the mechanism of graphene formation is similar, namely, carbon dissolution into the substrate followed by precipitation on the surface [15].

Yu et al. postulated that graphene formation on Ni foils via CVD involves the transport of vacancy-carbon complexes to grain boundaries and surfaces (which act as sinks), a process strongly dependent on the cooling technique [13]. They, therefore, studied the effect of different cooling rates on the growth of graphene corresponding to fast (20 K/s), medium (10 K/s) and slow (0.1 K/s) cooling rates on Ni substrates exposed to precursor hydrocarbon gas for a short time. At the slowest cooling rate, no graphene was observed because the carbon atoms had sufficient time to diffuse into the bulk metal, whereas the medium cooling rate resulted in the formation of few layer graphene. The fastest cooling rate resulted in graphite with a high concentration of defects as the quenching prevented the atoms from re-arranging into their equilibrium crystalline form. Huang and colleagues were also able to synthesize single and few-layer graphene using a rapid CVD technique and a cooling rate of 3 K/s [18].

In an attempt to develop a faster method than CVD to produce high quality graphene, Hu et al. examined rapid solidification via melt-spinning of nickel-carbon melts [19]. Invented by British scientists Strange and Pim in 1908, melt spinning has been used to manufacture sheets and ribbons of various metals [20]. In this process, a molten stream of metal impinges onto a spinning metal wheel and solidifies into a ribbon. Heat from the liquid is extracted via conduction through the wheel, leading to cooling rates that can exceed 10^6 K/s [21]. Compared to conventional solidification methods, rapid solidification techniques can produce microstructures with fine grains (even metallic glasses), extended solid solubility and metastable phases [22]. The primary application of this method has been the manufacture of metallic glasses for soft magnetic transformer cores and shape memory alloys [23–26].

The work performed by Hu and others shows that melt spinning is also a viable method to produce graphene. In their study, nickel alloy ingots containing less than 5 at. % carbon were prepared, melted by RF induction heating, and ejected onto a copper wheel rotating at tangential surface speeds of 25 – 50 m/s. Meters-long ribbon, with thicknesses that varied between 50 – 200 μm were produced; the free surfaces were found to be encased in few-layer graphene. Our analysis of their data suggested a noteworthy observation, namely, that because the solubility of carbon in solid nickel is 2 at. % at the eutectic temperature, most of the precursor carbon did not segregate to the surface of the ribbon to form graphene. Because graphene is likely formed by bulk diffusion of carbon to the free surface, i.e., the usual mechanism, we surmised that most of the carbon was still uniformly dissolved in the matrix of nickel. If so, then rapid solidification presented

a new route to a metastable carbon-containing precursor, and that heat treatments could be used to control the microstructure of precipitated carbon in novel ways.

In this chapter, we present a study of the morphological and chemical transformation that occurs when carbon is precipitated from melt spun nickel-carbon alloys. Overall, we find our hypothesis is justified – that melt-spun nickel carbon is indeed supersaturated with carbon, and that heat treatments can be used to control the precipitation kinetics.

3.3 Experimental Methods

3.3.1 Alloy Preparation

Nickel-carbon alloy ingots were prepared by inductively melting the constituents in a water-cooled copper crucible using a 45 kW Ambrell Ekoheat ES induction system under a flowing Ar atmosphere. The precursor alloys used in the subsequent melt-spinning experiments were (measured in at. %): Ni₉₆C₄, Ni₉₂C₈, Ni₉₀C₁₀, Ni₈₈C₁₂, where the constituent Ni (99.98 wt. %) was purchased from Kurt J. Lesker and graphite (99.995 wt. %) from Sigma Aldrich.

3.3.2 Melt Spinning

The components of the melt spinner (Arcast Inc.) are shown in Figure 3-1 and are enclosed in a stainless steel vacuum chamber. The equipment consists of (i) a boron nitride crucible with a 3/64" diameter nozzle that was machined in-house (the crucible head was replaced every three runs or when the nozzle was abraded beyond repair), (ii) RF induction coils, and (iii) the copper wheel (300 mm diameter and 50 mm wide) that was water-cooled to 13 °C during experiments, and (iv) a collection tube for ribbon.

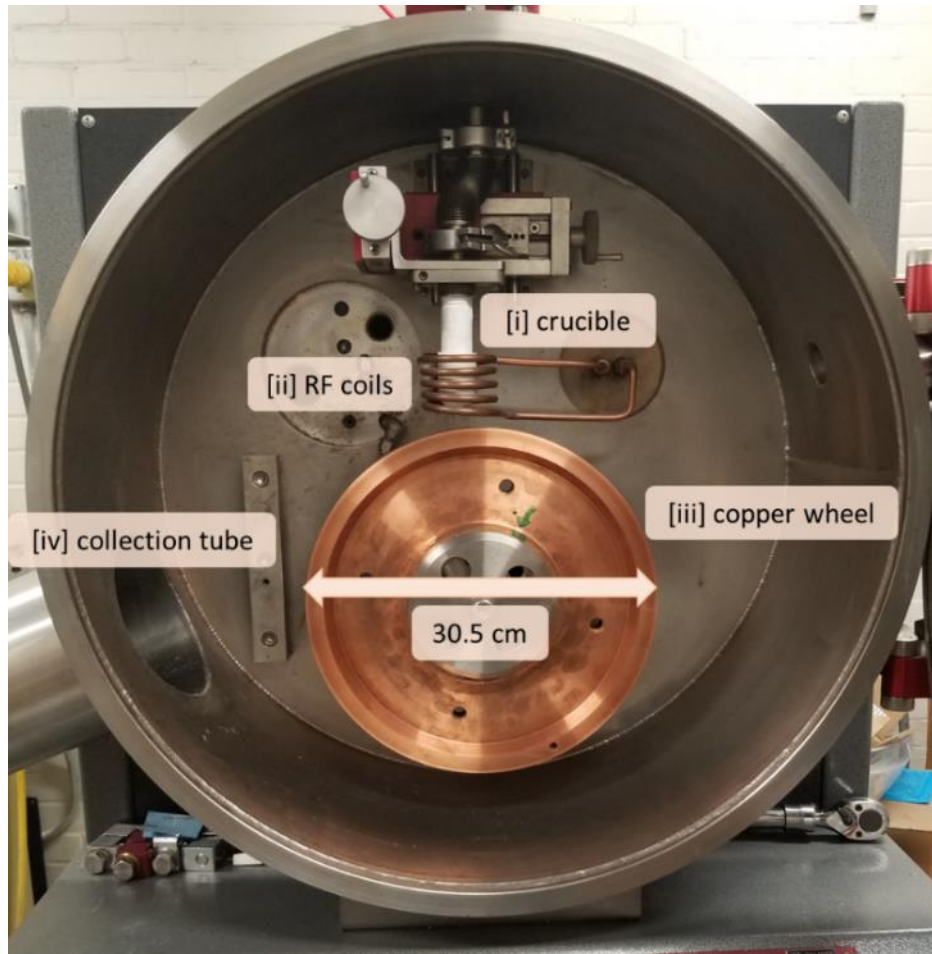


Figure 3-1. (a) Photograph showing major components of the melt spinning apparatus. (i) A typical boron nitride crucible that houses the pre-cast nickel carbon ingot is shown. (ii) RF coils surround the base of the crucible and are used to melt the ingot. The melt is ejected onto the surface of (iii) the water-cooled copper wheel and solidified into ribbon that is retrieved from (iv) the collection tube.

In a typical experiment, an approximately 20 g alloy ingot charge was inserted into the crucible, the chamber was evacuated and backfilled with purified argon to -10 psig. The charge was melted via RF induction heating using a 15 kW power supply and the temperature was monitored using a Dias Pyrospot DS 56 N pyrometer. The crucible was then lowered to a preset distance (about 1 mm) above the rotating wheel and the molten alloy was ejected via pressurized argon. The jet forms a melt pool on the cold copper

surface and solidifies into a ribbon that is typically several meters in length, ~1-3 mm wide and with a thickness in the range of 20 – 50 μm , depending on experimental parameters. The wheel rotation rate was varied between 2500 and 5000 rpm, corresponding to a surface tangential speed of 40 – 80 m/s. Above 80 m/s, excessive sticking of the ribbon to the wheel occurred, a phenomenon discussed in detail by Liebermann and others [27,28]. Typically, the entire 20 g ingot was spun into ribbon within 5 seconds.

Ribbon microstructures, plan view and cross-section, were investigated using Scanning Electron Microscopy (SEM) and Transmission Electron Microscopy (TEM). Composition analysis was performed using Energy Dispersive Spectroscopy (EDS) and phase analysis was conducted via X-ray Diffraction (XRD). The wheel was prepared between each run by polishing with silicon carbide sanding sheets of incrementally decreasing grit size, and because the literature concludes that the wheel speed is the most important parameter that affects the cooling rate [29], the ejection pressure and melt superheat were kept constant and only the wheel velocity was varied.

A minimum of 3 ribbon samples were made under the same synthesis conditions. Selected samples were mounted longitudinally in epoxy, polished, and the microstructure of the ribbon cross-section was examined via SEM. Plan view SEM micrographs were obtained by mounting the ribbon horizontally on SEM stubs. Sections were removed via FIB in preparation for TEM imaging. Ribbon thicknesses were measured using a digital micrometer, and a minimum of 4 measurements were taken for each sample and averaged.

3.3.3 Thermal annealing of melt spun ribbon

The melt-spun ribbons with varying carbon contents were annealed in a tube furnace under a flowing Ar atmosphere (99.999 %) at different temperatures: 400 °C, 800 °C, 1000 °C and 1200 °C for 60 minutes. To observe the effect of annealing time on the microstructure of the ribbon, Ni₉₂C₈ ribbon was annealed at 1000 °C for 1 minute, 30 minutes and 240 minutes. After annealing, the ribbons in each of these experiments were cooled slowly at 0.06 K/s, from their respective annealing temperatures to room temperature.

3.3.4 Characterization tools

SEM imaging was performed using a Thermo Scientific Helios G4 UC Focused Ion Beam/ Scanning Electron Microscope (FIBSEM) instrument equipped with an energy dispersive spectroscopy (EDS) detector which was used for compositional analysis. The FIBSEM instrument was also used to prepare samples for imaging using the Thermo Scientific TF30 Transmission Electron Microscope (TEM). XRD was performed with a Bruker D8 Focus diffractometer with a CuK α source.

3.4 Results and Discussion

3.4.1 Microstructural evolution of melt-spun ribbon

Conventional solidification typically proceeds at cooling rates lower than 100 K/s and generally results in phases and microstructures predicted by equilibrium thermodynamics [30]. However, melt spinning is a far-from-equilibrium cooling technique where solidification rates between $10^4 - 10^7$ K/s are encountered [22]. As a result, phases and microstructures that are favored kinetically instead of thermodynamically may evolve. The Ni-C phase diagram is a simple eutectic with a

eutectic composition and temperature of Ni_{92}C_8 and $1326\text{ }^\circ\text{C}$, respectively, and a maximum solubility of carbon in the nickel phase of ~ 2 at. % at the eutectic temperature. Figure 3-2(a) shows a comparison of the microstructure of a Ni_{92}C_8 ingot conventionally cooled in an induction furnace and the cross-section of melt spun ribbon of the same composition. The lighter regions are the Ni-rich phase and the darker regions are carbon particles embedded in the metal. As expected, the conventionally cooled ingot shows a dendritic microstructure as well as visible carbon precipitates. In contrast, the melt-spun ribbon shows a featureless, uniform Ni phase with no visible carbon precipitation, suggesting that melt spinning results in a metastable solid solubility of carbon in the metal.

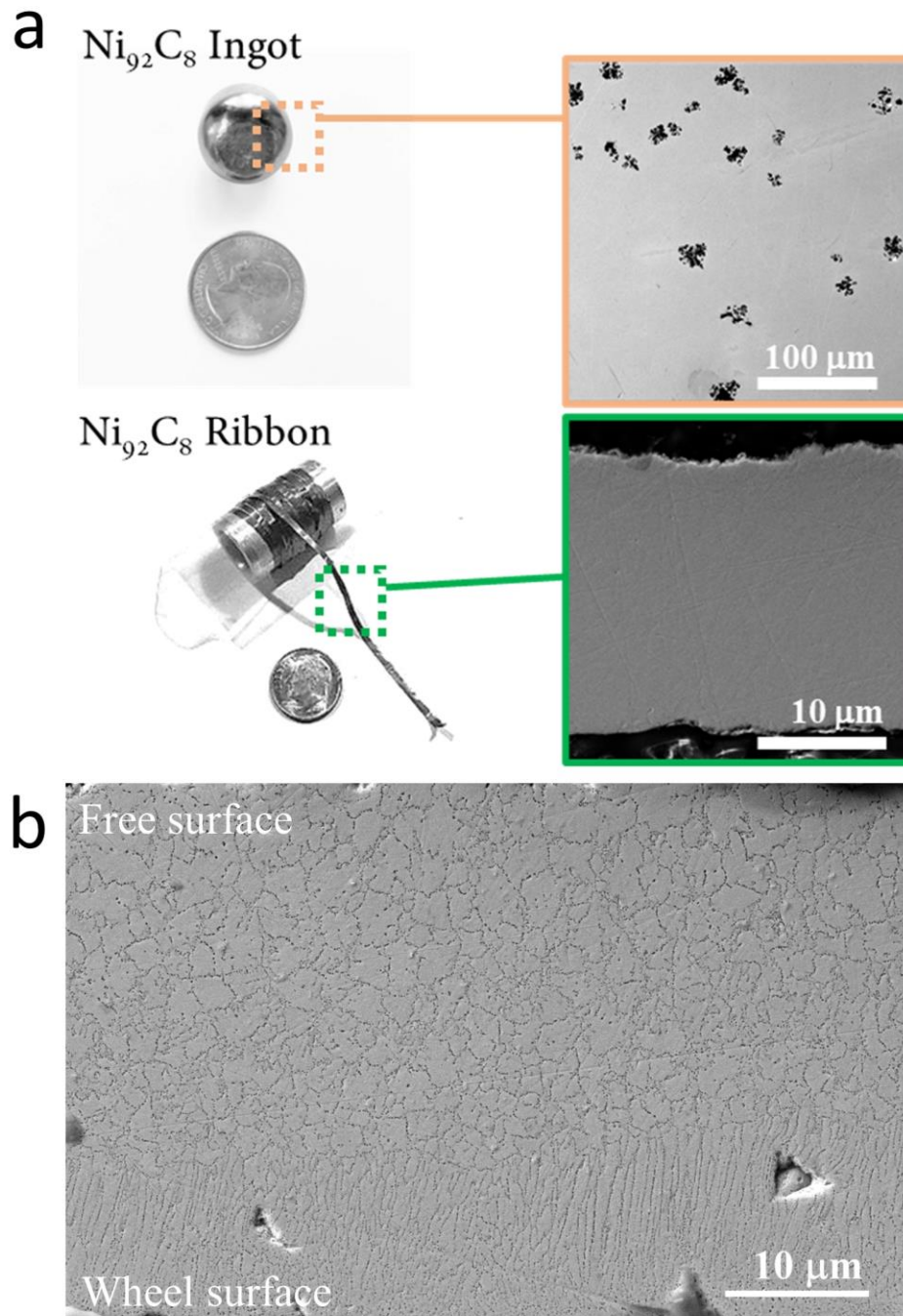


Figure 3-2. (a) Micrographs depicting the difference in microstructure of Ni_{92}C_8 cast in an induction furnace and that of melt-spun ribbon of the same composition. A dendritic solidification microstructure with visible carbon precipitation in the nickel is seen in the ingot while a homogeneous single phase is observed for the melt-spun ribbon. (b) Cross-section of $\text{Ni}_{88}\text{C}_{12}$ ribbon showing a typical melt-spun microstructure. Carbon precipitates highlight the evolution of the grain structure from the ribbon surface that was in contact with the wheel to the ribbon free surface.

In melt spinning, a molten alloy jet is ejected on a rotating metal wheel substrate to form a ribbon or strip. A melt puddle is formed on the substrate from which quenched ribbon is continually expelled. The wheel surface acts both as a heat sink and heterogenous nucleation site for the growth of solid phases. Typically, solidification begins in the form of fine, equiaxed crystals and extends laterally until the contact surface is covered. From this initial chill zone, columnar grains grow in the direction parallel to the thermal gradient, i.e., normal to the ribbon surface. In Ni alloys, the preferential growth direction of the columnar grains is the [100] direction [31]. With sufficient cooling rates, the early stage of columnar solidification is partitionless; that is, the solidification velocity is faster than the diffusion of solutes, which become trapped in the solid phase. The equilibrium partition coefficient $k = c_S/c_L$ is generally less than unity but can approach $k = 1$ in rapid solidification processes [32], and the equilibrium solid solubility can be greatly exceeded. As the solidification front advances from the contact surface to the free surface, the latent heat of solidification is released, reducing the thermal gradient and the interface velocity. When solidification is no longer partitionless, the microstructure of the ribbon transitions into a cellular configuration with much larger grains.

As shown in Figure 3-2(b), the solidification microstructure of $\text{Ni}_{88}\text{C}_{12}$ follows the expected behavior, transitioning from fine equiaxed crystals to columnar to larger cellular grains. As discussed below, most of the carbon is dissolved in the solidified nickel matrix; however, there is a small amount of carbon that segregates to grain boundaries, allowing the microstructural features to be highlighted.

Many experimental parameters affect the cooling rate, including the melt superheat, the ejection gas pressure, wheel material and its surface finish, and the wheel velocity. Increasing the wheel velocity increases the cooling rate due to improved thermal contact between the ribbon and the substrate, but also because it results in a decrease in ribbon thickness [30]. Thickness has been described as the most important feature of melt-spun ribbon that determines the cooling rate, where the average cooling rate increases approximately as the inverse square of ribbon thickness for ideal cooling [29,31,33]. The cooling rate is directly proportional to the wheel velocity and inversely to the square of ribbon thickness.

We investigated the relationship between wheel speed and ribbon thickness to determine the optimal conditions under which continuous, uniform, thin, rapidly solidified ribbons were produced. We kept constant the surface finish, melt superheat, and ejection pressure and varied only the wheel velocity and carbon content.

Figure 3-3 shows this observed relationship, where ribbon thickness (h) decreases with wheel velocity (v) as

$$h \propto k / v^{0.6} \quad (1)$$

where k is a constant. The experimentally derived exponent reported here is in close agreement with the equation derived by Gillen and colleagues [34]:

$$h \propto Q / v^{2n} \quad (2)$$

where Q is the volumetric flow rate and n is in the range 0.3 - 0.4. Specifically, n was found to be 0.35 for Ni-5wt%Al. Jones et al. proffered a slightly different variation of Gillen's equation in which

$$h \propto Q^n / v^m \quad (3)$$

where n and m are typically 0.2 and 0.8, respectively [30] which is still in good agreement with the relationship reported in this work. Gillen also derived a linear equation relating wheel speed to cooling rate that is independent of other melt spinning experimental parameters and the alloy material:

$$= a_4 v \tag{4}$$

where is the cooling rate and a_4 is a constant of proportionality equal to 1.2×10^4 K/s.

Using Eq. (4), we estimate the cooling rates achieved in the melt spinning of nickel-carbon alloys in this work were in the range $9.6 \times 10^5 - 1.9 \times 10^6$ K/s.

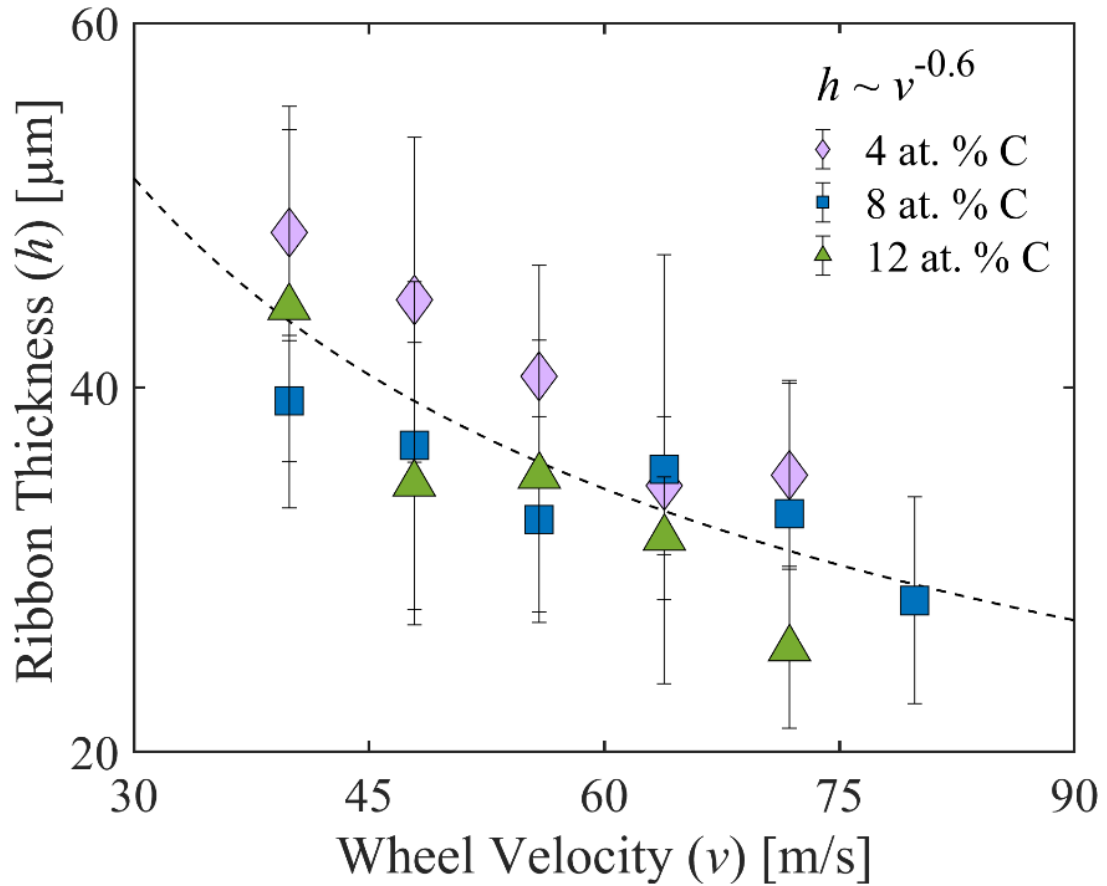


Figure 3-3. Ribbon thickness (h) vs. tangential wheel velocity (v) for different carbon fractions: Ni containing 4 at. % C (purple, diamonds), 8 at. % C (blue, squares), 10 at. % C (green, triangles).

The effect of thermal annealing on the ribbon microstructure was also investigated. TEM images comparing as-prepared ribbon with ribbon annealed at 1000 °C is shown in Figure 3-4. The TEM micrograph of a sample before annealing shows a homogenous region of sub-micron sized Ni grains with no obvious carbon precipitates observable within the resolution of the image. In contrast, after annealing, Ni grains have grown and carbon precipitates are also evident; the polygonal outline of a graphite precipitate is shown in the inset.

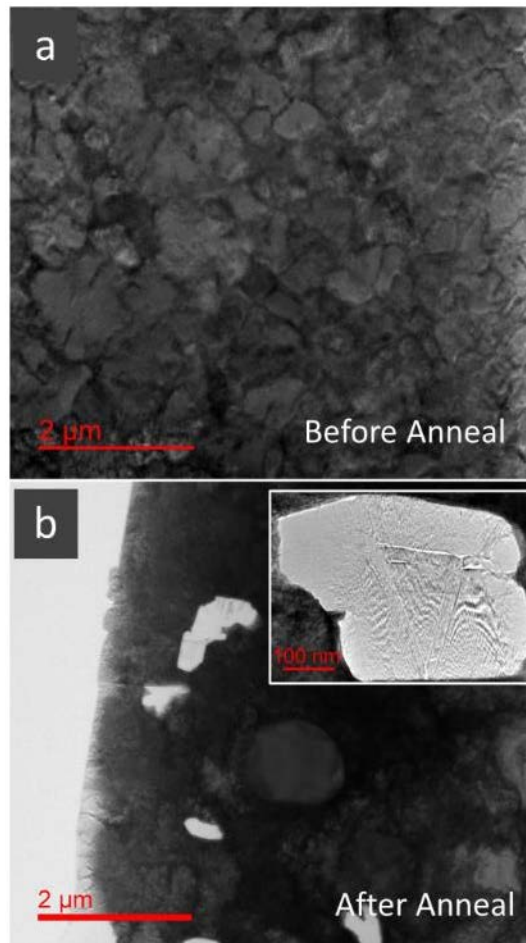


Figure 3-4. TEM micrographs of Ni_{92}C_8 ribbon. (a) Image taken before annealing show micron-sized grains and no evidence of carbon precipitation. (b) Image of ribbon annealed at 1000 °C for 1 hour show grain growth and the presence of large graphite particles (light particles) embedded in the Ni matrix (inset).

The evolution of the XRD patterns in response to annealing follows. The data labeled (i) in Figure 3-5(a) shows the diffraction pattern of melt spun pure Ni ribbon. The XRD pattern of as-spun Ni₉₂C₈ ribbon is also shown, labeled (ii). Compared to pure Ni, the (100) peak in this sample is shifted to smaller 2θ due to a 0.75% lattice expansion, consistent with supersaturation of carbon in the interstitial sites of the nickel lattice due to the high cooling rates. The XRD pattern of Ni₉₂C₈ ribbon was annealed at 1000 °C for 1 hour is shown as (iii) and indicates the Ni lattice peak has returned to the unstrained position, indicating that the lattice strain is relieved during carbon precipitation. Details of annealing the nickel-carbon ribbon will be further discussed in Chapter 3.4.2.

We also investigated the effect of wheel speed on the strain observed in the lattice spacings for Ni ribbon with increasing quantities of added graphite. As shown in Figure 3-5(b), negligible strain was observed in the Ni₉₆C₄ ribbon at any wheel speed and the Ni d_{hkl} remains virtually unchanged, indicating that a small quantity of carbon is easily accommodated by the Ni lattice. However, for Ni₉₂C₈ and Ni₉₀C₁₀ compositions, the d_{hkl} values increase, corresponding to up to 2% strain in the as-spun ribbon. The increase in strain is proportional to an increase in wheel velocity, consistent with the notion that higher cooling rates lead to higher supersaturation.

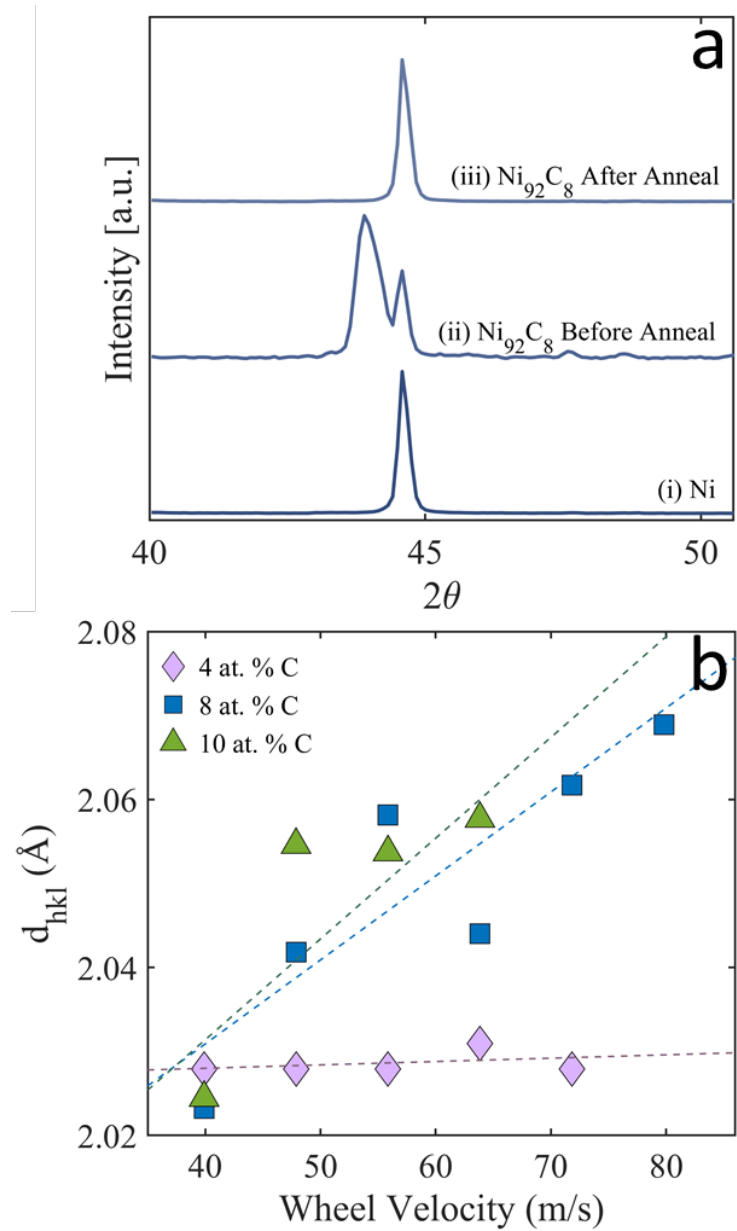


Figure 3-5. (a) XRD patterns showing the effect of annealing on the Ni peak positions in melt-spun ribbon prepared under the same conditions. (i) Shows unstrained Ni (111) peak. (ii) Shows a Ni (111) peak shift to a smaller 2θ indicating lattice expansion. The peak shoulder is the $K\alpha_2$ peak. (iii) Shows that annealing relieves the lattice strain. (b) Plot of lattice spacings in melt spun Ni-C ribbon with different carbon fractions as a function of tangential wheel velocity: Ni containing 4 at. % C (purple diamonds), 8 at. % C (blue squares), 10 at. % C (green triangles). Little to no change in d_{hkl} is observed for ribbon containing 4 at.% C indicating minimal strain, but for material with higher carbon fractions, d_{hkl} increases monotonically with wheel velocity, indicating increasing amounts of saturation of the Ni lattice with carbon.

3.4.2 The effect of annealing temperature and time on carbon precipitation

To re-iterate, as-spun ribbons generally accommodated a great deal of supersaturated carbon. However, as Figure 3-2(b) shows, we commonly observed some carbon precipitation at Ni grain boundaries, with a few ribbons containing regions where this segregation did not occur; the ribbon appeared as uniform and featureless within the resolution of the scanning electron microscope, such as shown in Figure 3-2(a). After annealing, however, C precipitates were uniformly dispersed throughout the matrix, no longer distinctly outlining Ni grains.

We now turn to the question of the morphological evolution of carbon precipitated from the ribbons which coarsen as a result of a thermal anneal. It seems reasonable to consider that growth of precipitates is controlled by an evaporation/condensation mechanism wherein carbon atoms dissolve from precipitates, diffuse down chemical potential gradients through the bulk of the nickel matrix, and re-attach to other precipitates. To date, we know of no study that suggests whether the rate limiting step in the nickel-carbon system is bulk diffusion or attachment/detachment at precipitates, and the situation is made more complex here by the presence of grain boundaries and surfaces that may act as short-circuit diffusion pathways. We emphasize that a coarsening study of precipitates embedded in a nickel matrix is fundamentally different than a study of graphitization of particles excavated from carbon, as graphitization does not generally involve long-range transport of carbon atoms.

The temporal evolution of carbon coarsening in Ni_{92}C_8 ribbon was first examined by performing 1000 °C isothermal heat treatments at varying times: 1 minute, 30 minutes, 60 minutes and 240 minutes. This step was followed by cooling and cross-sectioning for

microscopy; the cooling rate was kept constant for all experiments. Figure 3-6(a) shows micrographs of the carbon precipitates at annealing times up to 4 hours. It is clear that the average particle size has grown from initially submicron particles to particle sizes as large as 5 μm after the 4 hour anneal. Generally, precipitate coarsening is governed by the power law $d \propto t^n$, where d is the average precipitate size, t is the annealing time and n is an exponent that varies depending on the coarsening mechanism. The Lifshitz-Slyozof-Wagner (LSW) theory of Ostwald ripening [35,36] models the kinetics of precipitate growth from supersaturated solid solutions and is often referenced in the literature to describe the coarsening mechanism in rapidly solidified materials [37–39]. LSW theory predicts that $n = 1/3$ for diffusion-limited coarsening [40,41]. A plot of mean particle size vs. annealing time is shown in Figure 3-6(b), with an $n = 1/3$ power law relationship shown by a dashed line, showing good agreement between the data and model.

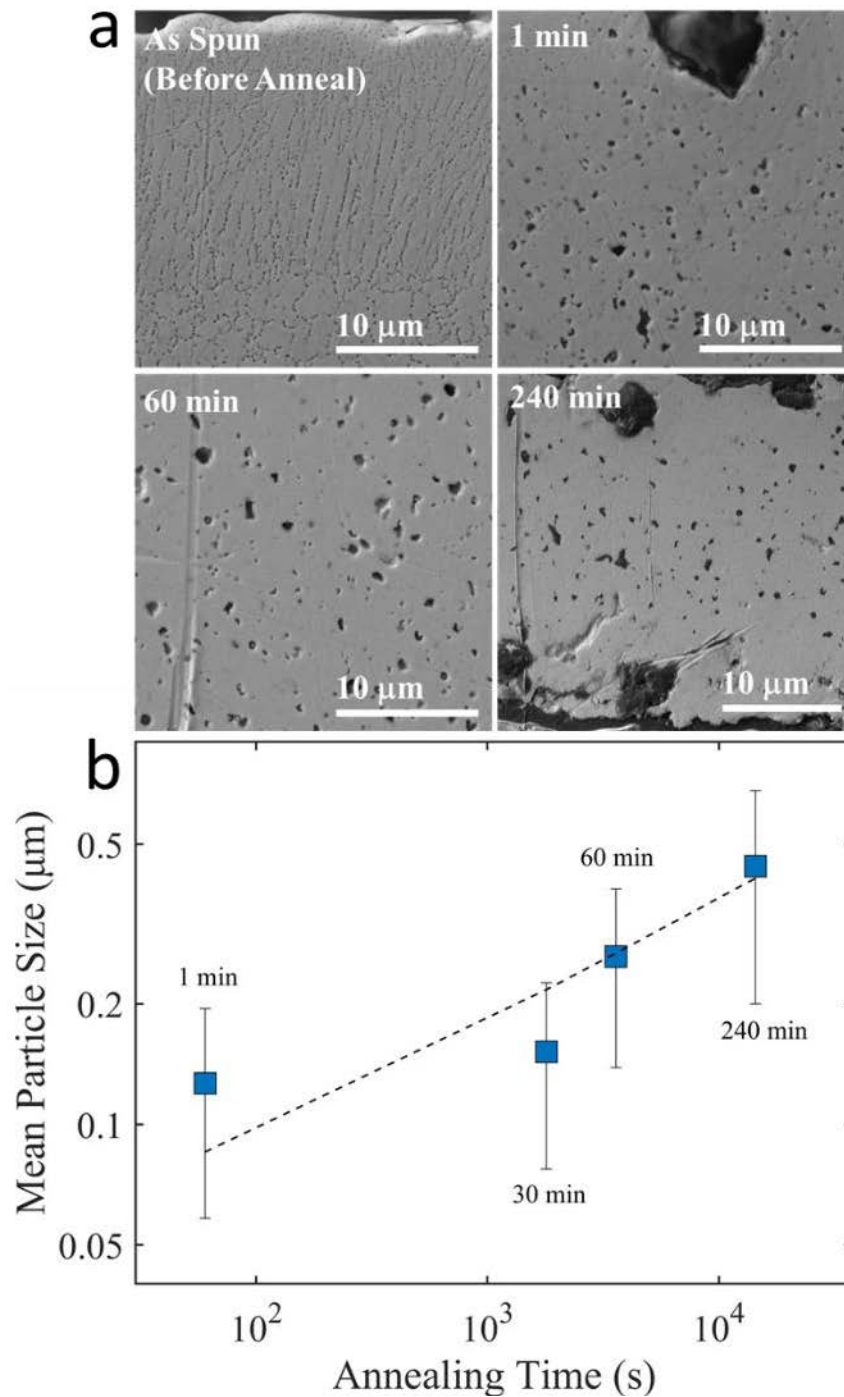


Figure 3-6. (a) SEM micrographs showing growth of carbon precipitates in Ni_{92}C_8 ribbon annealed at $1000\text{ }^\circ\text{C}$ for increasing times. (b) Log-Log plot of mean particle size as a function of time. The dashed line shows a power law fit with $n = 1/3$.

To further elucidate the mechanism of precipitate coarsening, ribbons were examined after a fixed annealing time but at multiple annealing temperatures and carbon content. Micrographs of representative samples are shown in Figure 3-7(a). An increase in the annealing temperature led to an increase in the size of the carbon precipitates and a reduction in the number density of precipitates. Regardless of the mechanism dominating coarsening, the average particle size should be proportional to a kinetic factor exhibiting Arrhenius kinetics, either diffusion coefficient D in diffusion-limited kinetics or an attachment/detachment rate k_a , and the particle size data for the annealing temperature range of 800 – 1200 °C plotted in Figure 3-7(b) does indeed exhibit Arrhenius type behavior. The activation barrier, 1.43 eV, is consistent with other measurements of carbon diffusion in Ni above 600 °C, which was found to be in the range 1.42 – 1.52 eV [42]. At temperatures below 550 °C, Wenisch [11] observed surface diffusion is the primary mechanism of carbon transport on Ni but hypothesized that bulk diffusion rates would reach comparable values at the higher temperatures reported in this manuscript. Weatherup [43] noted that for an increase in growth temperature from 300 – 600 °C, there is a more than five orders of magnitude increase in the lattice diffusivity of carbon in Ni but pointed out grain boundary and surface diffusion would also be greatly increased.

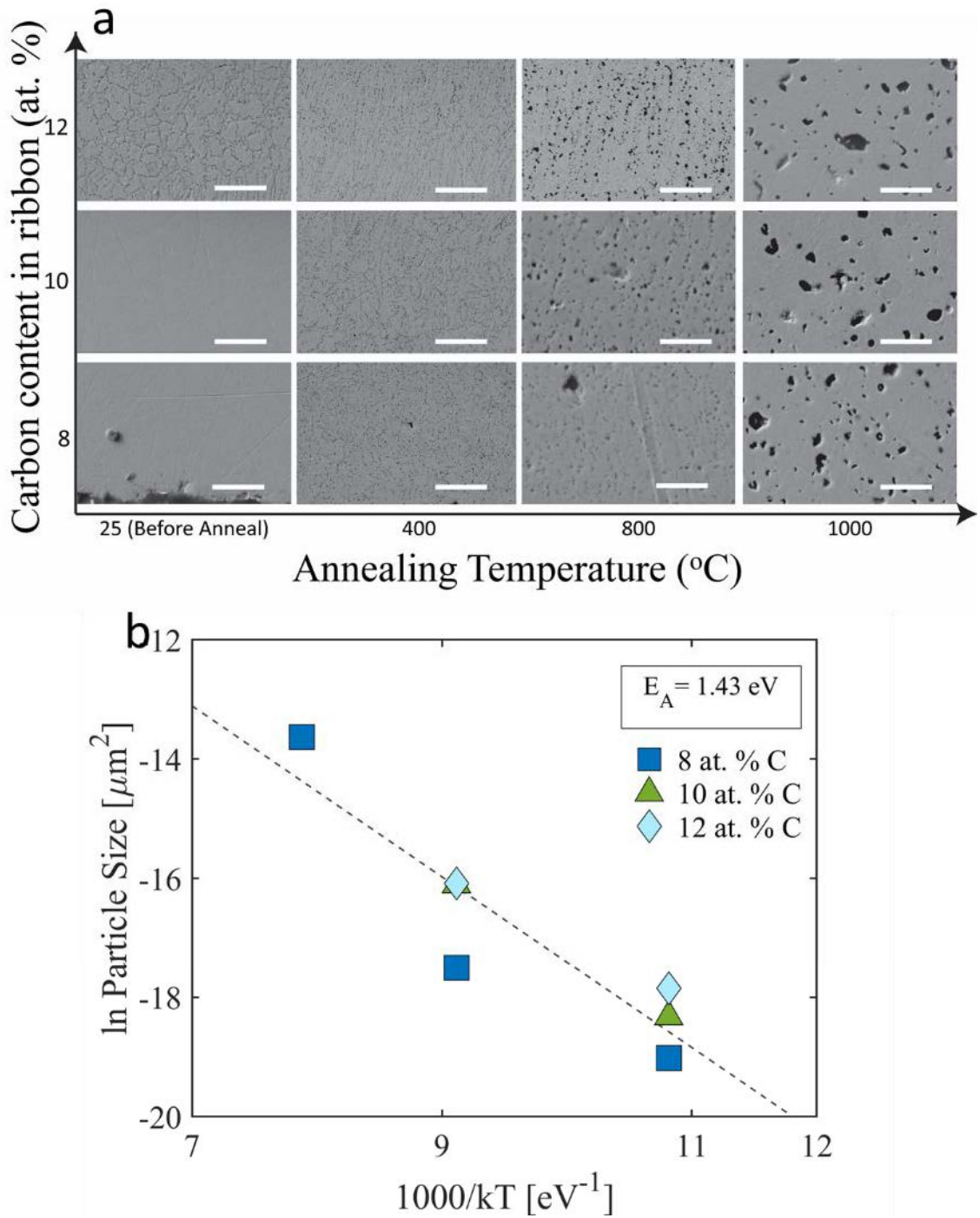


Figure 3-7. (a) Microstructural variation of melt-spun Ni-C ribbon (cross-section) with varying carbon content and annealed at different temperatures. Scale bars are 5 μm. (b) Plot of average carbon particle size in ribbon vs. annealing temperature for Ni-C ribbon of varying carbon fractions: Ni containing 8 at. % C (dark blue squares), 10 at. % C (green triangles) and 12 at. % C (light blue diamonds). The activation energy of 1.43 eV is consistent with bulk diffusion of carbon in Ni.

3.5 Conclusions

We report the ability to melt spin nickel-carbon alloys with a carbon fraction up to 12 at. % using a water-cooled copper roller rotating at speeds between 40 to 80 m/s. Extended solubility of carbon in the Ni was confirmed by measuring Ni lattice strain using X-ray diffraction. High temperature heat treatments led to precipitation of carbon from the nickel lattice on the ribbon free surfaces but also led to the subsequent growth of the precipitates within the nickel matrix via bulk diffusion-driven Ostwald ripening. ribbon produced thick graphite flakes from carbon material precipitated on the surfaces of the ribbon.

3.6 References

- [1] D.M. Stefanescu, Solidification and modeling of cast iron - A short history of the defining moments, *Mater. Sci. Eng. A.* 413–414 (2005) 322–333.
<https://doi.org/10.1016/j.msea.2005.08.180>.
- [2] K. Theuwissen, J. Lacaze, L. Laffont, Structure of graphite precipitates in cast iron, *Carbon.* 96 (2016) 1120–1128. <https://doi.org/10.1016/j.carbon.2015.10.066>.
- [3] E. Matuyama, Structure of kish and other graphites, *Nature.* 183 (1959) 670–671.
<https://doi.org/10.1038/183670b0>.
- [4] S. Liu, C.R. Loper, The formation of kish graphite, *Carbon.* 29 (1991) 547–555.
[https://doi.org/10.1016/0008-6223\(91\)90119-4](https://doi.org/10.1016/0008-6223(91)90119-4).
- [5] F.J. Derbyshire, A.E.B. Presland, D.L. Trimm, Graphite formation by the dissolution-precipitation of carbon in cobalt, nickel and iron, *Carbon.* 13 (1975) 111–113. [https://doi.org/10.1016/0008-6223\(75\)90267-5](https://doi.org/10.1016/0008-6223(75)90267-5).
- [6] K.S. Novoselov, A.K. Geim, S. V Morozov, D. Jiang, Y. Zhang, S. V Dubonos, I. V Grigorieva, A.A. Firsov, Electric field effect in atomically thin carbon films., *Science.* 306 (2004) 666–9. <https://doi.org/10.1126/science.1102896>.
- [7] H. Peng, G. Ma, K. Sun, J. Mu, Z. Zhang, Z. Lei, Formation of carbon nanosheets via simultaneous activation and catalytic carbonization of macroporous anion-exchange resin for supercapacitors application, *ACS Appl. Mater. Interfaces.* 6 (2014) 20795–20803. <https://doi.org/10.1021/am505066v>.
- [8] H. Li, X. Li, J. Wei, Z. Wang, P. Guo, P. Ke, H. Saito, P. Cui, A. Wang, Crystalline transformation from ta-C to graphene induced by a catalytic Ni layer during annealing, *Diam. Relat. Mater.* 101 (2020) 107556.
<https://doi.org/10.1016/j.diamond.2019.107556>.
- [9] W. Xiong, Y.S. Zhou, L.J. Jiang, A. Sarkar, M. Mahjouri-Samani, Z.Q. Xie, Y.

Gao, N.J. Ianno, L. Jiang, Y.F. Lu, Single-Step Formation of Graphene on Dielectric Surfaces, *Adv. Mater.* 25 (2013) 630–634.
<https://doi.org/10.1002/adma.201202840>.

- [10] M. Zheng, K. Takei, B. Hsia, H. Fang, X. Zhang, N. Ferralis, H. Ko, Y.-L. Chueh, Y. Zhang, R. Maboudian, A. Javey, Metal-catalyzed crystallization of amorphous carbon to graphene, *Appl. Phys. Lett.* 96 (2010) 63110.
<https://doi.org/10.1063/1.3318263>.
- [11] R. Wenisch, R. Hübner, F. Munnik, S. Melkhanova, S. Gemming, G. Abrasonis, M. Krause, Nickel-enhanced graphitic ordering of carbon ad-atoms during physical vapor deposition, *Carbon.* 100 (2016) 656–663.
<https://doi.org/10.1016/j.carbon.2015.12.085>.
- [12] K.L. Saenger, J.C. Tsang, A.A. Bol, J.O. Chu, A. Grill, C. Lavoie, In situ x-ray diffraction study of graphitic carbon formed during heating and cooling of amorphous-C/Ni bilayers, *Appl. Phys. Lett.* 96 (2010) 153105.
<https://doi.org/10.1063/1.3397985>.
- [13] Q. Yu, J. Lian, S. Siriponglert, H. Li, Y.P. Chen, S.S. Pei, Graphene segregated on Ni surfaces and transferred to insulators, *Appl. Phys. Lett.* 93 (2008) 113103.
<https://doi.org/10.1063/1.2982585>.
- [14] S. Amini, H. Kalaantari, J. Garay, A.A. Balandin, R. Abbaschian, Growth of graphene and graphite nanocrystals from a molten phase, *J. Mater. Sci.* 46 (2011) 6255–6263. <https://doi.org/10.1007/s10853-011-5432-9>.
- [15] L. Baraton, Z.B. He, C.S. Lee, C.S. Cojocaru, M. Châtelet, J.-L.L. Maurice, Y.H. Lee, D. Pribat, M. Chtelet, J.-L.L. Maurice, Y.H. Lee, D. Pribat, On the mechanisms of precipitation of graphene on nickel thin films, *EPL.* 96 (2011) 46003. <https://doi.org/10.1209/0295-5075/96/46003>.
- [16] S. Amini, J. Garay, G. Liu, A.A. Balandin, R. Abbaschian, Growth of large-area graphene films from metal-carbon melts, *J. Appl. Phys.* 108 (2010) 094321.

<https://doi.org/10.1063/1.3498815>.

- [17] A. Reina, X. Jia, J. Ho, D. Nezich, H. Son, V. Bulovic, M.S. Dresselhaus, K. Jing, Large area, few-layer graphene films on arbitrary substrates by chemical vapor deposition, *Nano Lett.* 9 (2009) 30–35. <https://doi.org/10.1021/nl801827v>.
- [18] L. Huang, Q.H. Chang, G.L. Guo, Y. Liu, Y.Q. Xie, T. Wang, B. Ling, H.F. Yang, Synthesis of high-quality graphene films on nickel foils by rapid thermal chemical vapor deposition, *Carbon.* 50 (2012) 551–556.
<https://doi.org/10.1016/j.carbon.2011.09.012>.
- [19] X. Hu, Y. Zhang, H. Ago, H. Zhou, X. Li, L. Fan, B. Cai, X. Li, M. Zhong, K. Wang, D. Wu, H. Zhu, Ultra-fast synthesis of graphene by melt spinning, *Carbon.* 61 (2013) 299–304. <https://doi.org/10.1016/j.carbon.2013.05.008>.
- [20] E.H. Strange, C.A. Pim, Process of manufacturing thin sheets, foil, strips, or ribbons of zinc, lead, or other metal or alloy., US905758A, 1908.
<https://patents.google.com/patent/US905758A/en> (accessed February 7, 2021).
- [21] H. Liebermann, C. Graham, Production of amorphous alloy ribbons and effects of apparatus parameters on ribbon dimensions, *IEEE Trans. Magn.* 12 (1976) 921–923. <https://doi.org/10.1109/TMAG.1976.1059201>.
- [22] B. Cantor, W.T. Kim, B.P. Bewlay, A.G. Gillen, Microstructure - cooling rate correlations in melt-spun alloys, *J. Mater. Sci.* 26 (1991) 1266–1276.
<https://doi.org/10.1007/BF00544465>.
- [23] G. Lojen, I. Anžel, A. Kneissl, A. Križman, E. Unterweger, B. Kosec, M. Bizjak, Microstructure of rapidly solidified Cu–Al–Ni shape memory alloy ribbons, *J. Mater. Process. Technol.* 162 (2005) 220–229.
<https://doi.org/10.1016/j.jmatprotec.2005.02.196>.
- [24] C.T. Hu, T. Goryczka, D. Vokoun, Effects of the spinning wheel velocity on the microstructure of Fe–Pd shape memory melt-spun ribbons, *Scr. Mater.* 50 (2004) 539–542. <https://doi.org/10.1016/j.scriptamat.2003.10.026>.

- [25] R.C. Budhani, T.C. Goel, K.L. Chopra, Melt-spinning technique for preparation of metallic glasses, *Bull. Mater. Sci.* 4 (1982) 549–561.
<https://doi.org/10.1007/BF02824962>.
- [26] M.J. Kramer, H. Mecco, K.W. Dennis, E. Vargonova, R.W. McCallum, R.E. Napolitano, Rapid solidification and metallic glass formation – Experimental and theoretical limits, *J. Non. Cryst. Solids.* 353 (2007) 3633–3639.
<https://doi.org/10.1016/j.jnoncrysol.2007.05.172>.
- [27] H.H. Liebermann, The dependence of the geometry of glassy alloy ribbons on the chill block melt-spinning process parameters, *Mater. Sci. Eng.* 43 (1980) 203–210.
[https://doi.org/10.1016/0025-5416\(80\)90103-2](https://doi.org/10.1016/0025-5416(80)90103-2).
- [28] R.E. Maringer, Solidification on a substrate, *Mater. Sci. Eng.* 98 (1988) 13–20.
[https://doi.org/10.1016/0025-5416\(88\)90117-6](https://doi.org/10.1016/0025-5416(88)90117-6).
- [29] R.C. Ruhl, Cooling rates in splat cooling, *Mater. Sci. Eng.* 1 (1967) 313–320.
[https://doi.org/10.1016/0025-5416\(67\)90013-4](https://doi.org/10.1016/0025-5416(67)90013-4).
- [30] H. Jones, The status of rapid solidification of alloys in research and application, *J. Mater. Sci.* 19 (1984) 1043–1076. <https://doi.org/10.1007/BF01120015>.
- [31] H.H. Liebermann, Rapidly solidified alloys made by chill block melt-spinning processes, *J. Cryst. Growth.* 70 (1984) 497–506. [https://doi.org/10.1016/0022-0248\(84\)90308-7](https://doi.org/10.1016/0022-0248(84)90308-7).
- [32] W. Löser, O. Shuleshova, Nucleation and Solidification Kinetics of Metastable Phases in Undercooled Melts, in: D.M. Herlach and D.M. Matson (Ed.), *Solidification of Containerless Undercooled Melts*, Wiley, Weinheim, Germany, 2012: pp. 187–212. <https://doi.org/10.1002/9783527647903.ch9>.
- [33] V.I. Tkatch, A.I. Limanovskii, S.N. Denisenko, S.G. Rassolov, The effect of the melt-spinning processing parameters on the rate of cooling, *Mater. Sci. Eng. A.* 323 (2002) 91–96. [https://doi.org/10.1016/S0921-5093\(01\)01346-6](https://doi.org/10.1016/S0921-5093(01)01346-6).

- [34] A.G. Gillen, B. Cantor, Photocalorimetric cooling rate measurements on a Ni-5 wt% Al alloy rapidly solidified by melt spinning, *Acta Metall.* 33 (1985) 1813–1825. [https://doi.org/10.1016/0001-6160\(85\)90005-7](https://doi.org/10.1016/0001-6160(85)90005-7).
- [35] I.M. Lifshitz, V. V. Slyozov, The kinetics of precipitation from supersaturated solid solutions, *J. Phys. Chem. Solids.* 19 (1961) 35–50. [https://doi.org/10.1016/0022-3697\(61\)90054-3](https://doi.org/10.1016/0022-3697(61)90054-3).
- [36] C. Wagner, Theorie der Alterung von Niederschlägen durch Umlösen (Ostwald-Reifung), *Zeitschrift Für Elektrochemie, Berichte Der Bunsengesellschaft Für Phys. Chemie.* 65 (1961) 581–591. <https://doi.org/10.1002/BBPC.19610650704>.
- [37] H. Lee, Seung Zeon Han, Hyuck Mo Lee, Z.H. Lee, Coarsening behavior of L12 precipitates in melt-spun AlTiVZr alloys, *Mater. Sci. Eng. A.* 163 (1993) 81–90. [https://doi.org/10.1016/0921-5093\(93\)90581-X](https://doi.org/10.1016/0921-5093(93)90581-X).
- [38] Z. Cai, C. Zhang, R. Wang, C. Peng, K. Qiu, N. Wang, Effect of solidification rate on the coarsening behavior of precipitate in rapidly solidified Al-Si alloy, *Prog. Nat. Sci. Mater. Int.* 26 (2016) 391–397. <https://doi.org/10.1016/j.pnsc.2016.08.002>.
- [39] C.H. Tsau, Y.C. Chen, The coarsening of the precipitates in melt-spun Al-Ti-Zr ribbons, *Mater. Chem. Phys.* 73 (2002) 111–117. [https://doi.org/10.1016/S0254-0584\(01\)00363-7](https://doi.org/10.1016/S0254-0584(01)00363-7).
- [40] Y.Y. Zhao, H.W. Chen, Z.P. Lu, T.G. Nieh, Thermal stability and coarsening of coherent particles in a precipitation-hardened (NiCoFeCr)₉₄Ti₂Al₄ high-entropy alloy, *Acta Mater.* 147 (2018) 184–194. <https://doi.org/10.1016/j.actamat.2018.01.049>.
- [41] A. Baldan, Review Progress in Ostwald ripening theories and their applications to the γ -precipitates in nickel-base superalloys Part II Nickel-base superalloys, *J. Mater. Sci.* 37 (2002) 2379–2405. <https://doi.org/https://doi.org/10.1023/A:1015408116016>.

- [42] E.A. Brandes, G.B. Brook, eds., *Smithells Metals Reference Book - 7th Edition*, 2013. <https://www.elsevier.com/books/smithells-metals-reference-book/brandes/978-0-08-051730-8> (accessed December 2, 2020).
- [43] R.S. Weatherup, C. Baecht, B. Dlubak, B.C. Bayer, P.R. Kidambi, R. Blume, R. Schloegl, S. Hofmann, Introducing Carbon Diffusion Barriers for Uniform, High-Quality Graphene Growth from Solid Sources, *Nano Lett.* 13 (2013) 4264–4631. <https://doi.org/10.1021/nl401601x>.

4 Microstructural Evolution of Freestanding Carbon from Rapidly Solidified Nickel-Carbon Ribbon

4.1 Summary

We report the chemical and structural transformations of freestanding carbon excavated from melt spun nickel-carbon ribbon by chemical dissolution of the metal in acid. We found that the microstructure of carbon precipitated from the rapidly quenched ribbon could be tuned by varying the carbon content from 4 – 12 at. % in the precursor and annealing the ribbon at temperatures that ranged from 400 – 1200 °C. Via the step-wise variation of these two parameters, we sequentially transformed amorphous carbon nanospheres with a high BET surface area of 203.4 m²/g into thick, highly crystalline flakes of graphite that conformed to the shape of the as-spun ribbon.

4.2 Introduction

In the previous chapter, we reported the ability to melt spin nickel-carbon alloys with a carbon fraction up to 12 at. % using a water-cooled copper roller rotating at speeds between 40 to 80 m/s. We also examined the precipitation kinetics of carbon within rapidly solidified nickel-carbon ribbons. In this chapter, we present a study of the morphological and chemical transformation of the freestanding carbon that is produced when the Ni from melt spun ribbon is dissolved in acid. A variety of carbon morphologies can be produced by varying the initial carbon content and annealing temperature. Depending on processing conditions, carbon excavated from as-spun Ni-C ribbon was found to contain amorphous nanospheres. By increasing the carbon content in the precursor and performing heat treatments on the ribbon after melt spinning, we

achieved multiple and step-wise conversions of the carbon microstructure to acquire highly crystalline, thick flakes of graphite whose dimensions matched that of the precursor ribbons.

4.3 Experimental Methods

The methods of alloy preparation, melt spinning, and thermal annealing of melt spun ribbon are described in Chapter 3.3.

4.3.1 Dissolution of metal phase to excavate carbon material

Metal-carbon ribbons were immersed in 5 M HCl solution at room temperature to remove the metal phase and excavate carbon in the ribbon. The acid was filtered off using a Millipore filter (pore size 1 μm) and the remaining carbon material was washed with deionized water until neutral. Carbon samples were dispersed in water via sonication and drop cast onto grids in preparation for TEM imaging. Carbon materials were also characterized using SEM, EDS, and Raman spectroscopy.

4.3.2 Characterization tools

SEM imaging was performed using a Thermo Scientific Helios G4 UC Focused Ion Beam/ Scanning Electron Microscope (FIBSEM) instrument equipped with an energy dispersive spectroscopy (EDS) detector which was used for compositional analysis. Carbon samples were also imaged using the Thermo Scientific TF30 Transmission Electron Microscope (TEM). Raman spectroscopy was carried out using a Horiba LabRam Evolution Raman microscope with a 532 nm laser line and a 100 μm spot size. 3-point BET surface area measurements were performed commercially using a Micrometrics TriStar II 3020 instrument.

4.4 Results and Discussion

4.4.1 The microstructural evolution of freestanding carbon

Here we focus on the structure of the carbon materials excavated from nickel-carbon alloys by chemical dissolution of the metal in hydrochloric acid. Figure 4-1 summarizes the evolution of the carbon microstructure as a function of annealing temperature and the carbon content in the precursor ribbon. Carbon obtained from as-spun Ni-C ribbon with a low carbon content exists as amorphous spheres. By increasing the ribbon annealing temperature, the morphology of the freestanding carbon transformed into high aspect carbon flakes. Figure 4-1 also shows that increasing the carbon content in the precursor ribbon is correlated with a conversion of the morphologies from nanospheres to flakes. By varying these two parameters, we can incrementally transform the microstructure of carbon synthesized by melt spinning Ni-C alloys. The mechanisms of these transformations are discussed in further detail in the subsequent sections.

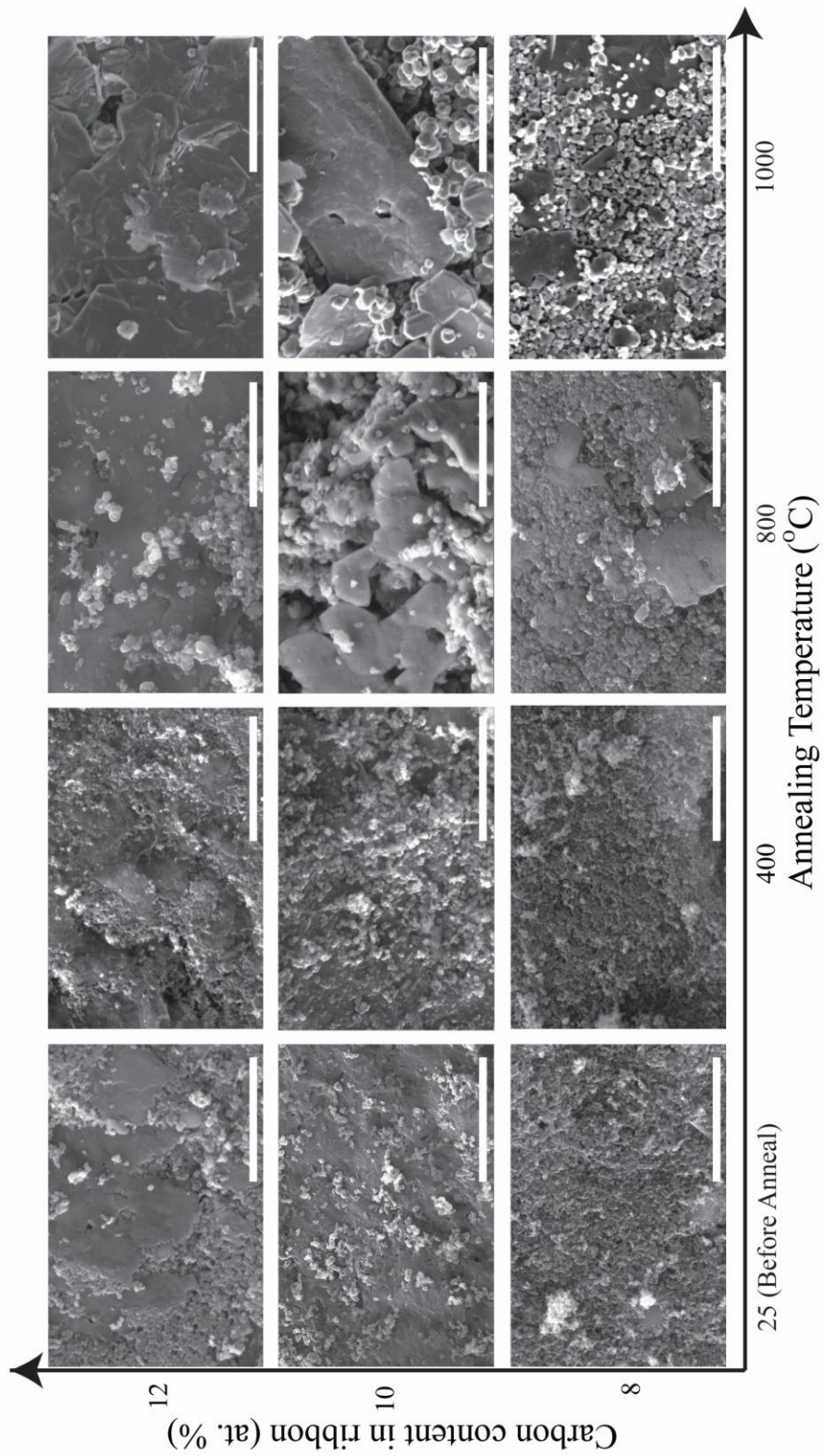


Figure 4-1. Microstructural variation of carbon excavated from melt-spun ribbon annealed at different temperatures with varying precursor carbon contents. Scale bars are 4 μm .

4.4.2 Microstructure of precursor carbon material

The structure of the commercially acquired graphite used in the precursor alloy was thick multi-layer flakes. This material was converted into spheroids and flakes when excavated from a nickel-carbon ingot prepared by induction melting and conventional cooling - structures that are typical of graphite precipitated from metallic melts. The transformation is shown in Figure 4-2 [1,2].

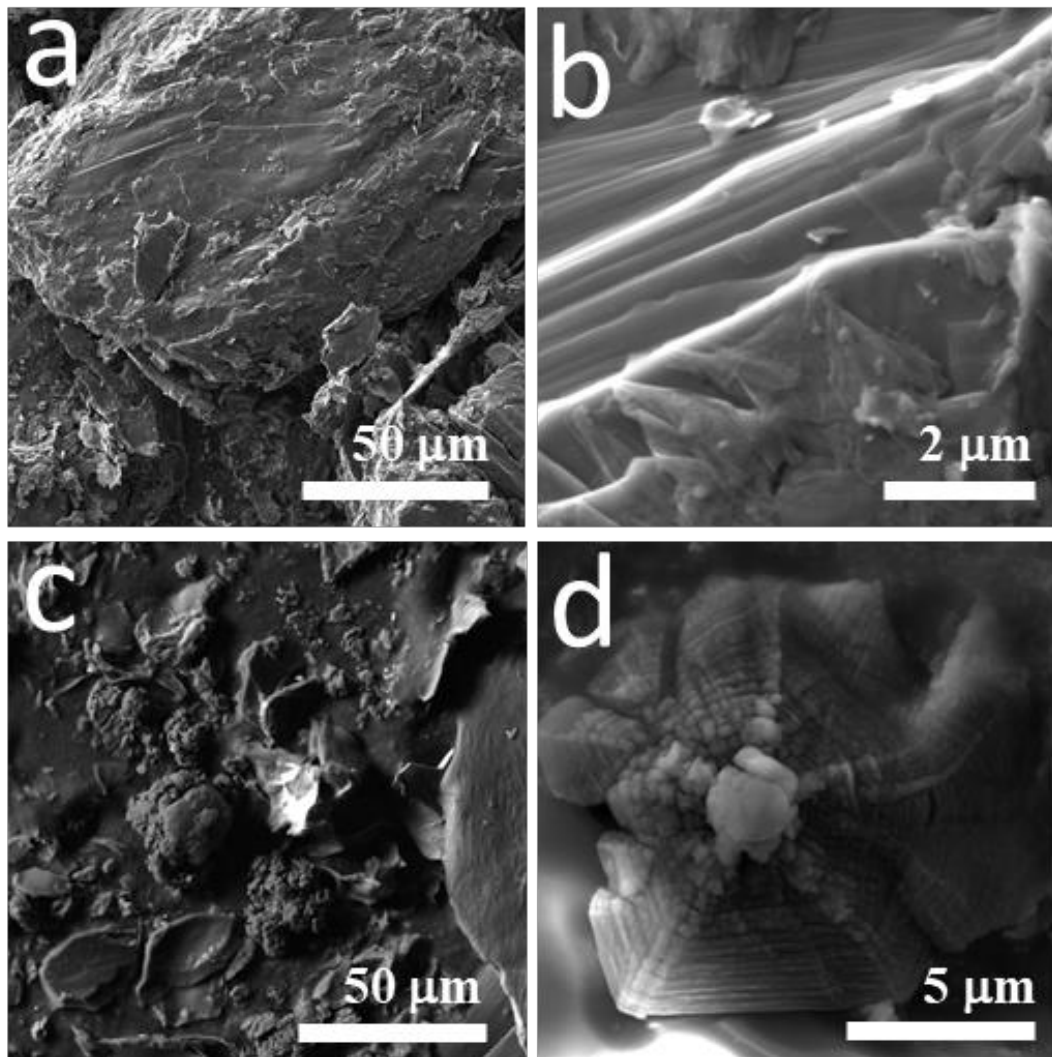


Figure 4-2. (Top) (a) and (b) Commercially prepared graphite used to prepare precursor Ni-C ingots for melt-spinning; (Bottom) (c) and (d) Carbon flakes and spheroids collected by chemical dissolution of Ni from Ni-C ingots prepared by induction melting.

4.4.3 Microstructure of carbon excavated from as-spun ribbon

Figure 4-3 shows the SEM micrographs of carbon obtained by the chemical etching of the Ni phase from as-prepared Ni_{92}C_8 melt-spun ribbon, i.e., without annealing. The most prevalent microstructure observed were sub-micron sized nodules that either existed as separate nanoparticles or a more complex morphology consisting of clusters of interconnected particles. The particle sizes are on the same order of magnitude as the precipitates found embedded in the nickel grain boundaries, so it is likely that is one location from which they originated. However, because the grain boundary precipitates cannot account for the quantity of carbon excavated in this case, it is reasonable to assume that another source of the nanospheres was carbon dissolved in the Ni bulk.

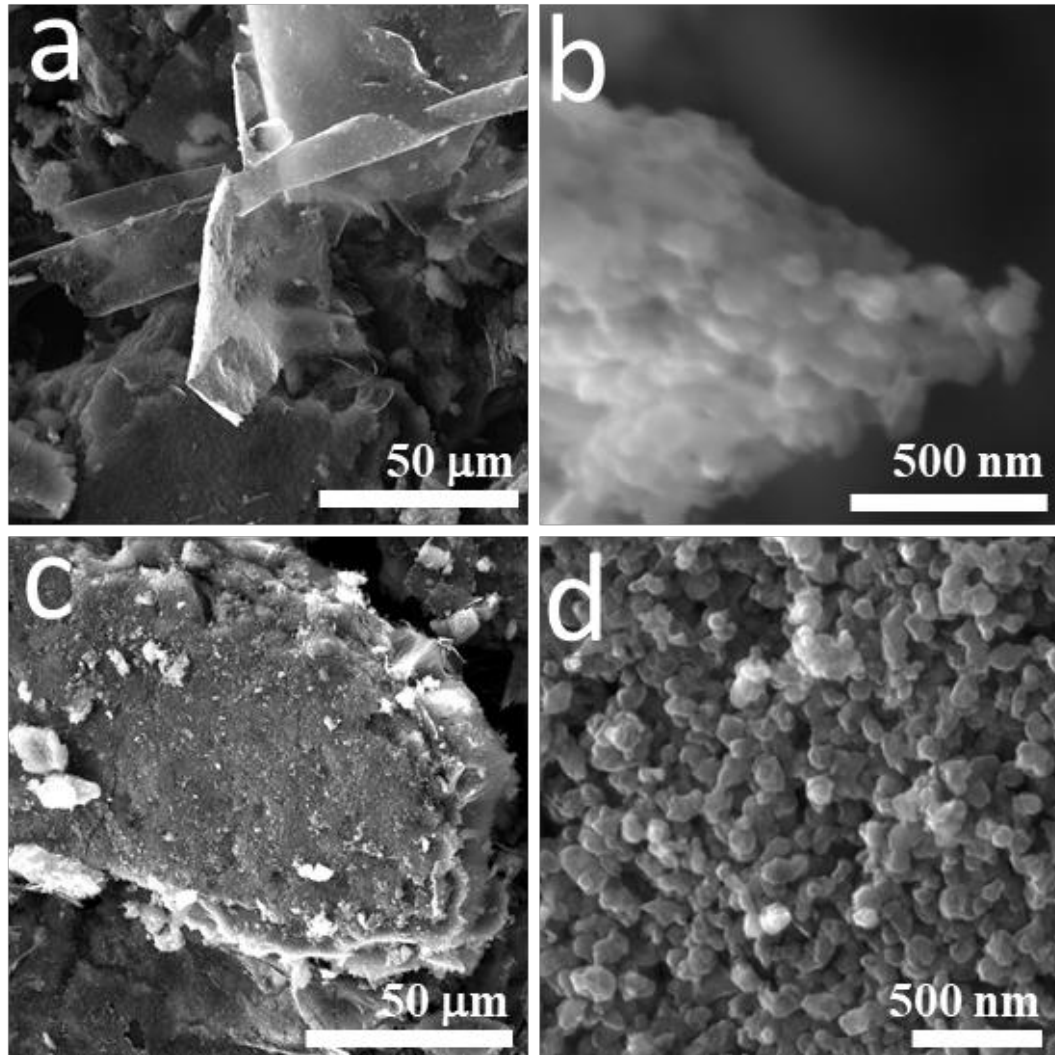


Figure 4-3. Carbon etched from Ni_{92}C_8 melt-spun ribbon before annealing showing two types of morphologies (a) Thin carbon flake comprised of clusters of nanometer sized carbon particles. (b) The structure shown in (a) is magnified. (c) A large carbon “slab” that is 10 μm thick and over 100 μm long. (d) At higher magnification, the slab is observed to be comprised of clusters of interconnected submicron sized particles.

Also observed, but in lesser quantities, were thin flakes that were electron transparent to 15 kV. Since no plate-like structures were present within the cross-section of melt-spun ribbon, we postulate that observed carbon sheet precipitated at the ribbon surface, a finding that corroborates the results found by Hu et al. that graphene grows on

the surfaces of melt spun ribbon [3]. Moreover, owing to the high processing temperature used to melt the nickel-carbon alloy during melt spinning ($> 1500\text{ }^{\circ}\text{C}$) and the presence of precipitates embedded in the melt spun ribbon, the mechanism of graphene growth is most consistent with the dissolution-precipitation process observed in CVD and precipitation on the surface of a metallic melt.

Raman spectroscopy was utilized to analyze the crystallinity of the fabricated material. The ratio of intensity of the D band to the G band, $I(D)/I(G)$, provides information on the defect concentration and crystallize size in disordered graphite and on the size of aromatic clusters in amorphous carbon [3 - 6]. The carbon from as-spun ribbon exhibited characteristic features of amorphous carbon: broad G and D peaks and a low 2D band intensity. The high $I(D)/I(G)$ ratio of 0.9 is indicative of large aromatic clusters. The TEM micrograph shown in Figure 4-4 shows a comparison of carbon excavated from as-spun and annealed Ni_{92}C_8 ribbon. The top images show that the carbon nanoparticles etched from unannealed ribbon are $\sim 100\text{ nm}$ in diameter and also confirm the low degree of crystallinity of carbon. The growth morphology attained under these experimental conditions most closely resembles carbon black or nano-graphite. In fact, the BET surface area for carbon obtained from as-spun (before annealing) rapidly solidified Ni_{92}C_8 ribbon was measured to be $203.4\text{ m}^2/\text{g}$, a value comparable to commercially prepared carbon blacks [7].

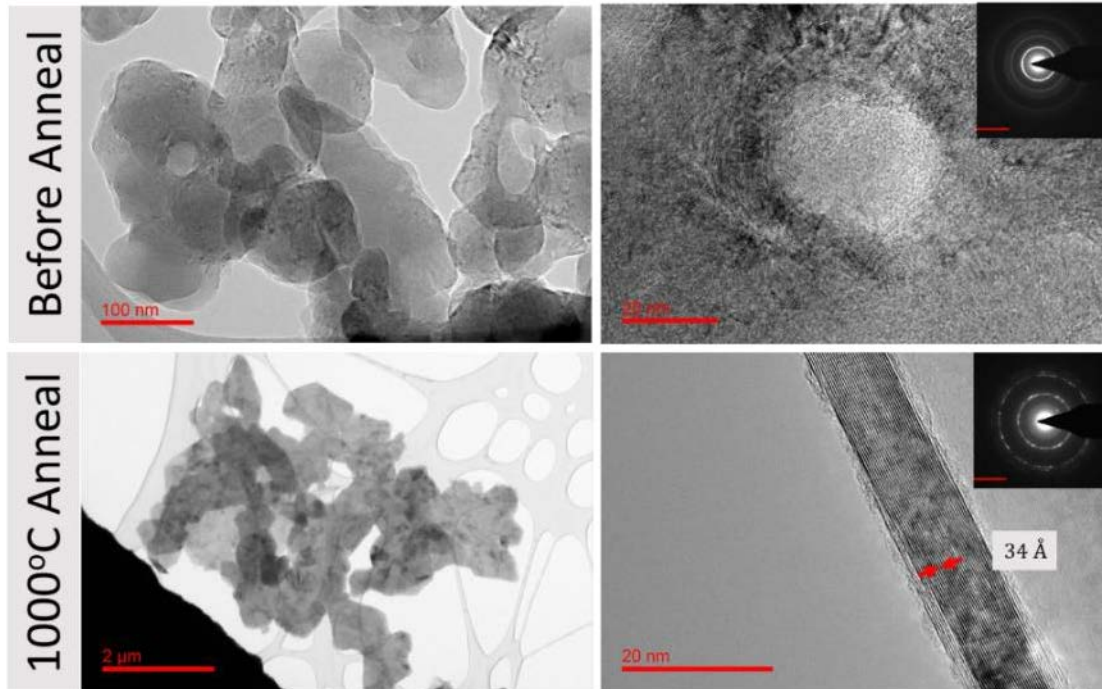


Figure 4-4. TEM micrographs of carbon from Ni_{92}C_8 ribbon before annealing showing amorphous sub-micron polygonal carbon spheres (top). After annealing at 1000 °C for one hour, the carbon particles became sized on the order of microns and exhibited a high degree of graphitic crystallinity (bottom).

Increasing the carbon content in the ribbon resulted in an increased thickness of the graphite flakes; the growth front of graphene layers can clearly be identified on the surface, as shown in Figure 4-5(a). This observation indicates that controlling the carbon content of the precursor alloy may allow us to tune the number of layers of graphene produced, consistent with Hu's observations [8].

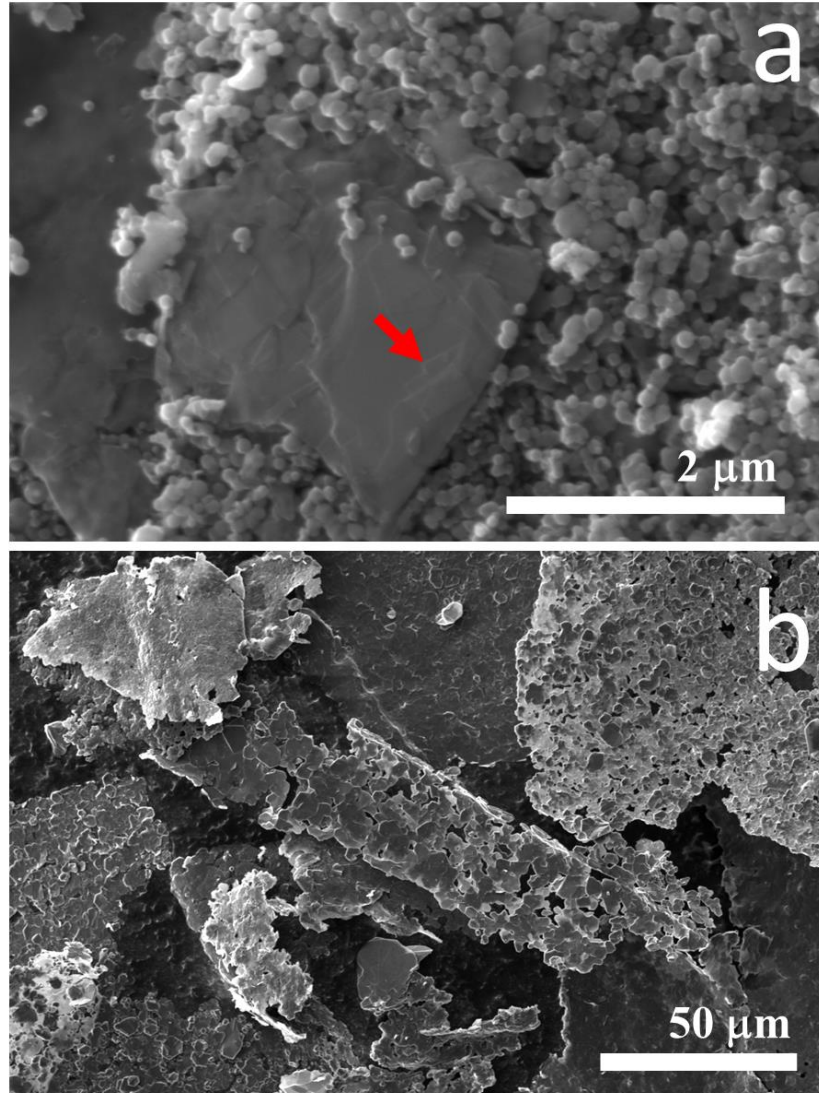


Figure 4-5. (a) Carbon from $\text{Ni}_{88}\text{C}_{12}$ melt spun ribbon before annealing showing growth front of graphene layers; (b) Carbon from Ni_{92}C_8 ribbon annealed at 1200 °C exhibiting the structure of Kish graphite.

4.4.4 Microstructure of carbon from excavated from annealed ribbon

The resultant microstructure of carbon embedded in the Ni matrix after ribbon annealing was shown in Figure 3-4; the TEM micrograph highlighted the polygonal outline of the graphite crystals, signaling the crystallization of carbon within the grains due to thermal treatment at 1000 °C. Additionally, annealing nickel-carbon ribbon promoted the precipitation of graphite on the ribbon free surfaces, as depicted in Figure

4-6, where the plan view of Ni_{92}C_8 ribbon before and after annealing at 1000 °C is shown. This observation is consistent with a reduction in the density of carbon precipitates that speckle the interior of the ribbon, as well as the reduced quantity of nanospheres fabricated by excavating carbon from the ribbon. Instead, increasing the annealing temperature of the ribbon resulted in an increase in the prevalence of the high aspect ratio graphite flakes retrieved after etching the Ni matrix. Increasing the initial carbon content in the ribbon also led to the same observation: the samples that contained the highest atomic fraction of carbon ($\text{Ni}_{88}\text{C}_{12}$) and were annealed at 1000 °C for 1 hour produced carbon materials consisting of large graphite flakes, hundreds of microns wide (equal to the width of the ribbon) and about 1 μm thick, and almost devoid of spherical nodules. Interestingly, Ni_{92}C_8 ribbon at 1200 °C, shown in Figure 4-5(b), exhibited the foliated dendrite structure characteristic of Kish graphite, providing further confirmation that C segregates to the solid Ni surface at high temperatures, as it does in liquid Ni.

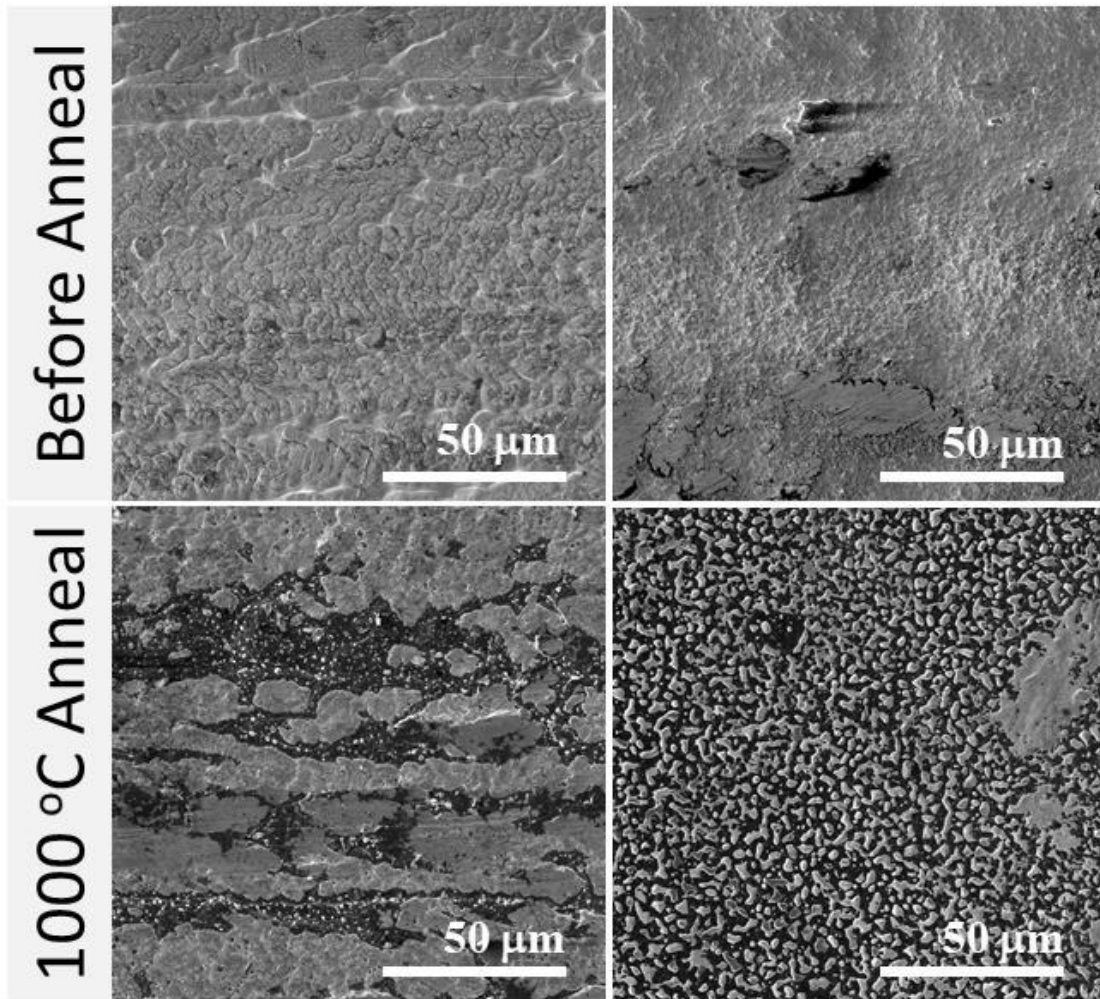


Figure 4-6. Plan view of (top) as-spun $\text{Ni}_{88}\text{C}_{12}$ ribbon and (bottom) $\text{Ni}_{88}\text{C}_{12}$ ribbon annealed at 1000 °C for 1 hour, showing the growth of carbon (black regions) on the surface post heat-treatment. The carbon appears to grow in two forms on the ribbon surface: (left) as striations through the Ni ribbon and (right) as a layer interspersed with Ni particles embedded in the surface.

Raman characterization of the freestanding carbon microstructure as a function of ribbon annealing temperature is shown in Figure 4-7. Table I also outlines the effect of annealing on the Raman spectra of carbon obtained from melt spun ribbon. Annealing at 400 °C has little effect on increasing the crystallinity of the carbon material compared to the sample that was not annealed, consistent with other reports that 400 °C is too low of a temperature to initiate significant graphitization [9]. However, corresponding to the

increase in annealing temperature, the $I(D)/I(G)$ ratio decreased from 0.9 for carbon annealed at 400 °C to 0.3 for carbon annealed at 1000 °C, indicating that the thermal treatments resulted in a reduction in defect density, increase in crystallite size, and ultimately, enhanced graphitization of the material. The $I(2D)/I(G)$ ratio also increased from 0.31 to 0.65, signaling a resultant increase in the number of graphene layers present in the material. Similar transformations of carbon from amorphous to crystalline by increasing the annealing temperature have been well documented in the literature [10-13]. The TEM micrograph in Figure 11 also shows the development of crystallinity in the material after annealing at 1000 °C where the annealed carbon exhibited a d-spacing of 0.34 nm, which is consistent with the expected value of the interlayer spacing of graphite [14].

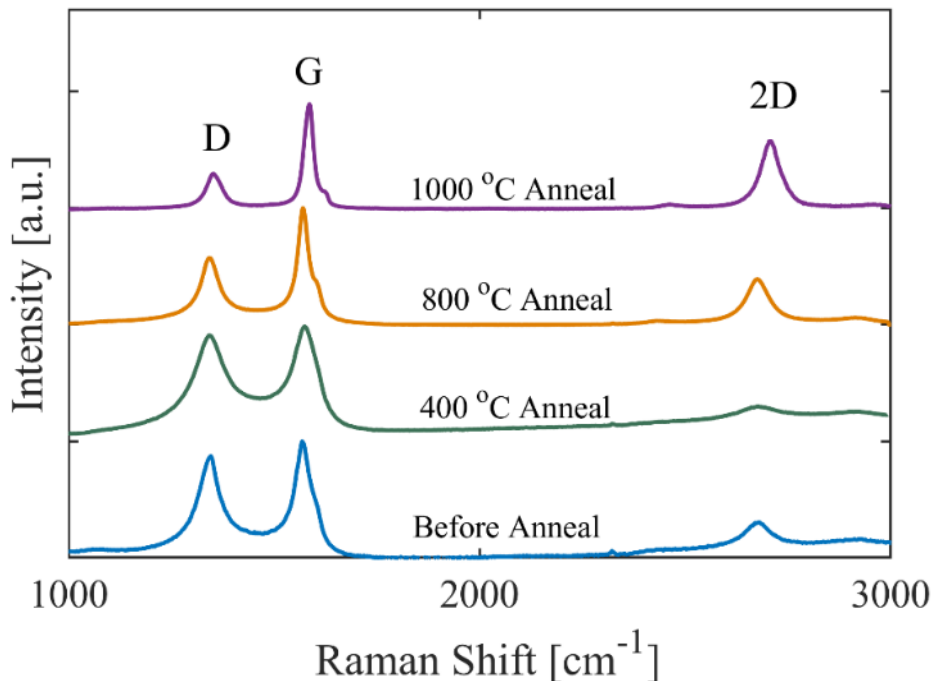


Figure 4-7. Raman spectra showing increasing graphitization of carbon with increasing annealing temperatures.

Table 4-1. Summary of Raman spectrum properties of freestanding carbon etched from melt spun Ni₉₂C₈ ribbon annealed at different temperatures.

| | Before Anneal | 400 °C Anneal | 800 °C Anneal | 1000 °C Anneal |
|----------------------------|---------------|---------------|---------------|----------------|
| G peak (cm ⁻¹) | 1569 | 1577 | 1571 | 1578 |
| I(D)/I(G) | 0.88 | 0.92 | 0.57 | 0.34 |
| I(2D)/I(G) | 0.31 | 0.31 | 0.39 | 0.65 |

We postulate that supersaturation of the Ni lattice leads to carbon atoms being dispersed throughout the metal's interstitial sites. When the rapidly solidified ribbon is immersed in acid and the carbon is liberated, there is little time and driving force to induce graphitization. As a result, the carbon lacks crystallinity and evolves as sub-micron sized nodules – approximately the same shape and size as they were in the ribbon – where the amorphous spheres appeared brighter in the SEM micrograph. Annealing, however, allows for carbon diffusion, which led to growth and graphitization of flakes on the free surfaces of the ribbon.

It is interesting to consider the utility of the carbon materials fabricated here in the context of carbon fiber manufacture. Carbon fiber usually consists of graphitic crystal threads a few microns in diameter, with a microstructure in which the graphene planes are aligned parallel to the axis of each thread so that the strong direction is along the axis of the thread. Nominally, the microstructure of carbons produced here is similar – microns-wide graphite sheets oriented with the strong axis in the plane of the ribbon. Although the length of the flakes produced here is much shorter than those in carbon fiber, it is easy to imagine that directional precipitation and crystal growth can be induced if the ribbons were to be pulled through a hot zone rather than homogeneously annealed,

and this should lead to very long graphite crystals. Assuming these may be spun into fiber with a suitable binder (we have not produced enough material to perform this test), this approach may be a more benign method to produce carbon fiber precursors from a life-cycle approach, as it is well-known that carbon fiber produced from polymeric precursors is an energy and resource intensive process, leading to significant emissions during the oxidation and graphitization cycles at high temperature [15].

4.5 Conclusions

We report the ability to melt spin nickel-carbon alloys with a carbon fraction up to 12 at. % using a water-cooled copper roller rotating at speeds between 40 to 80 m/s. From the rapidly solidified ribbon, carbon was excavated via chemical dissolution of the metal to reveal freestanding carbon materials. We evaluated changes in carbon microstructure as a function of precursor carbon content and annealing the Ni-C ribbon. We observed that the morphology of the carbon materials could be adjusted sequentially by varying these two experimental parameters. As-spun ribbon (undergoing no heat treatment) with a low carbon content will lead to the formation of high surface area amorphous carbon nanospheres and single or few-layer graphene. By increasing the carbon content and/or the annealing temperature, the quantity of nanospheres was decreased and replaced by graphite flakes. The thickness and crystallinity of these flakes can also be controlled by these experimental variables. After a high temperature heat treatment at 1000 °C, Ni₈₈C₁₂ ribbon produced thick graphite flakes from carbon material precipitated on the surfaces of the ribbon.

4.6 References

- [1] D.M. Stefanescu, G. Alonso, P. Larrañaga, E. De la Fuente, R. Suarez, On the crystallization of graphite from liquid iron–carbon–silicon melts, *Acta Mater.* 107 (2016) 102–126. <https://doi.org/10.1016/J.ACTAMAT.2016.01.047>.
- [2] S. Amini, H. Kalaantari, J. Garay, A.A. Balandin, R. Abbaschian, Growth of graphene and graphite nanocrystals from a molten phase, *J. Mater. Sci.* 46 (2011) 6255–6263. <https://doi.org/10.1007/s10853-011-5432-9>.
- [3] M.A. Pimenta, G. Dresselhaus, M.S. Dresselhaus, L.G. Cançado, A. Jorio, R. Saito, Studying disorder in graphite-based systems by Raman spectroscopy, *Phys. Chem. Chem. Phys.* 9 (2007) 1276–1290. <https://doi.org/10.1039/B613962K>.
- [4] M.S. Dresselhaus, A. Jorio, R. Saito, Characterizing Graphene, Graphite, and Carbon Nanotubes by Raman Spectroscopy, *Annu. Rev. Condens. Matter Phys.* 1 (2010) 89–108. <https://doi.org/10.1146/annurev-conmatphys-070909-103919>.
- [5] A.C. Ferrari, J. Robertson, Interpretation of Raman spectra of disordered and amorphous carbon, American Physical Society, 2000. <https://doi.org/10.1103/PhysRevB.61.14095>.
- [6] A.C. Ferrari, J.C. Meyer, V. Scardaci, C. Casiraghi, M. Lazzeri, F. Mauri, S. Piscanec, D. Jiang, K.S. Novoselov, S. Roth, A.K. Geim, Raman spectrum of graphene and graphene layers, *Phys. Rev. Lett.* 97 (2006) 187401. <https://doi.org/10.1103/PhysRevLett.97.187401>.
- [7] J.H. Atkins, Porosity and surface area of carbon black, *Carbon.* 3 (1965) 299–303. [https://doi.org/10.1016/0008-6223\(65\)90064-3](https://doi.org/10.1016/0008-6223(65)90064-3).
- [8] X. Hu, Y. Zhang, H. Ago, H. Zhou, X. Li, L. Fan, B. Cai, X. Li, M. Zhong, K. Wang, D. Wu, H. Zhu, Ultra-fast synthesis of graphene by melt spinning, *Carbon.* 61 (2013) 299–304. <https://doi.org/10.1016/j.carbon.2013.05.008>.

- [9] H. Li, X. Li, J. Wei, Z. Wang, P. Guo, P. Ke, H. Saito, P. Cui, A. Wang, Crystalline transformation from ta-C to graphene induced by a catalytic Ni layer during annealing, *Diam. Relat. Mater.* 101 (2020) 107556. <https://doi.org/10.1016/j.diamond.2019.107556>.
- [10] R.S. Weatherup, C. Baetz, B. Dlubak, B.C. Bayer, P.R. Kidambi, R. Blume, R. Schloegl, S. Hofmann, Introducing Carbon Diffusion Barriers for Uniform, High-Quality Graphene Growth from Solid Sources, *Nano Lett.* 13 (2013) 4264–4631. <https://doi.org/10.1021/nl401601x>.
- [11] M. Pawlyta, J.N. Rouzaud, S. Duber, Raman microspectroscopy characterization of carbon blacks: Spectral analysis and structural information, *Carbon.* 84 (2015) 479–490. <https://doi.org/10.1016/j.carbon.2014.12.030>.
- [12] G. Greenidge, J. Erlebacher, Porous graphite fabricated by liquid metal dealloying of silicon carbide, *Carbon.* 165 (2020) 45–54. <https://doi.org/10.1016/j.carbon.2020.04.028>.
- [13] S.-G. Yu, K. Yubuta, T. Wada, H. Kato, Three-dimensional bicontinuous porous graphite generated in low temperature metallic liquid, *Carbon.* 96 (2016) 403–410. <https://doi.org/10.1016/j.carbon.2015.09.093>.
- [14] Y. Gamo, A. Nagashima, M. Wakabayashi, M. Terai, C. Oshima, Atomic structure of monolayer graphite formed on Ni(111), *Surf. Sci.* 374 (1997) 61–64. [https://doi.org/10.1016/S0039-6028\(96\)00785-6](https://doi.org/10.1016/S0039-6028(96)00785-6).
- [15] S. Das, Life cycle assessment of carbon fiber-reinforced polymer composites, *Int. J. Life Cycle Assess.* 16 (2011), 268-282. <https://doi.org/10.1007/s11367-011-0264-z>

5 Amorphous Carbon Foam Fabricated by Melt Spinning Iron-Carbon Alloys

5.1 Summary

In this work, we report a novel and facile technique to produce a carbon foam with a honeycomb lattice architecture and uniform pore size. Melt spinning was used to fabricate rapidly solidified iron-carbon ribbon, from which the iron was removed via chemical dissolution to produce a freestanding carbon monolith. The resulting material from as-spun ribbon was freestanding carbon foam with hierarchical porosity; the sizes of the cells ranged from 2 – 5 μm , but the carbon walls that enclosed the cells contained nanometer sized pores. Annealing resulted in the disappearance of the submicron sized pores, but the open cell pore size remained unchanged by thermal treatment. Raman spectroscopy and TEM analysis revealed that the material consisted of amorphous carbon even after annealing and the BET surface area of the material was 4.5 m^2/g .

5.2 Introduction

Three-dimensional porous carbon architectures exhibit desirable electrochemical, mechanical and microstructural properties that make such materials attractive candidates for use in a variety of applications: water decontamination and oil/water separation [1], water desalination [2], anode materials in sodium-ion batteries [3], cathodes in lithium ion batteries [4], electromagnetic interference shielding [5] and scaffolds for neural stem cells [6].

Carbon foams, in particular, often exhibit a honeycomb pore structure, where the pores (or cells) are enclosed by carbon walls that are interconnected via struts [7]. There

are several reported fabrication methods of carbon foams; each route can produce pores of varying sizes that range from 100 nm to 1000 μm [3,7]. The direct drying of graphene oxide (GO) hydrogels is an example of a process to prepare graphene foams [8]. The GO is first prepared via the modified Hummer's method. An aqueous suspension of GO nanosheets is then freeze-dried to form GO foams which are then subjected to high temperatures in a dry inert atmosphere to reduce material; the result is a foam made of graphene. Carbon sponges have also been prepared by chemical vapor deposition (CVD) where, for example, CH_4 gas was decomposed on a nickel foam template at 1050 $^\circ\text{C}$ and cooled slowly, facilitating precipitation of graphite on the Ni walls [4]. The nickel was then chemically etched in acid to liberate the freestanding carbon foam.

In this work, we report a novel and facile method to synthesize a porous carbon material with a honeycomb lattice structure. Melt spinning was used to fabricate rapidly solidified iron-carbon ribbon, from which the iron was removed via chemical dissolution. The resulting material from as-spun ribbon was a freestanding carbon foam with hierarchical porosity; the sizes of the cells ranged from 2 – 5 μm , but the carbon walls that enclosed that the cells contained nanometer sized pores. When the melt-spun ribbon underwent heat treatment, the smaller pores consolidated to produce a porous carbon monolith with a honeycomb structure. Raman spectroscopy and TEM analysis revealed that the material consisted of amorphous carbon even after annealing and the BET surface area of the material was 4.5 m^2/g .

5.3 Experimental Methods

5.3.1 Alloy Preparation

Ingots of iron-carbon alloys (20 g) containing 83 at.% Fe (99.5 wt. % from Kurt J. Lesker) and 17 at. % graphite (99.995 wt. % from Sigma Aldrich) were prepared by inductively melting the constituents in a water-cooled copper crucible using a 45 kW Ambrell Ekoheat ES induction system under a flowing Ar atmosphere.

5.3.2 Melt Spinning

The components of the melt spinner (Arcast Inc.) are shown in Figure 3-1 and are enclosed in a stainless steel vacuum chamber. The equipment consists of (i) a combat-grade boron nitride crucible with a 3/64" diameter nozzle that was machined in-house (the crucible head was replaced every three runs or when the nozzle was abraded beyond repair), (ii) RF induction coils, and (iii) the copper wheel (300 mm diameter and 50 mm wide) that was water-cooled to 13 °C during experiments, and (iv) a collection tube for the ribbon.

In a typical experiment, an approximately 20 g alloy ingot charge was inserted into the crucible, the chamber was evacuated and backfilled with purified argon to -10 psig. The charge was melted via RF induction heating using a 15 kW power supply and the temperature was monitored using a Dias Pyrospot DS 56 N pyrometer. The crucible was then lowered to a preset distance (about 1 mm) above the rotating wheel and the molten alloy was ejected via pressurized argon. The jet forms a melt pool on the cold copper surface and solidifies into a brittle ribbon that is typically only a few centimeters in length, ~1-3 mm in width and a thickness in the range of 20 – 50 μm . The wheel rotation

rate used was 3000 rpm. Typically, the entire 20 g ingot was converted to ribbon in under 5 seconds.



Figure 5-1. Photograph of melt-spun iron-carbon ribbon

Ribbon microstructures, plan view and cross-section, were investigated using Scanning Electron Microscopy (SEM) and Transmission Electron Microscopy (TEM). Composition analysis was performed using Energy Dispersive Spectroscopy (EDS) and phase analysis was conducted via X-ray Diffraction (XRD). The wheel was prepared between each run by polishing with silicon carbide sanding sheets of incrementally decreasing grit size and because the literature concludes that the wheel speed is the most important parameter that affects the cooling rate [9], the ejection pressure and melt superheat were kept constant and only the wheel velocity was varied.

Selected samples were mounted longitudinally in epoxy, polished and the microstructure of the ribbon cross-section was examined via SEM. Plan view SEM micrographs were obtained by mounting the ribbon horizontally on SEM stubs. Ribbon thicknesses were measured using a digital micrometer, and a minimum of 4 measurements were taken for each sample and averaged.

5.3.3 Dissolution of metal phase to excavate carbon material

The metal-carbon ribbon was immersed in 5 M HCl solution at room temperature to remove the metal phase and excavate carbon in the ribbon. The acid was filtered off using a Millipore filter (pore size 1 μm) and the remaining carbon material was washed with deionized water until neutral. Carbon materials were characterized using SEM, EDS, TEM, and Raman spectroscopy.

5.3.4 Ribbon Annealing

The melt-spun ribbons with varying carbon contents were annealed in a tube furnace under a flowing Ar atmosphere (99.999 %) at 1000 °C for 60 minutes. After annealing, the ribbon was cooled slowly at 0.06 K/s, from their respective annealing temperatures to room temperature.

5.3.4.1 Characterization tools

SEM imaging was performed using a Thermo Scientific Helios G4 UC Focused Ion Beam/ Scanning Electron Microscope (FIBSEM) instrument equipped with an energy dispersive spectroscopy (EDS) detector that was used for compositional analysis. The FIBSEM instrument was also used to prepare samples for imaging using the Thermo Scientific TF30 Transmission Electron Microscope (TEM). XRD was performed with a Bruker D8 Focus diffractometer with $\text{CuK}\alpha$ source. Raman spectroscopy was carried out

using a Horiba LabRam Evolution Raman microscope with a 532 nm laser line and a 100 μm spot size. 3-point BET surface area measurements were performed commercially using a Micrometrics TriStar II 3020 instrument.

5.4 Results and Discussion

5.4.1 Microstructural variation in Fe-C alloy

The iron-iron carbide phase diagram, shown in Figure 5-2, exhibits a eutectic at $\text{Fe}_{83}\text{C}_{17}$ (at. %). The cross-section of an $\text{Fe}_{83}\text{C}_{17}$ ingot prepared by RF melting is displayed in Figure 5-3(a). Here, it is evident conventional casting results in the expected lamellar microstructure that comprises of cementite (Fe_3C) and ferrite ($\alpha\text{-Fe}$), where the maximum solubility of carbon in the latter is only 0.09 at.%. Figure 5-3(b) shows that rapid solidification of the ingot results in ribbons with a much finer microstructure compared with the ingot. According to the phase diagram, melt spinning should result in lamellar microstructure containing austenite and ferrite; however, quenching could also result in the formation of the martensite phase, but detailed XRD analysis needs to be performed to confirm the presence of these phases. Figure 5-3 (c) shows ribbon that was annealed at 1000 $^\circ\text{C}$ for 1 hr. The domain sizes grew and unlike melt spun Ni-C, the majority of the ribbon was devoid of carbon precipitates. XRD patterns of ribbon before and after annealing (see Figure 5-4) are identical and show that ferrite, the BCC-Fe crystal structure is the primary phase present in the ribbon. One might notice that the (200) peak is missing from the XRD pattern. The most likely explanation for this occurrence is that the inherent geometry of the ribbon prevents the material from adopting the random orientation required to observe all phases, and as a result of adopting a preferred orientation, there was systematic error in the (200) peak intensity.

Atomic Percent Carbon

15

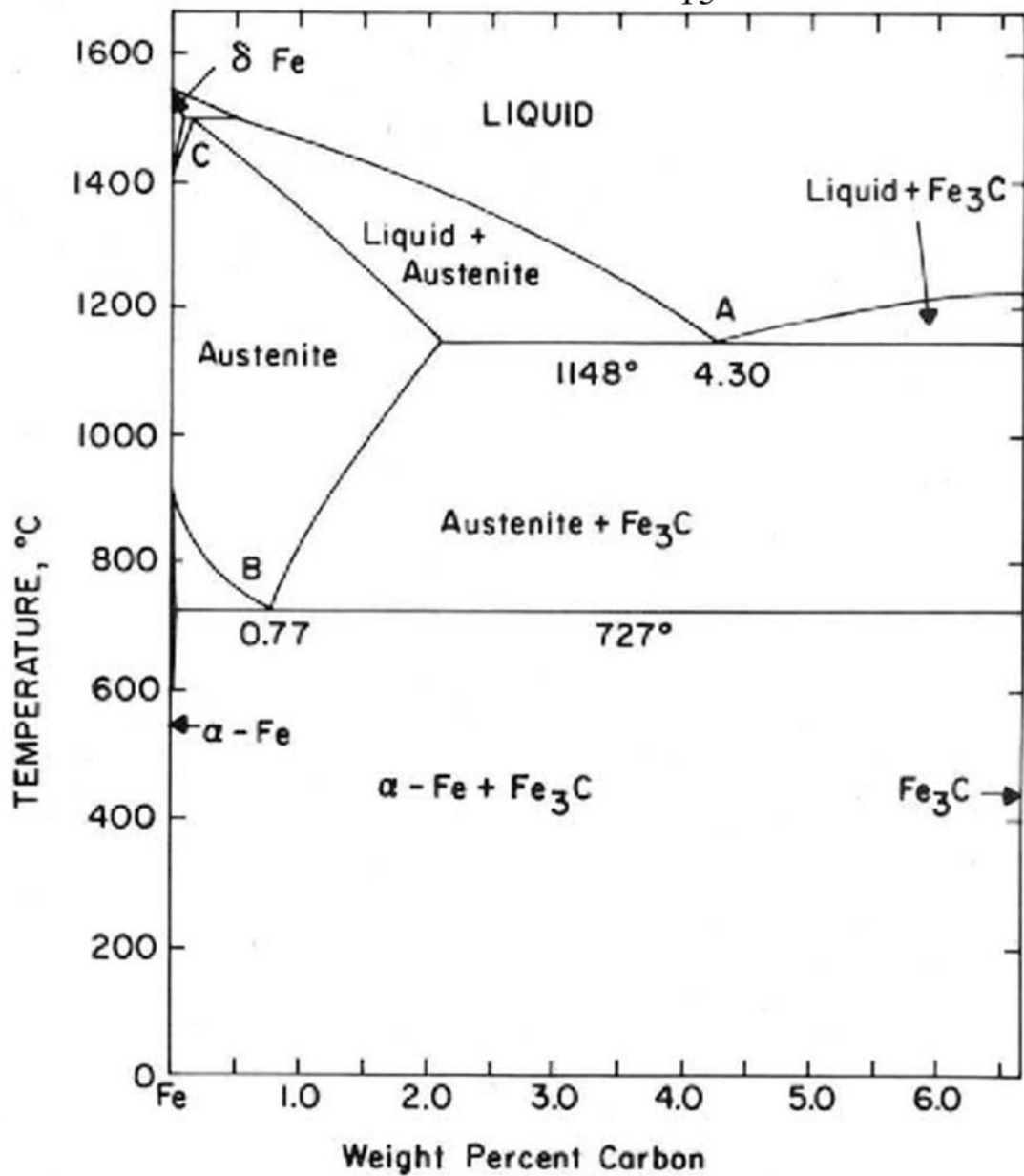


Figure 5-2. The iron-iron carbide phase diagram. Adapted with permission from Reference [10].

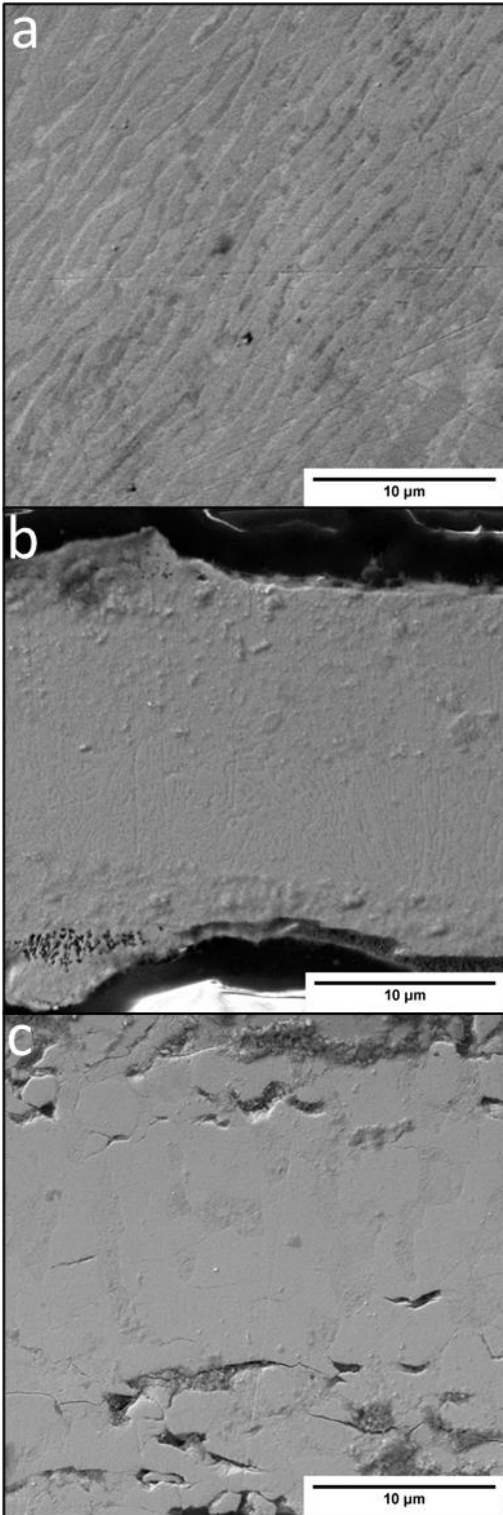


Figure 5-3. SEM images (a) Cross-section of $\text{Fe}_{83}\text{C}_{17}$ (at. %) alloy showing lamellar microstructure. (b) Cross-section of as-spun melt-spun ribbon showing finer features and a small region of carbon

precipitates. (c) Cross-section of melt-spun ribbon annealed at 1000 °C for 1 hour showing growth of domains.

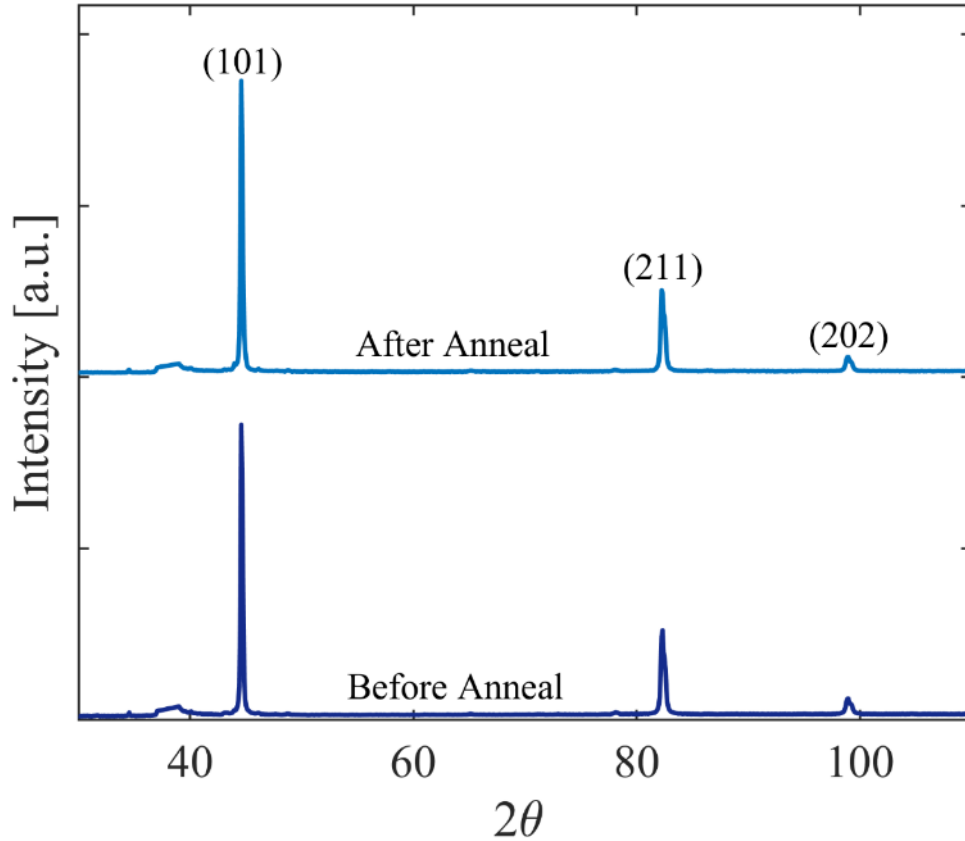


Figure 5-4. XRD Patterns of melt spun $\text{Fe}_{83}\text{C}_{17}$ ribbon before and after heat treatment. Peaks corresponding to bcc-iron are labeled.

5.4.2 Microstructural evolution of the carbon after Fe removal

5.4.2.1 Carbon from As-Spun Ribbon

The iron in the $\text{Fe}_{83}\text{C}_{17}$ ribbon was removed by chemical dissolution in hydrochloric acid. From the as-spun ribbon, the morphology of the freestanding material was a carbon foam with hierarchical porosity: the walls of the honeycomb lattice consisted of nanometer sized pores. It was surprising that an interconnected network of carbon could develop from an inhomogeneous ribbon consisting of multiple phases and

in a material with a low carbon. The mechanism of formation is not yet well understood; however, we suggest that the rapid quenching achieved by melt spinning allowed for the preferential supersaturation of carbon in the bcc-Fe interstitials over the other iron-carbon phases, increasing the C concentration above the percolation threshold, which is 24.5 at. % in the bcc lattice [11].

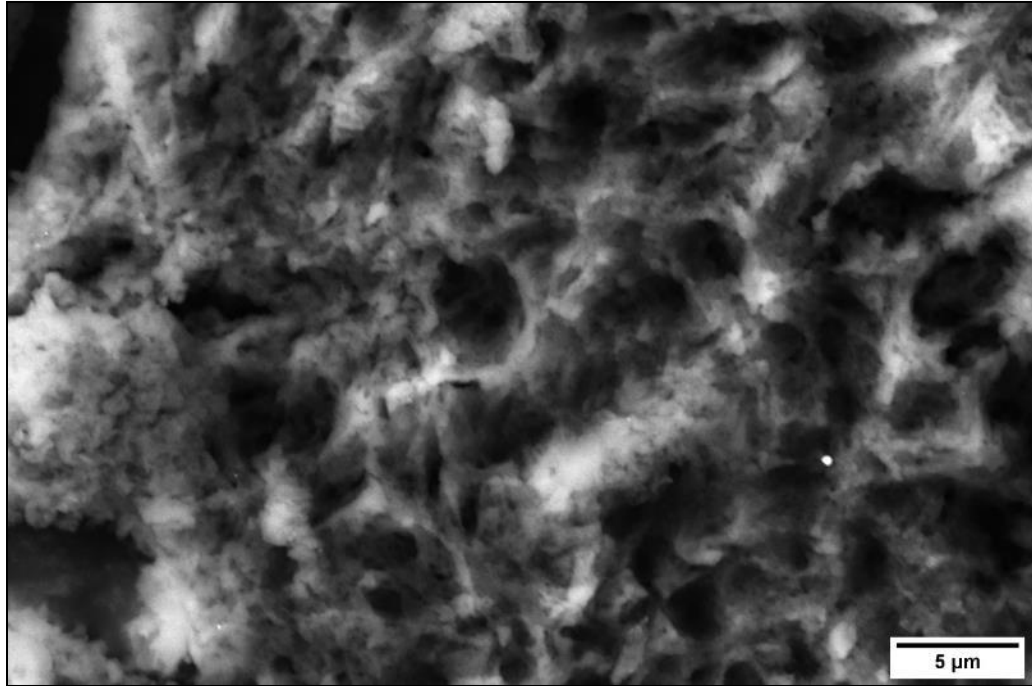


Figure 5-5. Carbon foam exhibiting hierarchical porosity formed by chemical dissolution of Fe from as-spun Fe-C ribbon

5.4.2.2 Carbon from Annealed Ribbon

The carbon foam excavated from melt spun Fe-C ribbon that was annealed at 1000 °C by chemical etching consolidated into millimeter-sized contiguous porous carbon sheets, shown in Figure 5-6. The thermal treatment also resulted in the disappearance of the sub-micron pores, but the pore size of the open cell structure was maintained.

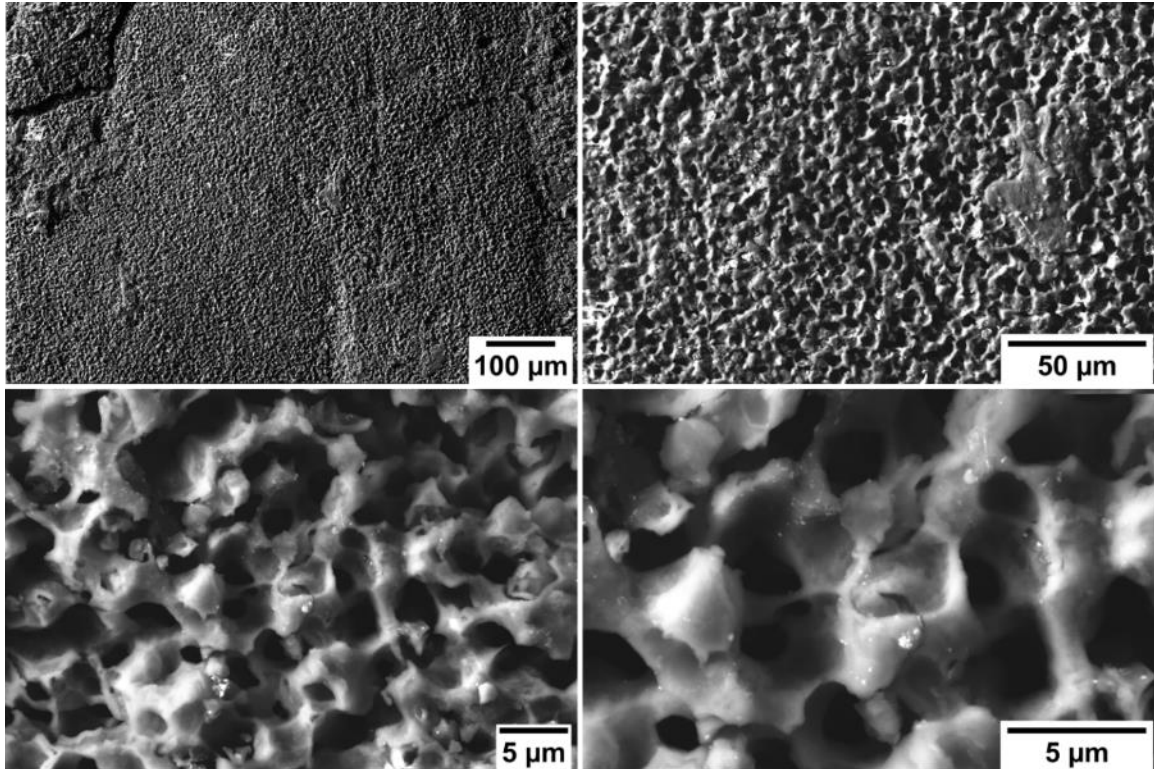


Figure 5-6. SEM micrographs of carbon foam fabricated from annealed melt spun Fe-C ribbon shown at different magnifications.

Figure 5-7 shows TEM micrographs of the carbon structure at increasing magnifications. The material is comprised of thin sheets of overlapping layers. The selected area diffraction pattern and the high resolution image show that the carbon is amorphous – it contains no long range order. The low degree of crystallinity in the microstructure is confirmed by the Raman spectrum (Figure 5-8) of the carbon foam that exhibits the characteristic features of amorphous carbon: a large I(D)/I(G) ratio, broad D and G peaks, and near absent 2D band. Graphitization of materials often occurs at temperatures around 1000 °C, so it was unexpected that the carbon foam exhibited such a low degree of structural order after annealing. The BET surface area of the carbon foam was found to be 4.5 m²/g (see Appendix B.2), a value comparable with a carbon foam

prepared by the carbonization of a monolithic resorcinol-formaldehyde resin at 400 °C [12].

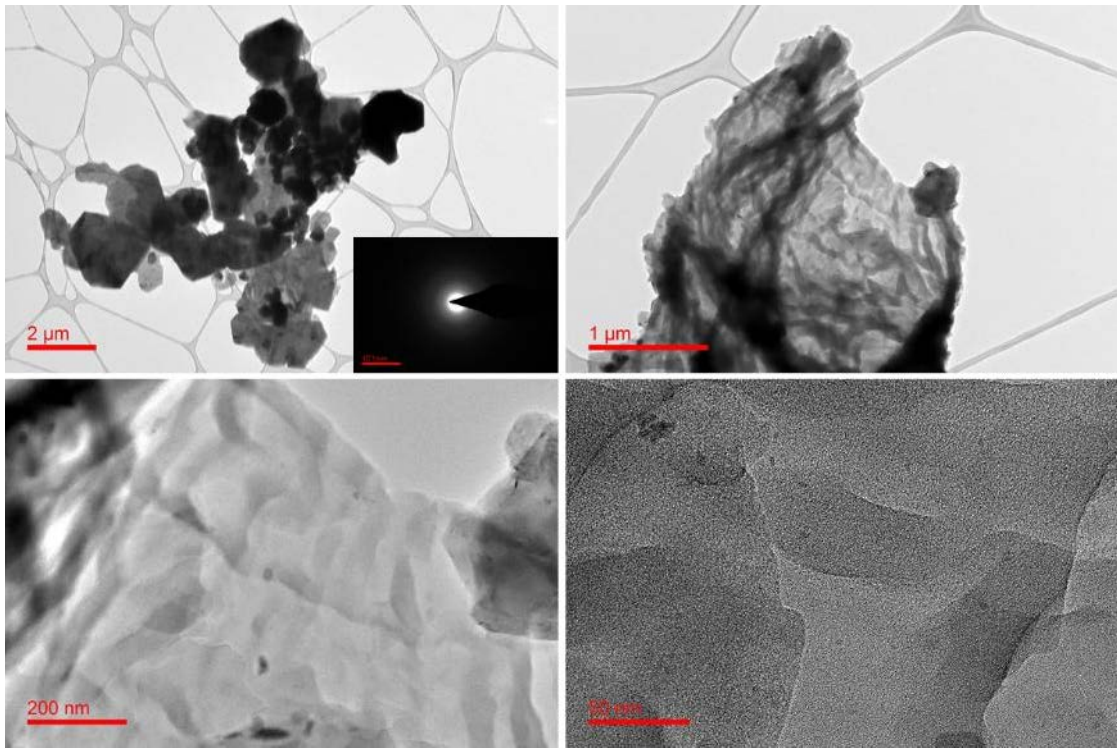


Figure 5-7. TEM micrographs of carbon from annealed Fe-C ribbon at different magnifications. (Inset) Selected area electron diffraction showing that the carbon is amorphous.

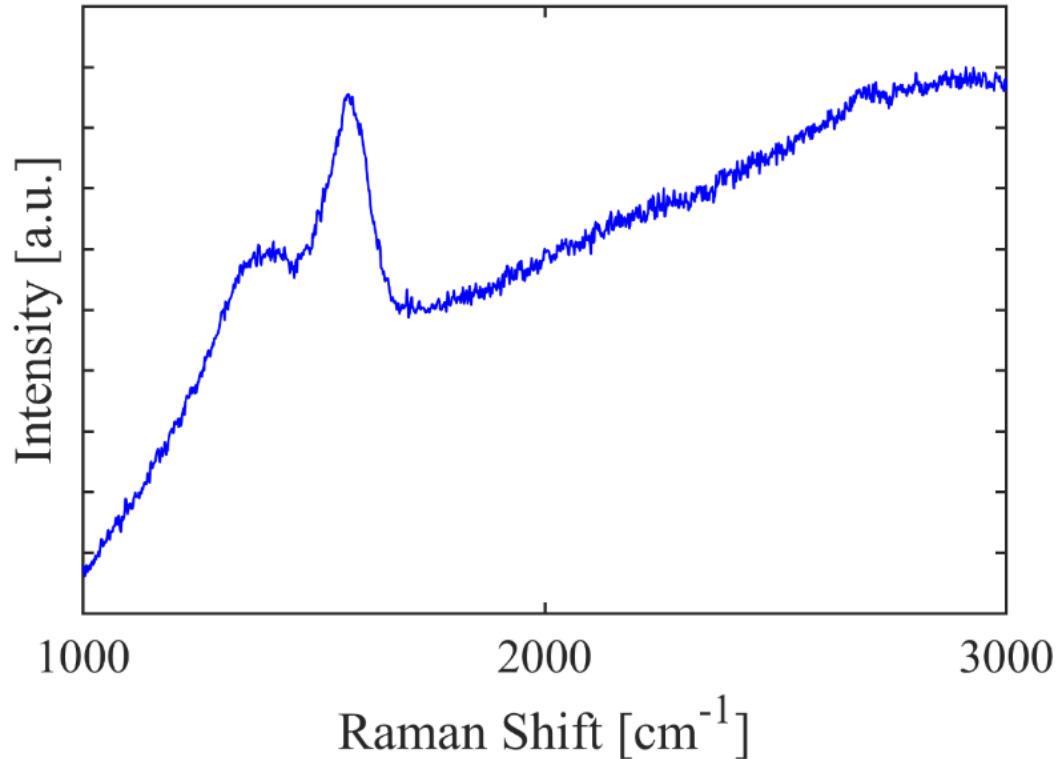


Figure 5-8. Raman spectrum of carbon from melt spun and annealed iron-carbon ribbon.

5.5 Conclusions

For the first time, a freestanding carbon foam with uniform pore sizes around 5 μm in diameter was prepared by melt spinning an iron-carbon alloy and subsequent chemical dissolution of the metal. Annealing of the ribbon can alter the porosity, where heat treatment transforms the material from exhibiting hierarchical porosity with nanometer sized pores in the carbon walls to a consistent honeycomb structure with solid walls. Even after annealing, Raman spectroscopy and TEM analysis revealed that the material consisted of stacked layers of amorphous carbon and the BET surface area of the material was $4.5 \text{ m}^2/\text{g}$.

Future studies on this topic would involve a thorough investigation of the phases produced via melt spinning, and if by altering the resultant phases, the type of carbon

material can also be varied. BET analysis and Raman spectroscopy should also be performed on material from as-prepared ribbon to better understand the effect of thermal treatment of the ribbon on the carbon produced. Furthermore, the annealing studies should be expanded, characterizing the ribbon and its carbon products after treatments at different times and temperatures. Finally, computational studies should be performed to elucidate the mechanism of the formation of a honeycomb lattice from rapidly solidified Fe-C ribbons.

5.6 References

- [1] H. Hosseini Bay, D. Patino, Z. Mutlu, P. Romero, M. Ozkan, C.S. Ozkan, Scalable Multifunctional Ultra-thin Graphite Sponge: Free-standing, Superporous, Superhydrophobic, Oleophilic Architecture with Ferromagnetic Properties for Environmental Cleaning, *Sci. Rep.* 6 (2016) 21858. <https://doi.org/10.1038/srep21858>.
- [2] X. Xu, L. Pan, Y. Liu, T. Lu, Z. Sun, D.H.C. Chua, Facile synthesis of novel graphene sponge for high performance capacitive deionization, *Sci. Rep.* 5 (2015) 8458. <https://doi.org/10.1038/srep08458>.
- [3] P. Lu, Y. Sun, H. Xiang, X. Liang, Y. Yu, 3D Amorphous Carbon with Controlled Porous and Disordered Structures as a High-Rate Anode Material for Sodium-Ion Batteries, *Adv. Energy Mater.* 8 (2018) 1702434. <https://doi.org/10.1002/aenm.201702434>.
- [4] H. Ji, L. Zhang, M.T. Pettes, H. Li, S. Chen, L. Shi, R. Piner, R.S. Ruoff, Ultrathin Graphite Foam: A Three-Dimensional Conductive Network for Battery Electrodes, *Nano Lett.* 12 (2012) 2446–2451. <https://doi.org/10.1021/nl300528p>.
- [5] Z. Chen, C. Xu, C. Ma, W. Ren, H.M. Cheng, Lightweight and flexible graphene foam composites for high-performance electromagnetic interference shielding, *Adv. Mater.* 25 (2013) 1296–1300. <https://doi.org/10.1002/adma.201204196>.
- [6] N. Li, Q. Zhang, S. Gao, Q. Song, R. Huang, L. Wang, L. Liu, J. Dai, M. Tang, G. Cheng, Three-dimensional graphene foam as a biocompatible and conductive scaffold for neural stem cells, *Sci. Rep.* 3 (2013) 1604. <https://doi.org/10.1038/srep01604>.
- [7] M. Inagaki, J. Qiu, Q. Guo, Carbon foam: Preparation and application, Elsevier Ltd, 2015. <https://doi.org/10.1016/j.carbon.2015.02.021>.
- [8] V. Chabot, D. Higgins, A. Yu, X. Xiao, Z. Chen, J. Zhang, A review of graphene

and graphene oxide sponge: Material synthesis and applications to energy and the environment, *Energy Environ. Sci.* 7 (2014) 1564–1596.

<https://doi.org/10.1039/c3ee43385d>.

- [9] R.C. Ruhl, Cooling rates in splat cooling, *Mater. Sci. Eng.* 1 (1967) 313–320.
[https://doi.org/10.1016/0025-5416\(67\)90013-4](https://doi.org/10.1016/0025-5416(67)90013-4).
- [10] G.J. Long, H.P. Leighly, The Iron-Iron Carbide Phase Diagram, *J. Chem. Educ.* 59 (1982). <https://pubs.acs.org/sharingguidelines>.
- [11] I. McCue, B. Gaskey, P.-A. Geslin, A. Karma, J. Erlebacher, Kinetics and morphological evolution of liquid metal dealloying, *Acta Mater.* 115 (2016) 10–23. <https://doi.org/10.1016/J.ACTAMAT.2016.05.032>.
- [12] K. Murakami, Y. Satoh, I. Ogino, S.R. Mukai, Synthesis of a Monolithic Carbon-Based Acid Catalyst with a Honeycomb Structure for Flow Reaction Systems, *Ind. Eng. Chem. Res.* 52 (2013). <https://doi.org/10.1021/ie400656x>.

6 Summary and Prospects

There has been a rich history of research on the topic of carbon from metal alloys. The ability to transform carbon into a large variety of functional forms is particular to this versatile element. The purpose of this work was to explore new metallurgical methods of engineering technologically useful carbon materials while also elucidating the fundamental kinetics and thermodynamics of these processes.

We proved that liquid metal dealloying is a viable technique by which porous graphite with tunable and uniform pore sizes can be fabricated by dissolution of Si from SiC in molten germanium. In addition to expanding the set of materials available to conventional liquid metal dealloying, we also provided an alternate route to the synthesis of a carbide-derived carbon by this method. The kinetics of dealloying for this system deviates from the expected behaviors typically seen in both liquid metal and electrochemical dealloying of metals; liquid metal dealloying of a non-metal precursor exhibits kinetic features of both conventional processes.

We also transformed commercially prepared graphite into amorphous carbon nanospheres and high aspect ratio graphite flakes by melt spinning nickel carbon alloys. Melt spinning allowed for solidification rates up to 10^6 K/s; the resultant Ni ribbon consisted of fine grains supersaturated with carbon atoms, where carbon precipitation in the Ni grain boundaries was observed for ribbon with higher carbon fractions. Annealing of the Ni-C melt spun ribbon led to the growth of spherical C precipitates within the bulk of the ribbon via diffusion-driven Ostwald ripening, but also led to the growth of high aspect ratio graphite flakes on the free surfaces of the ribbon.

Once we understood the kinetics of the rapid solidification of the metal-carbon ribbon, we removed the Ni matrix by chemical dissolution in acid and examined the microstructural evolution of the freestanding carbon because of varying experimental parameters. By increasing the carbon fraction in the parent ingot and/or increasing the annealing temperature of the melt spun ribbon, amorphous nanospheres of carbon were sequentially transformed into highly crystalline flakes of graphite where the number of layers can also be controlled by varying these parameters.

Nanoporous graphite with a honeycomb lattice architecture was also prepared by melt spinning. The iron-carbon phase diagram is complex compared to that of nickel-carbon and resulted in a carbon morphology distinct from that produced by the rapid solidification of Ni-C alloys. The freestanding carbon foam synthesized from the as-prepared Fe-C ribbon exhibited hierarchical porosity: the cell sizes were less than 4 μm in diameter, but the cell walls contained nanometer-sized pores. Annealing of the ribbon before Fe dissolution led to the densification of the walls but the cell sizes remained unchanged. The foam, even after thermal treatment, was amorphous with a low BET surface area of $\sim 5 \text{ m}^2/\text{g}$.

This work showed the utility of dealloying and melt spinning in the fabrication of carbon materials. Future work should involve the exploration of alternate systems that are amenable to either process. With respect to dealloying, there are potentially multiple other carbon-containing systems that may produce carbon materials of technological value. For example, via liquid metal dealloying, Gaskey et al. [1] fabricated a self-assembled porous Nb/Nb₅Si₃ composite with excellent mechanical properties compared to porous Nb by adding small amounts of Si (3 at. %) to the parent alloy. Perhaps, porous

carbon/SiC composite materials can be engineered by dealloying of metal-C-Si precursor alloy such as Mn-C-Si in molten Bi. Figure 6-1 shows micrographs of a $Mn_{80}Si_{10}C_{10}$ sample that was dealloyed in molten Bi and etched in acid to reveal a carbon-containing product with highly faceted ligaments. Although the desired composite did not develop, we show that this system is amenable to dealloying, and different initial alloy compositions may yield interesting carbon materials.

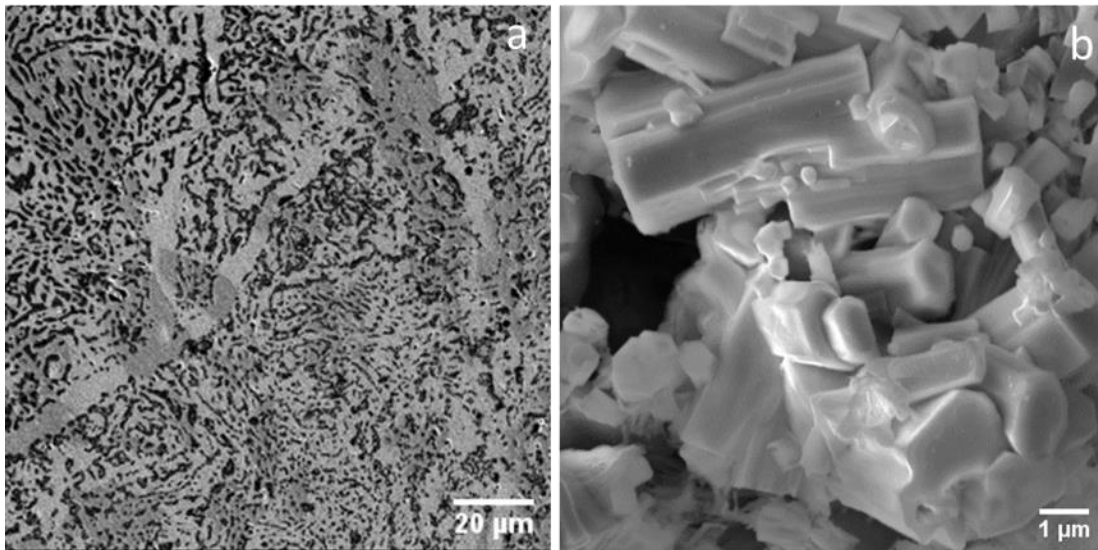


Figure 6-1. (a) Scanning electron micrograph showing $Mn_{80}Si_{10}C_{10}$ that was dealloyed in liquid Bi at 800 °C. SiC powder was used to make the parent alloy. The light grey areas are Bi rich and dark grey areas are ligaments that comprise large amounts of residual Mn (~20 at. %) along with Si and C. (b) The dealloyed material post etching in acid shows faceted ligaments that comprised of 94 at. % C with some residual Si.

The work reported in this dissertation showed that porous carbon films can be grown on SiC via dealloying. Future work should explore the dealloying of carbides in various form factors. For example, porous carbon powders have utility in a variety of applications and the liquid metal dealloying of SiC powders could prove another useful technique in the synthesis of high surface area porous carbon powders.

Finally, the fundamental rate-limiting kinetics of electrochemical and liquid metal dealloying are well understood. For ECD, the rate-limiting step is the removal of a dissolving atom from a terrace site; for LMD, it is the dissolution of the leaving species from the pores. However, the kinetics of dealloying a stoichiometric precursor such as SiC exhibits kinetic features that do not fall neatly into those two categories. Kinetic Monte Carlo simulation can be performed to understand the origins of the interfacial reaction that gives rise to the rate-limiting behavior observed when SiC is dealloyed in molten Ge.

Other materials systems also have the potential to produce technologically useful carbon products via melt spinning. For example, the Mn-C phase diagram exhibits even higher solubility for carbon than nickel – near 40 at. % at 1400 °C. However, due to the high vapor pressure of Mn, C-Mn alloys are experimentally challenging to cast. Its vapor pressure is reduced by alloying with Ni, and we have successfully melt spun Ni₄₀Mn₄₀C₂₀ ribbon, shown in Figure 6-2 (a). Melt spinning of this system yields a novel metallic glass, as evidenced by the lack of sharp peaks in the powder diffraction pattern and crystallinity can be achieved via annealing; the corresponding diffraction patterns are shown in Figure 6-2 (b).

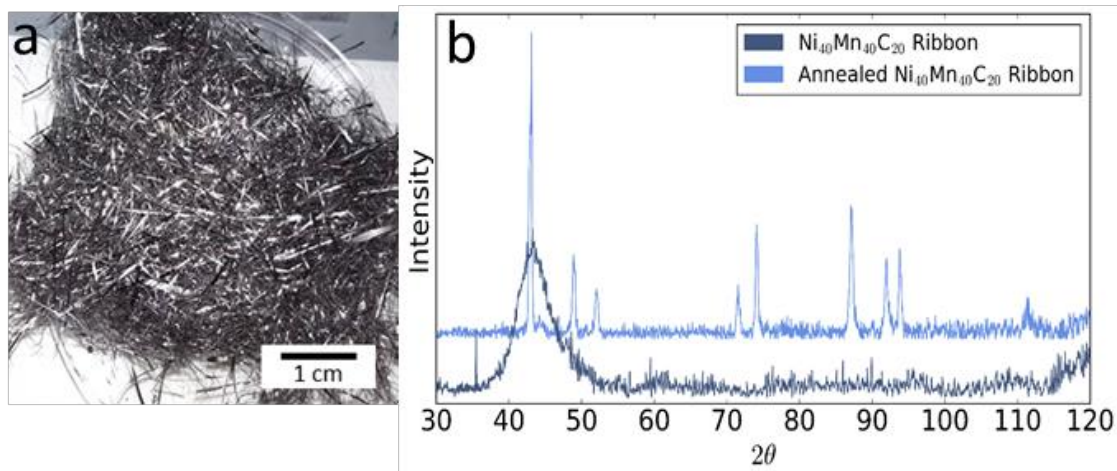


Figure 6-2. (a) $\text{Ni}_{40}\text{Mn}_{40}\text{C}_{20}$ melt spun ribbon. (b) Powder diffraction patterns of $\text{Ni}_{40}\text{Mn}_{40}\text{C}_{20}$ melt spun ribbon before and after annealing showing the heat treatment transforms the ribbon microstructure from amorphous to crystalline.

Mentioned throughout the manuscript were several potential applications for the carbon material fabricated in this work. For example, porous carbon can be used in electrode materials and water and gas purification devices. The high aspect ratio graphite flakes produced by melt spinning Ni-C can also be investigated as a precursor material for graphene fibers [2].

An essential initial impetus for this work involves the reduction in the emission of greenhouse gases. In 2016, 5171 million metric tons of carbon dioxide were emitted into the atmosphere by the U.S. from energy related sources such as natural gas [3]. The impact of greenhouse gas emissions on climate change has motivated numerous scientists to investigate methods to mitigate the deleterious effects of energy production on our environment. Our group was no exception. We have investigated the decomposition of natural gas into solid carbon and hydrogen over a nickel chloride intermediate. Using methane to produce clean fuel, hydrogen instead, we can potentially divert 550 million metric tons of CO_2 emitted via the combustion of methane [3]. However, a challenge that

arises from this process is that massive amounts of solid carbon will be produced. If this “waste” carbon can be transformed into value-added materials, there will be a strong economic incentive for the relevant industries to adopt methane decomposition methods. The work discussed in this manuscript offers techniques to address such challenges while also adding to the toolset of ways to engineer technologically important carbon materials.

6.1 References

- [1] B. Gaskey, I. McCue, A. Chuang, J. Erlebacher, Self-assembled porous metal-intermetallic nanocomposites via liquid metal dealloying, *Acta Mater.* 164 (2019) 293–300. <https://doi.org/10.1016/J.ACTAMAT.2018.10.057>.
- [2] Z. Xu, C. Gao, Graphene fiber: A new trend in carbon fibers, *Mater. Today.* 18 (2015) 480–492. <https://doi.org/10.1016/j.mattod.2015.06.009>.
- [3] How much of U.S. carbon dioxide emissions are associated with electricity generation? - FAQ - U.S. Energy Information Administration (EIA), (n.d.). <https://www.eia.gov/tools/faqs/faq.php?id=77&t=11> (accessed January 29, 2018).

Appendix A: Porous Tungsten Fabricated by the Liquid Metal Dealloying of Tungsten Silicides

A.1 Summary

Three-dimensional porous W was prepared by dealloying W-Si plasma-sprayed coatings and bulk W-Si ingots in molten Ge, following by chemical dissolution of the Ge phase to reveal open porosity. The bulk $W_{41}Si_{59}$ (at. %) parent ingot was dealloyed to demonstrate proof-of-concept and the plasma sprayed coating exhibited uniform pore sizes that could be controlled by varying the experimental time and temperature. The W ligaments were larger than expected for a material with an exceedingly high melting point. It was observed that the W ligament sizes fell above the universal trendline for the variation of ligament size with inverse homologous dealloying temperature for metal precursors. However, the ligament dimensions corroborated well with the porous C ligament sizes fabricated by the dealloying of SiC, indicating that significant coarsening is involved in the dealloying of stoichiometric precursors. The liquid metal dealloying of W-Si provides an alternate and facile route for the fabrication of bulk porous W and porous W coatings at low temperatures ($< 1300\text{ }^{\circ}\text{C}$) and atmospheric pressure.

A.2 Background

Owing to its superlative materials properties, tungsten is an attractive metal for applications that require excellent thermal stability, high tensile strength, wear resistance, and good dynamic stress compression properties [1]. In particular, porous tungsten is used as a matrix in composites; for example, porous W is impregnated with electron emissive materials for use in high current density cathodes [2], W-Re composites are

used as rocket nozzles in spacecrafts [3], and porous W infiltrated with Cu is used as heat-sink materials for high density integrated circuits [4].

Traditional methods for synthesizing porous W involve sintering of powders [2,5]. The inability to finely tune the pore size and porosity coupled with the extreme processing conditions of high temperatures (> 2000 °C) and pressures (~ 200 MPa) have led researchers to explore more favorable methods of fabrication [3,4]. In 2003, Selcuk et al. [6] designed a reactive sintering method to produce porous W at temperatures around 1200 °C with a high degree of uniformity from tungsten powders with average particle sizes of 8 μm and 18 μm . In 2017, Shen et al. [7] reported the fabrication of three-dimensional porous W with controlled pore size from $1 - 6$ μm using a pressureless sintering method called tape-casting.

The porous W fabrication methods described above involve complicated powder metallurgy processing techniques that limit the form factor of the material produced. However, McCue [8] reported the fabrication of submicron sized porous W composites via the liquid metal dealloying of W-Ti alloys in molten Cu/Ag demonstrating the LMD is a feasible route in the synthesis of nanoporous W. In this work, we confirm that liquid metal dealloying is a facile route to fabricate porous W monoliths but we also show that it can be used to fabricate porous W coatings, which has potential for use in applications where high temperature coatings are required.

W has the highest melting point of any metal and because of this, homogenous W alloys are experimentally challenging to fabricate by traditional casting methods. By using the eutectic W-Si composition, we were able to prepare bulk tungsten silicide ingots via induction melting. The W intermetallics were dealloyed in molten germanium,

followed by the chemical removal of the Ge phase in cold aqua regia. With this system, the thermodynamic requirements for dealloying are met: there is limited solubility of W in Ge (< 2 at. % at temperatures below 1500 °C) but Ge and Si are miscible over the entire composition range, see Figure A-1. Similar to the dealloying of SiC detailed in Chapter 2, WSi_2 and W_5Si_3 are stoichiometric ceramic compounds instead of homogeneous metal alloys conventionally used as precursors in dealloying. The dealloying process was performed at temperatures below 1400 °C and atmospheric pressure and produced materials with uniform pore sizes that are tunable by controlling the processing temperature. Therefore, porous W synthesized by LMD is a suitable alternative to fabrication via powder metallurgy.

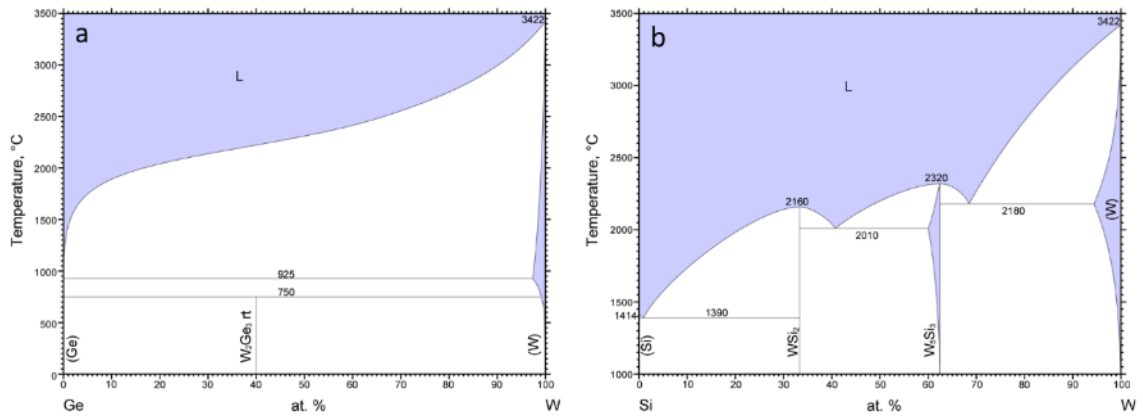


Figure A-1 (a) Binary Ge-W phase diagram showing limited solubility of W in liquid Ge below 1500 °C. (b) Binary Si-W phase diagram showing a eutectic point at 41 at. % W. © ASM International.

A.3 Experimental Methods

A.3.1 Bulk Material Preparation

The W-Si binary phase diagram shown in Figure A-1(b) displays a eutectic at Si-41 at.% W and 2010 °C and. Using W pellets (99.95 wt.%) and Si pieces (99.995 wt.%)

from Kurt J. Lesker, the parent ingot of the eutectic composition was prepared by inductively melting the Si and W in a water-cooled copper crucible using a 45 kW Ambrell Ekoheat ES induction system under a flowing Ar atmosphere (99.999 at. %). Single samples were melted a minimum of three times to ensure total mixing and homogeneity. A ProtoMAX waterjet cutter (OMAX Corporation) was used to make ~ 1 mm thick slices of the ingot.

A.3.2 Plasma-Sprayed WSi₂ Coating

The WSi₂ coated was prepared at the Johns Hopkins Applied Physics Laboratory and the experimental details are proprietary. A coating of WSi₂ approximately 250 μm thick was plasma sprayed on a bulk W coupon sized 30 mm long x 5mm wide x 3 mm thick.

A.3.3 Liquid Metal Dealloying

The dealloying process is depicted in Figure A-2. In a typical experiment, a ~ 20 g mass of n-doped germanium (99.999 wt. % from Kurt J. Lesker) was inductively heated in a graphite crucible using a 4.5 kW Ambrell EkoHeat power supply to a specified temperature.

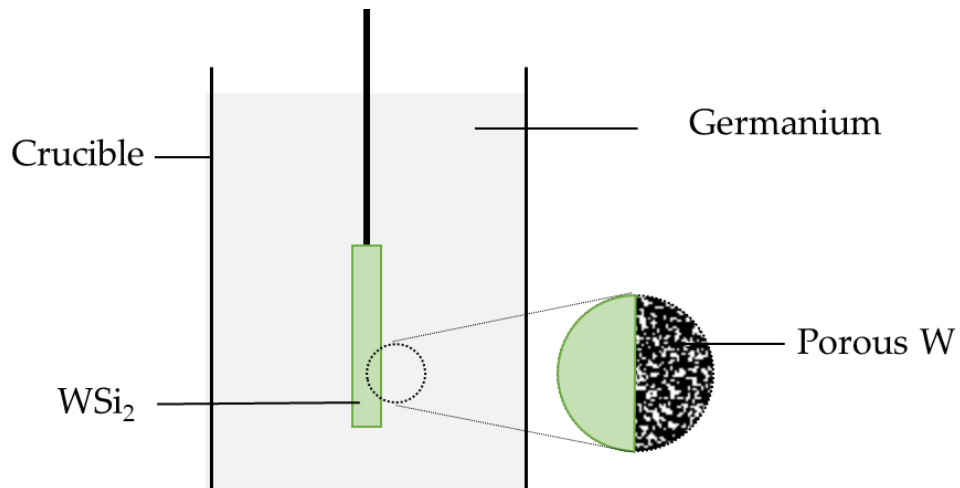


Figure A-2. Schematic description of the liquid metal dealloying of a WSi_2 intermetallic in liquid Ge. Si is selected dissolved leaving behind a porous network of W ligaments.

A.3.4 LMD of $W_{41}Si_{59}$ ingot

A single slice of the $W_{41}Si_{59}$ ingot was immersed into the liquid Ge at 1300 °C for 120 seconds using a vacuum manipulator arm, after which the sample was raised from the bath to initiate cooling and discontinue the dealloying process. The interior of the sample retained the microstructure of the parent material and the dealloyed region extended from the geometric surface inward to the dealloyed interface; this dealloyed region at the sample surface consisted of porous W infiltrated with solid Ge.

A.3.5 LMD of the Plasma Sprayed WSi_2 Coating

A bar of solid W with a plasma-sprayed with a $\sim 200 \mu\text{m}$ thick WSi_2 coating was immersed in molten Ge at 1200 °C for 30 seconds and 1300 °C for 90 seconds in a process analogous to that described in Chapter 2.3.1.

A.3.6 Characterization of As-Dealloyed porous W/Ge Samples

Dealloyed samples were mounted in epoxy and mechanically polished through their cross-sections. A Thermo Scientific Helios G4 UC Focused Ion Beam/ Scanning Electron Microscope (FIBSEM) instrument equipped with an energy dispersive spectroscopy (EDS) detector was used to image the material and perform compositional analysis.

A.3.7 Excavation of the Pure Porous Tungsten Phase

The Ge phase was etched in room temperature aqua regia for 1.5 hours and rinsed thoroughly in deionized water before imaging via optical and electron microscopy.

A.4 Results and Discussion

A.4.1 LMD of $W_{41}Si_{59}$ ingot

Typically, dealloying is performed on a homogenous alloy or a single phase material such as SiC. However, Yu et al. demonstrated that it is possible to dealloy an inhomogeneous precursor when they fabricated porous graphite with two different microstructures from an $Mn_{85}C_{15}$ that phase separated into α -Mn and $Mn_{23}C_6$. A similar phenomenon occurs in the LMD of the $W_{41}Si_{49}$ parent material. The phase diagram in Figure A-1(b) shows that $W_{41}Si_{59}$ is a eutectic composition; therefore, one would expect that a melt at this composition would solidify into the typical lamellar eutectic lamellar microstructure consisting of WSi_2 and W_5Si_3 phases.

Figure A-3(a) shows a micrograph of dealloyed $W_{41}Si_{49}$, where the original parent microstructure is also visible. The expected phase separation is evident, the darker grey regions are WSi_2 and the lighter grey regions are W_5Si_3 . The interface between the dealloyed and parent regions is evident and is highlighted by the dashed line in Figure A-

3(a); however, it is not sharp and parallel to the geometric sample edge as in other reported dealloyed materials. In fact, the anisotropy in the parent material is maintained and certain regions seem to act as short-circuit pathways for the penetration of Ge into the sample. This is the first time such a phenomenon has been observed and is worthy of further investigation.

The dealloyed area, which sits at the geometric edge of the sample, is magnified in Figure A-3(b) and here, the Ge rich phase appears as the darkest grey color and the lightest grey is the W rich phase. A third phase, highlighted by the green arrow, also appears at the boundary between the Ge layer the encases the sample and the porous W. It was found to be a heretofore unknown ternary compound that was determined to comprise 32 at.% Ge, 45 at.% Si and 23 at.% W. An interconnected network of W ligaments that appears to maintain the crystallographic texture of the parent material is visible. Figure A-4 shows large faceted lamellar-like W ligaments at the geometric sample surface, adjacent to disconnected droplets, followed by an interconnected W network that also maintains the crystallographic texture of the parent material. While the non-uniformity in the parent material leads to a wide pore size distribution, this experiment serves as proof-of-concept that porous W can be fabricated by the LMD process.

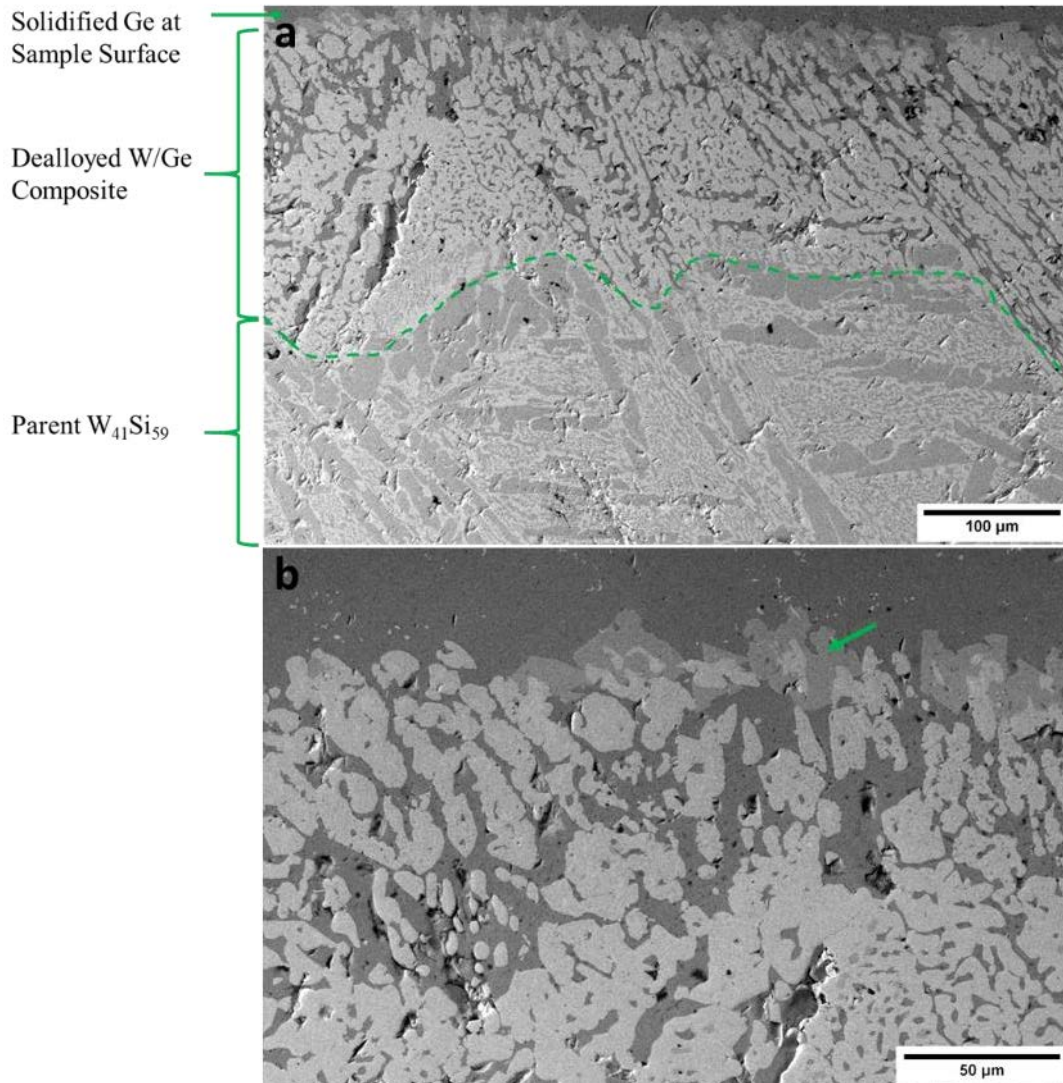


Figure A-3. Scanning electron micrographs of $W_{41}Si_{59}$ dealloyed in molten Ge. (a) A distinct but non-planar interface between the dealloyed layer and the non-dealloyed parent material is shown by the dashed line. The parent material exhibits two major phases: the darker grey regions are WSi_2 and the lighter grey regions are W_5Si_3 . (b) shows a magnification of the dealloyed region. The darkest grey phase is Ge rich and the lightest grey phase is W rich. A third phase, highlighted by the green arrow, is an unknown ternary compound that was determined to be comprised of 32 at.% Ge, 45 at.% Si and 23 at.% W.

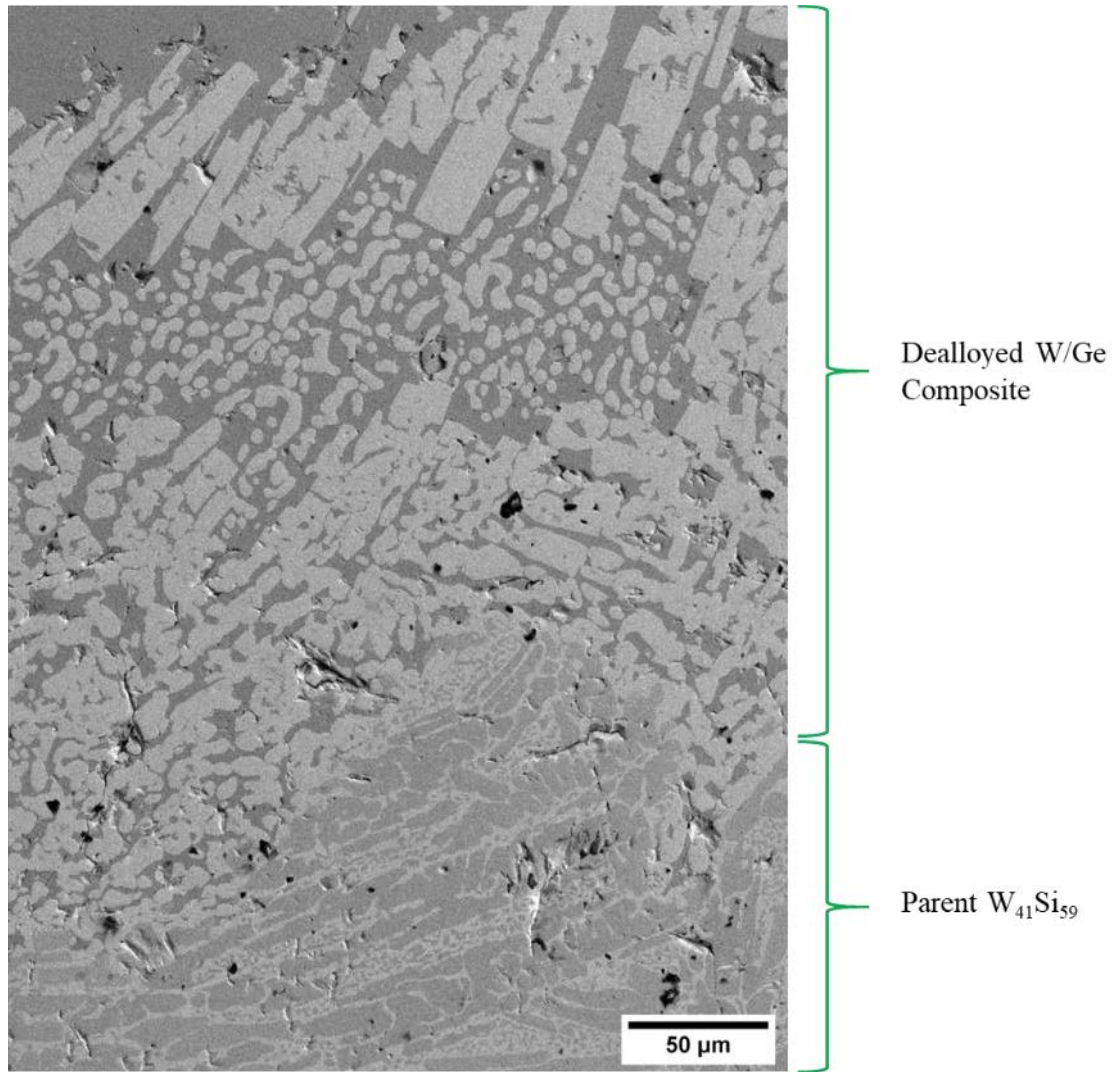


Figure A-4. Scanning electron micrograph of dealloyed $W_{41}Si_{59}$ showing large faceted lamellar-like W ligaments at the geometric sample surface, adjacent to disconnected droplets followed by an interconnected W network that maintains the crystallographic texture of the parent material.

A.4.2 LMD of WSi_2 coating

Figure A-5 shows a scanning electron micrograph of tungsten silicide plasma sprayed coating dealloyed in molten Ge at 1200 °C for 30 seconds. The pure W support is on the bottom of the image. The parent plasma-sprayed microstructure is in the middle region of the image consists of separate WSi_2 (which appears as the darker grey color) and W_5Si_3 (lighter grey). Also included are C-rich impurities (black). The highly

anisotropic texture observed in the dealloying of bulk $W_{41}Si_{59}$ is absent here, and as a result, the interface between the dealloyed layer and the parent material is sharp, continuous and evident, where the dealloyed layer consisting of porous W ligaments impregnated with Ge is shown at the top of the image.

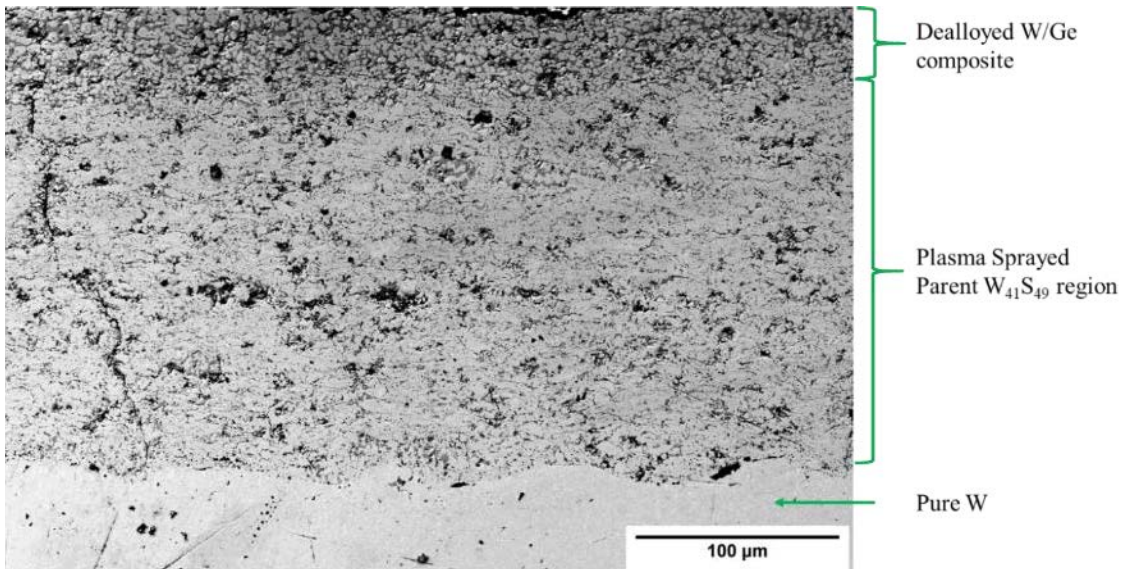


Figure A-5. Scanning electron micrograph of a plasma-sprayed tungsten silicide coating dealloyed in molten Ge at 1200 °C for 30 seconds. The pure W support is on the bottom of the image, the parent plasma-sprayed microstructure is in the middle region and the dealloyed layer consisting of porous W ligaments impregnated with Ge is shown at the top.

Figure A-6 shows higher magnification SEM micrographs of plasma-sprayed W-Si coatings dealloyed in Ge at 1200 °C for 30 seconds and 1300 °C for 90 seconds. In both images, the lighter grey regions represent the W-rich ligaments and the darker grey areas consist of the Ge rich bath that solidified within the W pores. The strong crystallographic texture exhibited by the bulk W-Si material was not present in the parent plasma sprayed material; however, the latter showed horizontal striations characteristic of the plasma spraying process. In contrast to the porous W prepared by dealloying the bulk ingot, both plasma-sprayed samples show a high degree of uniformity in the ligament

size. There is a difference in observed microstructure between the samples processed at 1200 °C and 1300 °C, however, due to coarsening. The material dealloyed at the lower temperature developed average ligament sizes of $\sim 3 \mu\text{m}$, and the ligaments form an interconnected network, especially at the interface between dealloyed and parent materials where limited reaction time prevented significant coarsening. Ligaments became more disconnected closer to the geometric sample edge as this is the region that was dealloyed first. At 1300 °C, the plasma spray coating was fully dealloyed through its thickness; W ligaments were larger, $\sim 8 \mu\text{m}$, and formed as disconnected droplets due to the higher temperature and longer dealloying time. Shown in Figure A-7 is the delamination of the coating from the W substrate; this occurrence should be avoided in the preparation of the material as a coating for future applications.

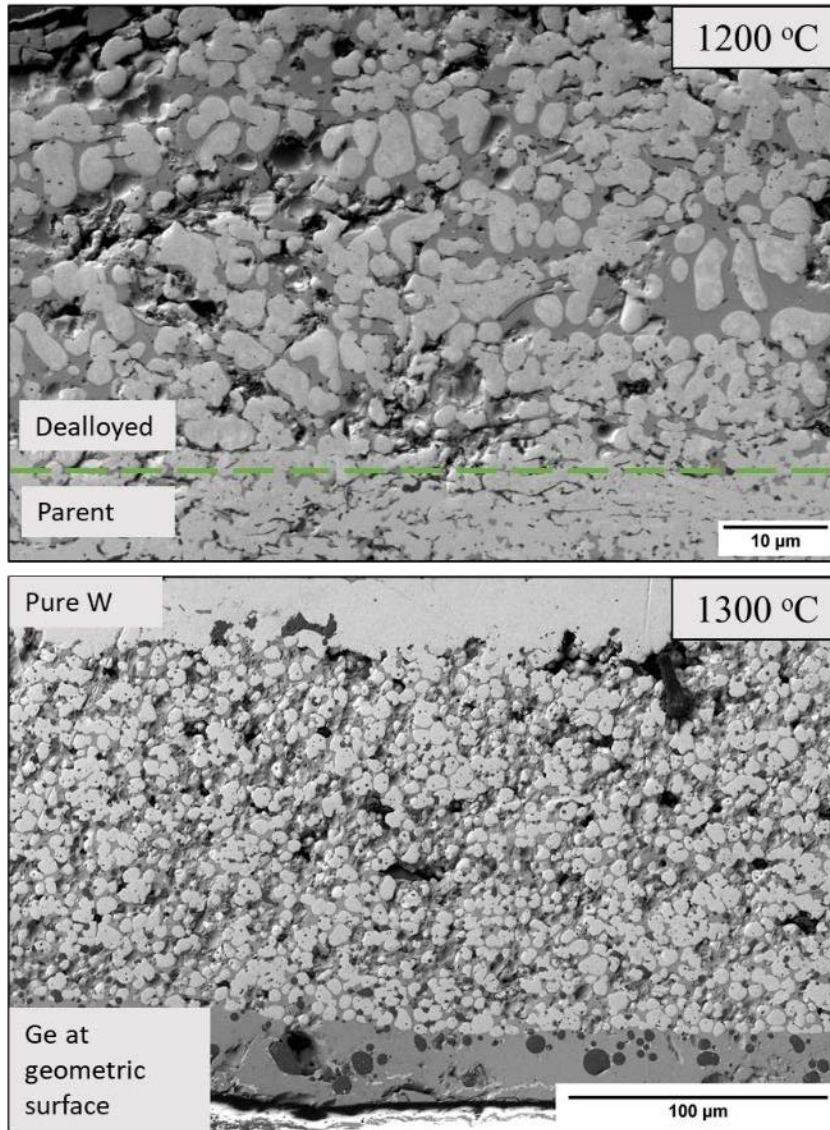


Figure A-6. (top) SEM image of W-Si plasma sprayed coating dealloyed at 1200 °C for 30 seconds. (bottom) SEM image of W-Si plasma sprayed coating dealloyed at 1300 °C for 90 seconds.

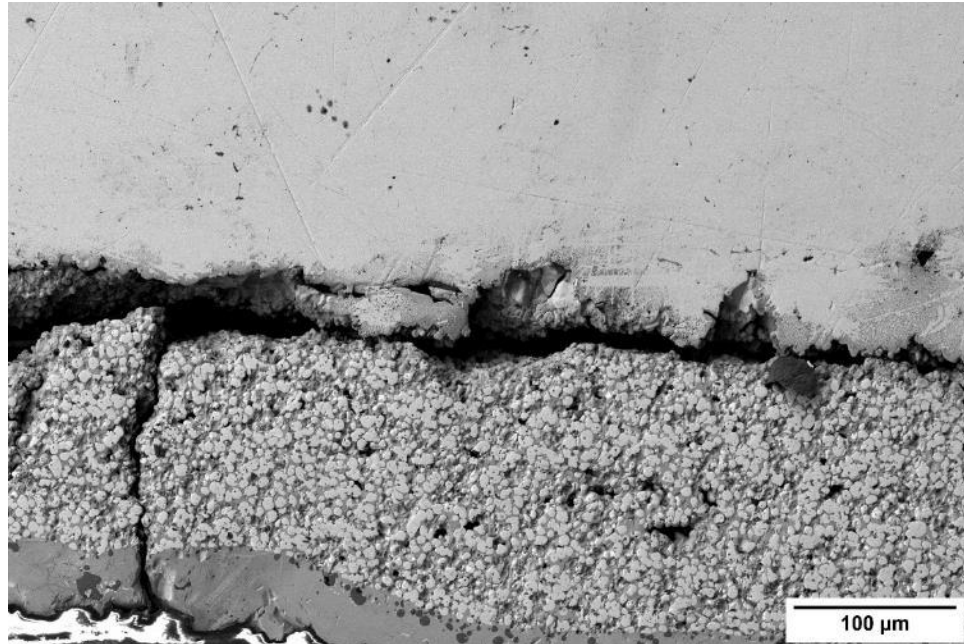


Figure A-7. SEM image showing delamination of the porous W/Ge composite prepared by dealloying at 1300 °C for 90 seconds.

The Ge was chemically etched from the 1200°C sample and images of the resultant porous W structure are shown in Figure A-8. Removal of the Ge phase does not affect the underlying W-Si parent structure and the porous W layer showed good structural integrity as it did not disintegrate or delaminate from the layer beneath it.

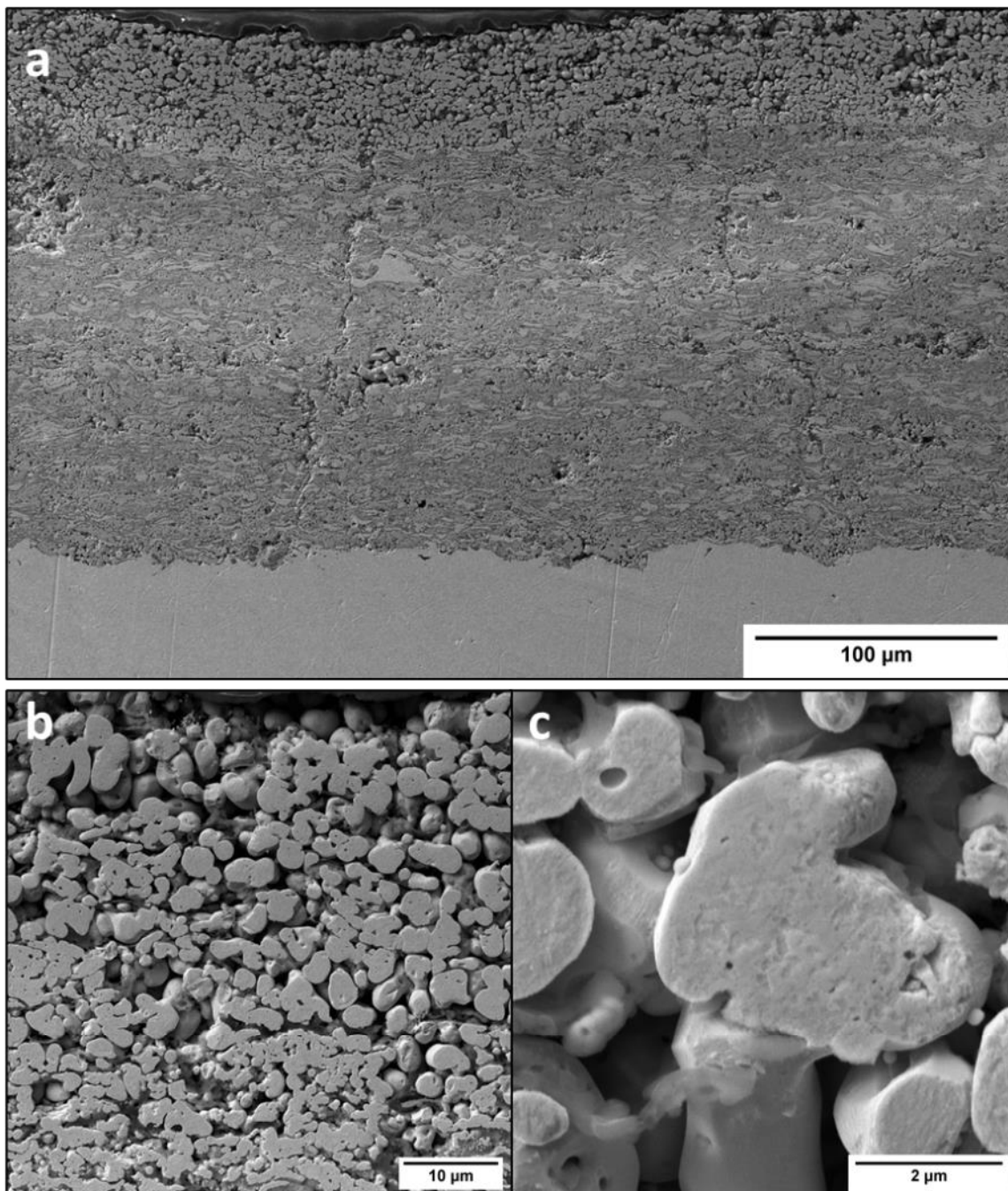


Figure A-8. Scanning electron micrographs of porous W coatings after removal of the Ge phase from the pores by chemical dissolution. (a) Ge was etched from the surface dealloyed layer while the underlying parent plasma sprayed coating remained pristine. (b-c) Higher magnification images of the porous W layer.

A.4.3 Ligament Size

In Chapter 1.4.5, we discussed the relationship between inverse homologous temperature and ligament size: ligament diameter scales with “inverse homologous temperature” $T_m/T_{dealloy}$ for both LMD and ECD [9,10]. According to the trend shown previously in Figure 1-12, materials with higher melting points form smaller ligaments when dealloyed. In this work, the sizes of the porous W ligaments ranged from 10 – 80 μm , values that are much larger than expected for a metal with a melting point as high as 3422 °C. Figure A-9 shows an updated version of Figure 1-12 that includes the W data points acquired in this work; we see that W ligaments do not obey the usual relationship between homologous temperature and ligament size first described by Chen and Sieradzki. We saw in Chapter 2 that porous carbon dealloyed from a SiC precursor also falls above the observed trend line for porous materials fabricated from the dealloying of metal precursors. In fact, as depicted in Figure A-9, there seems to be a significant coarsening in the dealloying of stoichiometric precursors. In traditional dealloying, coarsening is mediated by thermally activated surface diffusion of the remaining component. We surmise that the chemical changes that simultaneously accompany surface diffusion may add complexity to the rate-limiting steps observed in traditional dealloying, the result of which is increased expected ligament diameter.

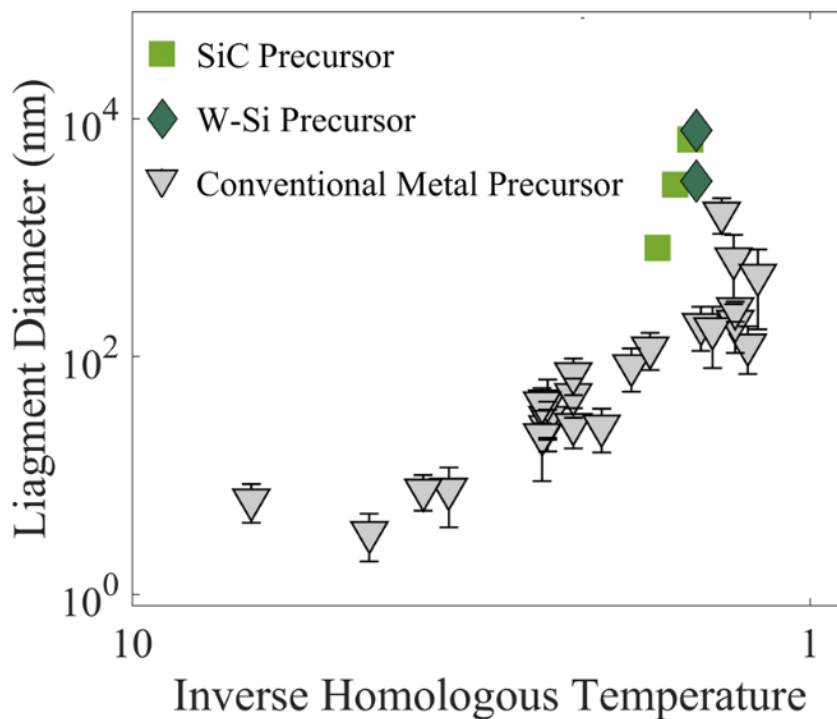


Figure A-9 Trend in ligament diameter versus inverse homologous temperature ($T_m/T_{dealloy}$) for electrochemical dealloying and liquid metal dealloying at different times, shown as grey triangles for metal systems (adapted with permission from reference [9]). Error bars represent one standard deviation. For comparison, the trend between ligament diameter and inverse homologous temperature for SiC ($T_{sublimation}/T_{dealloy}$) is shown as green squares. Error bars lie within the data markers. The data for porous Wi is shown as the green diamond.

A.5 Conclusions and Future Work

Porous W was successfully prepared by dealloying two different form factors of tungsten silicide precursors: a bulk ingot and plasma sprayed coatings. Ge was used as the liquid medium to selectively dissolve the Si from the stoichiometric parent materials and upon termination of the dealloying process, pulling the sample out of the bath, the Ge solidified in the pores forming a composite that comprised of porous W with Ge within its pores. The Ge phase was excavated by chemical dissolution in room temperature aqua regia to reveal porous W with open porosity.

The W ligaments were larger than expected for a material with an exceedingly high melting point; the W ligament size did not fall on the universal trendline for the variation of ligament size with inverse homologous dealloying temperature for conventional metal precursors. However, the ligament dimensions corroborated well with the porous C ligament sizes fabricated by the dealloying of SiC, and we hypothesize that both systems are affected by an additional chemical step is involved in the dealloying of stoichiometric precursors. The liquid metal dealloying of W-Si provides an alternate and facile route for the fabrication of bulk porous W and porous W coatings at low temperatures ($< 1300\text{ }^{\circ}\text{C}$) and atmospheric pressure.

Future experiments would involve impregnating the pores with different materials to form composites that would vary depending on the application. It was also observed that the pore sizes in the coating could be varied by altering the experimental times and temperatures, allowing the material microstructure to be tuned for specific uses. Additionally, since the precursors W-Si alloys were inhomogeneous and contained distinct WSi_2 and W_5Si_3 phases, discrepancies between the dealloying of these two silicides warrant further investigation.

A.6 References

- [1] D.P. Dandekar, R.M. Lamothe, Behavior of porous tungsten under shock compression at room temperature, *J. Appl. Phys.* 48 (1977) 2871. <https://doi.org/10.1063/1.324095>.
- [2] C. Selcuk, J. V Wood, Reactive sintering of porous tungsten: A cost effective sustainable technique for the manufacturing of high current density cathodes to be used in flashlamps, *J. Mater. Process. Technol.* 170 (2005) 471–476. <https://doi.org/10.1016/j.jmatprotec.2005.05.037>.
- [3] D. Yong Park, Y. Jun Oh, Y. Sam Kwon, S. Taek Lim, S. Jin Park, Development of non-eroding rocket nozzle throat for ultra-high temperature environment, *Int. J. Refract. Met. Hard Mater.* 42 (2014) 205–214. <https://doi.org/10.1016/j.ijrmhm.2013.09.007>.
- [4] A.G. Hamidi, H. Arabi, S. Rastegari, A feasibility study of W-Cu composites production by high pressure compression of tungsten powder, *Int. J. Refract. Met. Hard Mater.* 29 (2010). <https://doi.org/10.1016/j.ijrmhm.2010.09.002>.
- [5] B. Li, Z. Sun, H. Jin, P. Hu, F. Yuan, Fabrication of homogeneous tungsten porous matrix using spherical tungsten powders prepared by thermal plasma spheroidization process, *Int. J. Refract. Met. Hard Mater.* 59 (2016) 105–113. <https://doi.org/10.1016/j.ijrmhm.2016.06.002>.
- [6] C. Selcuk, N. Morley, J. V Wood, Porous tungsten with controlled porosity by low temperature sintering, *Powder Metall.* 48 (2013) 17–22. <https://doi.org/10.1179/003258905X37648>.
- [7] Q. Shen, D. Zhou, J. Zhang, G. Luo, L. Zhang, Study on preparation and property of porous tungsten via tape-casting, *Int. J. Refract. Met. Hard Mater.* 69 (2017) 27–30. <https://doi.org/10.1016/j.ijrmhm.2017.07.018>.
- [8] I. McCue, *Frontiers of Dealloying – Novel Processing For Advanced Materials*,

Doctoral Dissertation, Johns Hopkins University, 2015.

- [9] I. McCue, A. Karma, J. Erlebacher, Pattern formation during electrochemical and liquid metal dealloying, *MRS Bull.* 43 (2018) 27–34.
<https://doi.org/10.1557/mrs.2017.301>.
- [10] Q. Chen, K. Sieradzki, Spontaneous evolution of bicontinuous nanostructures in dealloyed Li-based systems, *Nat. Mater.* 12 (2013) 1102–1106.
<https://doi.org/10.1038/nmat3741>.

Appendix B: BET Surface Area Reports for Carbon from Melt Spun Ribbon

Performed by Particle Technology Labs, Downers Grove, IL
 Instrument: Micrometrics TriStar II 3020
 Technique: Static Pressure Gas Adsorption/Volumetric
 Degassing Conditions: 1 hour, 105 °C, Vacuum

B.1 Carbon from As Spun Ni₉₂C₈ ribbon

Started: 1/5/2021 11:14:40 AM
 Completed: 1/5/2021 9:19:54 PM
 Report Time: 1/6/2021 8:30:51 AM
 Sample Mass: 0.2529 g
 Cold Free Space: 41.0314 cm²
 Low Pressure Dose: None
 Automatic Degas: No
 Analysis Adsorptive: N₂
 Analysis Bath Temp.: 77.350 K
 Thermal Correction: No
 Warm Free Space: 13.6806 cm³ Measured
 Equilibrium Interval: 20 s
 Sample Density: 1.000 g/cm³

BET Report

BET Surface Area: 203.3466 ± 1.1470 m²/g
 Slope: 0.021338 ± 0.000120 g/cm³ STP
 Y-Intercept: 0.000067 ± 0.000009 g/cm³ STP
 C: 321.350873
 Qm: 46.7186 cm³/g STP
 Correlation Coefficient: 0.9999841
 Molecular Cross-Sectional Area: 0.1620 nm²

| Relative Pressure (P/P ₀) | Quantity Adsorbed (cm ³ /g STP) | 1/[Q(P ₀ /P-1)] |
|--|---|----------------------------|
| 0.012354454 | 38.4975 | 0.000325 |
| 0.048937622 | 45.9965 | 0.001119 |
| 0.125186458 | 52.3161 | 0.002735 |

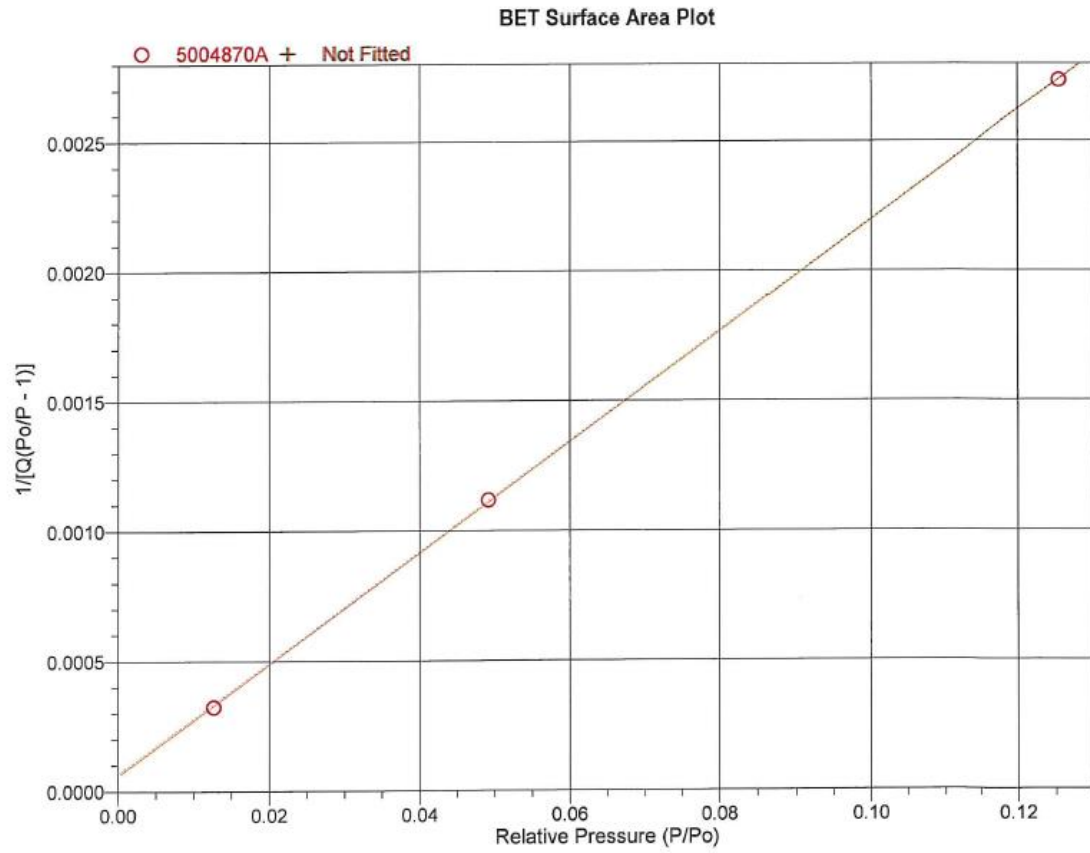


Figure B-1 BET Surface Area plot for carbon from as spun $Ni_{92}C_8$ ribbon

B.2 Carbon from Fe₈₃C₁₇ ribbon annealed at 1000 °C

Started: 1/5/2021 11:14:40 AM
Completed: 1/5/2021 9:19:54 PM
Report Time: 1/6/2021 8:32:10 AM
Sample Mass: 0.0432 g
Cold Free Space: 42.3052 cm²
Low Pressure Dose: None
Automatic Degas: No
Analysis Adsorptive: N2
Analysis Bath Temp.: 77.350 K
Thermal Correction: No
Warm Free Space: 14.1014 cm³ Measured
Equilibrium Interval: 20 s
Sample Density: 1.000 g/cm³

BET Report

BET Surface Area: 4.4714 ± 0.1723 m²/g
Slope: 0.955078 ± 0.037341 g/cm³ STP
Y-Intercept: 0.018352 ± 0.003640 g/cm³ STP
C: 53.041085
Qm: 1.0273 cm³/g STP
Correlation Coefficient: 0.9992366
Molecular Cross-Sectional Area: 0.1620 nm²

| Relative Pressure (P/Po) | Quantity Adsorbed (cm ³ /g STP) | 1/[Q(Po/P-1)] |
|-----------------------------|---|---------------|
| 0.014198395 | 0.4757 | 0.0302077 |
| 0.074838138 | 0.8719 | 0.092772 |
| 0.150701055 | 1.1023 | 0.160976 |

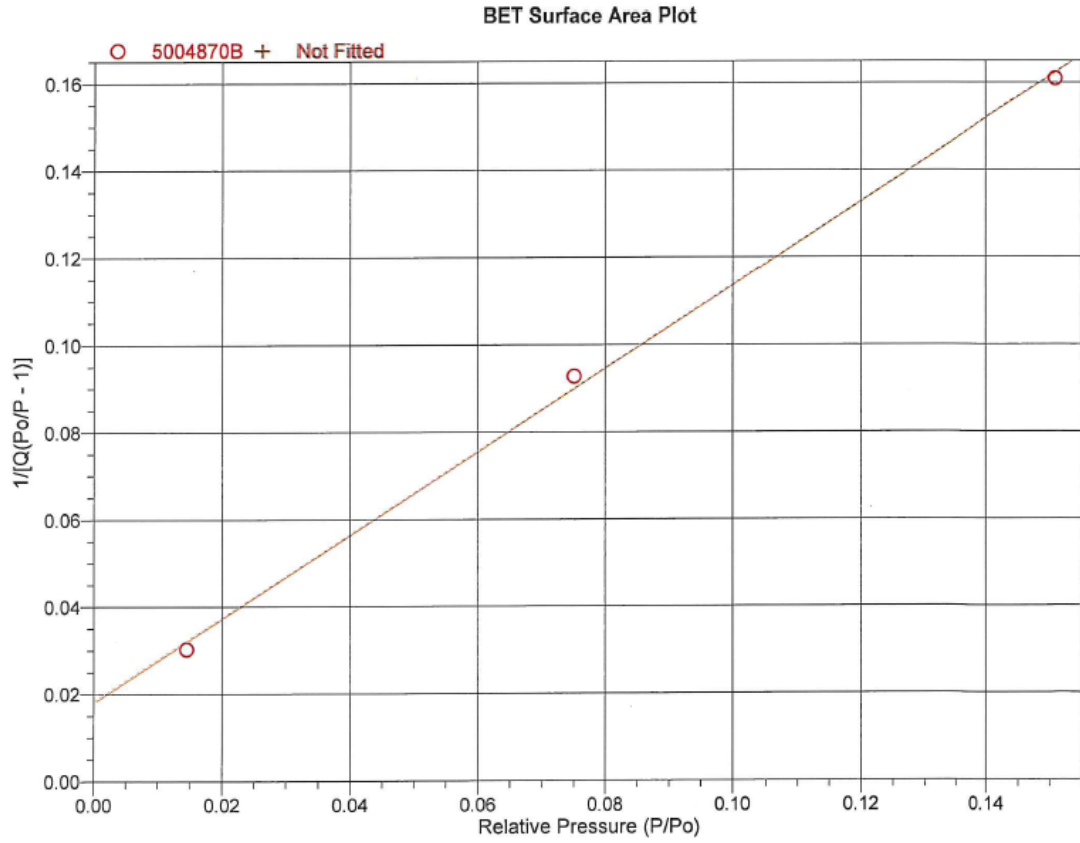


Figure B-2 BET Surface Area plot for carbon from annealed $Fe_{83}C_{17}$ melt spun ribbon

Curriculum Vitae

GINA GREENIDGE

gina.greenidge@gmail.com

EDUCATION

- | | | |
|------------|--|----------|
| PhD | Johns Hopkins University, Materials Science & Engineering Dissertation: "Novel Metallurgical Approaches to Carbon Transformations" Advisor: Jonah Erlebacher | Mar 2021 |
| MS | Howard University, Chemistry Thesis: "The Charge Transfer Effects of NH ₃ and NO ₂ molecules on the Raman fingerprint of graphene" Advisor: Joshua Halpern | 2015 |
| BS | Howard University, Chemistry, Biology Magna Cum Laude, Phi Beta Kappa | 2012 |

RESEARCH EXPERIENCE

Research Assistant, Johns Hopkins University, Baltimore, MD Sep 2015 - present

- Conceptualized and designed a process to synthesize porous graphite via the liquid metal dealloying of silicon carbide at temperatures up to 1400 °C, introducing a novel technique to fabricate porous carbon materials from ceramics.
- Performed the first kinetic analysis of the liquid metal dealloying process on a non-metallic precursor in the literature.
- Developed a novel technique to sequentially transform graphite into various morphological forms, from carbon black to graphene to graphite, using a rapid solidification technique followed by high temperature post-processing treatments.

Research Assistant, Howard University, Washington, DC Jan 2013 - Jul 2015

- Successfully fabricated graphene electrical chip devices using photolithography in a clean room environment.
- Successfully determined the charge transfer effects of gaseous environmental pollutants (NO_x and NH₃) on the Raman fingerprint of graphene establishing potential use of graphene as a gas sensor.

Research Assistant, Howard University, Washington, DC Jun 2011- May 2012

- Redesigned and rebuilt an existing spray pyrolysis system to improve function.
- Optimized growth parameters to successfully grow doped and undoped semiconductor thin films of zinc oxide on different substrates.

PUBLICATIONS

- **Greenidge, G.**, Erlebacher, J., Porous Graphite Fabricated by Liquid Metal Dealloying of Silicon Carbide, *Carbon*. 165, 45-54 (2020)
- Zeng, Y., Gaskey, B., Benn, E., McCue, I., **Greenidge, G.**, *et al.* Electrochemical dealloying with simultaneous phase separation, *Acta Materialia* 171, 8–17 (2019)
- **Greenidge, G.**, Price, S., Erlebacher, J., Carbon Transformation in Melt Spun Nickel Carbon Ribbon (*under review*)

PRESENTATIONS

- Greenidge, G., Erlebacher, J., Porous Graphite Fabricated by Liquid Metal Dealloying of Silicon Carbide, TMS Meeting, 2021 (Oral)
- Greenidge, G., Erlebacher, J., Porous Graphite Fabricated by Liquid Metal Dealloying of Silicon Carbide, Harvard University, Invited Talk, March 2021 (Oral)
- Greenidge, G., Erlebacher, J., Porous Graphite Fabricated by Liquid Metal Dealloying of Silicon Carbide, TMS Meeting, 2020 (Poster)
- Greenidge, G., Erlebacher, J., Synthesis of Porous Graphite by Dealloying Silicon Carbide, *International Symposium on Nanoporous Materials*, 2019 (Oral & Poster)
- Greenidge, G., Erlebacher, J., Carbon Materials from Rapidly Solidified Nickel-Carbon Alloys, *MRS Fall Meeting*, 2018 (Poster)
- Greenidge, G., Halpern J., Effect of adsorbed gases on the G and D peaks of the Raman spectrum of graphene, APS March Meeting, 2015 (Poster)
- Greenidge, G., Halpern J., Adsorption of water vapor on graphene, MRS Fall Meeting, 2015 (Poster)
- Greenidge, G., Halpern J., Transparent ZnO and doped ZnO semiconducting thin films grown by spray pyrolysis, ACS March Meeting, 2012 (Poster)

PATENTS

Erlebacher J., Greenidge, G., Production of Carbon Materials via Melt Spinning, *Patent Pending*

AWARDS/HONORS

Johns Hopkins University

- Edward A. Bouchet Graduate Honor Society Member 2021
- Louis M. Brown Engineering Fellow 2015 – 2016

Howard University

- The Onassis Foundation Lecture Series:
Nanoscience & Nanotechnology Scholarship Recipient 2013
- College of Arts and Science Honors Graduate 2012
- Undergraduate Research Symposium 2nd Place Poster 2012
- Capstone Scholar 2008 – 2012
- Dean's List Honors 2008 – 2012
- 11 Awards for Excellence in Chemistry 2008 – 2012

LEADERSHIP EXPERIENCE

- JHU Diversity Leadership Council 2019 – 2021
- JHU Doctor of Philosophy Board 2018 – 2019

TEACHING EXPERIENCE

Johns Hopkins University Teaching Assistant

- Management and Technology Consulting 2018 – 2020
- Demand Discovery: Finding and Creating Customer Value 2018 – 2019
- Kinetics and Phase Transformation 2017
- Nanomaterials Lab 2017

VOLUNTEER EXPERIENCE

- Volunteer for Family Engineering Day | Johns Hopkins University 2019
- Graduate Student Mentor | Materials Research Society 2017
- Graduate Student Mentor | Howard Middle School 2013 - 2015
- Volunteer at NanoDays | Museum of Science, Boston 2015